THÈSE POUR OBTENIR LE GRADE DE DOCTEUR DE L'UNIVERSITÉ DE MONTPELLIER

En Chimie Séparative, Matériaux et Procédés

École doctorale Sciences Chimiques Balard

Unité de recherche UMR 5247

Identification de composés valorisables présents dans la coquille de l'huître comestible Crassostrea gigas

Identification of valuable compounds from the shell of the edible oyster

Crassostrea gigas

Présentée par Michel BONNARD Le 15 décembre 2020

Sous la direction de Isabelle PARROT et Bruno BOURY

Devant le jury composé de

Pascal GERBAUX, Professeur, Université de Mons

Frédéric MARIN, Directeur de recherche, Université de Bourgogne

Estelle LE BIHAN, Directrice, IVAMER

Vincent LISOWSKI, Professeur, Université de Montpellier

Isabelle PARROT, Maître de Conférences, Université de Montpelier

Bruno BOURY, Professeur, Université de Montpellier

Florent TARBOURIECH, Directeur, Tarbouriech-Médithau

Rapporteur
Rapporteur
Examinateur
Président du jury
Directeur de thèse
Co-Directeur de thèse

Invité



THÈSE POUR OBTENIR LE GRADE DE DOCTEUR DE L'UNIVERSITÉ DE MONTPELLIER

En Chimie Séparative, Matériaux et Procédés

École doctorale Sciences Chimiques Balard

Unité de recherche UMR 5247

Identification de composés valorisables présents dans la coquille de l'huître comestible Crassostrea gigas

Identification of valuable compounds from the shell of the edible oyster

Crassostrea gigas

Présentée par Michel BONNARD Le 15 décembre 2020

Sous la direction de Isabelle PARROT et Bruno BOURY

Devant le jury composé de

Pascal GERBAUX, Professeur, Université de Mons

Frédéric MARIN, Directeur de recherche, Université de Bourgogne

Estelle LE BIHAN, Directrice, IVAMER

Vincent LISOWSKI, Professeur, Université de Montpellier

Isabelle PARROT, Maître de Conférences, Université de Montpelier

Bruno BOURY, Professeur, Université de Montpellier

Florent TARBOURIECH, Directeur, Tarbouriech-Médithau

Rapporteur
Rapporteur
Examinateur
Président du jury
Directeur de thèse
Co-Directeur de thèse

Invité



This thesis was carried out at The Institute of Biomolecules Max Mousseron (IBMM - UMR 5247, UM - CNRS - ENSCM) of the University of Montpellier, under the direction of Doctor Isabelle Parrot and Professor Bruno Boury.

I would like to thank Doctor Isabelle Parrot and Professor Bruno Boury for having welcomed me, having ensured the follow-up and the orientation of my thesis, having pushed me to surpass myself, for having trusted me and in a general way for their support and their wise advices. I would like to express my deep respect and gratefulness.

I thank Florent Tarbouriech for having welcomed me into his company and having placed his trust in me. I would also like to thank Jean-Jacques Thibaut for having welcomed me within the R&D team and for having initiated the collaboration at the origin of this project.

I would like to thank Professor Pascal Gerbaux of the University of Mons, Doctor Frédéric Marin of the University of Bourgogne, Doctor Estelle Le Bihan director of IVAMER and Professor Vicent Lisowski of the University of Montpellier for the privilege they offer me by accepting to judge this work. May they find here the expression of my deepest gratefulness.

I would also like to thank all the staff of the University of Montpellier who made possible the progress of this thesis, Doctor Sonia Cantel (IBMM), Mr Guillaume Cazals of the Laboratoire de Mesures Physiques, Mr Didier Cot of the European Membrane Institute, Mr Bertrand Rebière (ICGM) and Professor Sébastien Clément (ICGM).

Acknowledgments

Finally, I thank those who collaborated on this thesis: Mr Aurélien Lebrun from the Laboratoire de Mesures Physiques for NMR experiments in Chapter III, Ms Saliha Amiche, Ms Claire Bataille, Mr Stébane Anaclet, Ms Marie-France Cauzit, Mr Pierre-Henri Galavielle, Mr Anthony Font, Ms Céline Vidal, all of Médithau for various purposes, Ms Elodie Fernandez and Mr Enzo Martin of the company Arthur Dupuy and Hélène Bisi for their daily support and advices, Marjorie Damian (IBMM) for her support on size exclusion chromatography and electrophoresis experiments, Doctor Julien Fullenwarth (ICGM) and Doctor Florence Rouessac of the European Membrane Institute for their support on milling experiments, Doctor Hélène Van Den Berghe (IBMM) for her support on gel permeation chromatography, and Ms Dominique Granier (ICGM) for her support on XDR experiments.

Ces travaux de thèse ont été réalisés dans le cadre d'une convention industrielle de formation par la recherche (Cifre) entre l'entreprise ostréicole Tarbouriech-Médithau, basée à Marseillan sur le bord de l'Etang de Thau, et deux instituts du Pôle Chimie Balard de l'Université de Montpellier : l'Institut des Biomolécules Max Mousseron (IBMM) et l'Institut Charles Gerhart Montpellier (ICGM). Ce projet est fortement ancré dans une dynamique économique régionale en Occitanie Est, visant à promouvoir les produits locaux, tout en favorisant les partenariats industriels et académiques.

Le programme de recherche initié s'inscrit dans une volonté large d'identification de composés valorisables présents dans certains mollusques bivalves d'élevage cultivés sur le bassin de l'Etang de Thau et en particulier par la société Tarbouriech-Médithau. Le projet à plus long terme s'intéresse à la découverte de composés à forte valeur ajoutée ciblant les secteurs de la nutraceutique, du cosmétique et des matériaux innovants.

Les travaux de doctorat présenté ici se sont concentrés sur l'huître comestible *Crassostrea gigas* permettant notamment d'aboutir à l'identification pionnière de biomolécules colorées. L'huître *Crassostrea gigas* cultivée par Tarbouriech-Médithau bénéficie d'un mode d'élevage par cycles d'exondation programmés et protégé par un brevet-société, lui conférant des caractéristiques organoleptiques appréciées des amateurs et des professionnels gastronomiques. Au-delà de ses qualités gustatives, la coquille présente un esthétisme naturel particulier. Sa surface interne est éclatante et légèrement iridescente, la partie extérieure est quant à elle marquée de motifs rosepourpres, particulièrement exprimés lors des périodes de forte croissance de la coquille.

L'ostréiculture représente l'une des activités aquacoles les plus développées, produisant de manière évidente une accumulation directe de coquilles. Face à ce qui devient un problème environnemental, nous nous sommes dans un premier temps intéressés aux solutions développées dans la littérature scientifique pour recycler cette source de matière première en

accord avec les principes de la chimie durable. Après avoir réalisé un aperçu argumentatif de cette question dans le premier chapitre, le manuscrit détaille les études expérimentales qui nous ont permis d'une part de proposer une caractérisation structurale du biomatériau principal, et d'autre part d'identifier des familles de biomolécules à l'origine de la coloration particulière de la coquille de l'huître *Crassostrea gigas*.

Les coquilles des mollusques bivalves sont des biomatériaux composites structurés. Leur formation résulte d'un processus de biominéralisation au cours duquel une matrice organique est produite par le manteau de l'animal en charge du contrôle de la nucléation et de la croissance de la phase inorganique constituée de carbonate de calcium (CaCO₃). Le carbonate de calcium représente plus de 95 % de la masse de la coquille. Sous forme anhydre, il est décrit sous trois formes cristallines distinctes, la calcite, l'aragonite et la vatérite. La présence de certaines des formes dans la coquille est corrélée au stade de développement de l'animal ainsi qu'à la couche minérale considérée. Chez certains bivalves Ptériomorphes (moule, huître perlière), la couche externe de la coquille (couche prismatique) est composée de calcite, différant de la couche interne (la nacre) composée d'aragonite. La matrice organique représentant entre 1 et 5 % de la masse de la coquille des mollusques, est principalement constituée de protéines, peptides, chitine, polysaccharides, lipides et autres molécules de faibles poids moléculaires.

L'étude structurale de la coquille de l'huître *Crassostrea gigas* élevée par Tarbouriech-Médithau selon des cycles d'exondation programmée a tout d'abord été conduite par microscopie électronique à balayage. Cette méthode permettant d'observer l'arrangement structural général du matériau à l'échelle micronique et submicronique, nous a permis d'étudier la couche interne, mettant en évidence un arrangement microstructural de lamelles superposée d'une épaisseur individuelle d'environ 100-400 nm (longueur > 20 µm), décrit dans la

littérature comme la microstructure foliée. La surface de la couche interne est tapissée par ces lamelles de largeur individuelle allant jusqu'à environ 10 µm, un arrangement structural à l'origine de la faible iridescence résultant de l'interférence de la lumière diffractée sur la surface interne de la coquille. La coupe transversale d'un échantillon de coquille permet d'observer une microstructure crayeuse interrompant la couche foliée. Cette structure est caractérisée par une distribution hétérogène de lamelles formant des pores allant jusqu'à 10 µm³ de volume. Cet assemblage est visible à l'œil sous forme de dépôts blancs, d'une étendue allant jusqu'à plusieurs centimètres carrés de surface, distribués sous la surface foliée. La couche extérieure est caractérisée par un assemblage de prismes comme on peut l'observer dans la nature avec les orgues basaltiques. Chaque prisme présente une épaisseur allant jusqu'à 20 µm et une longueur allant jusqu'à 100 µm. L'assemblage de ces prismes est décrit dans la littérature comme la microstructure prismatique.

Notre étude de la structure cristalline du CaCO₃ constituant la phase inorganique de la coquille a été conduite par diffraction des rayons X sur poudre. Un échantillonnage représentatif de la coquille a permis de mettre en évidence la présence de calcite, une structure cristalline de maille élémentaire de type rhomboédrique. Ces résultats sont en accord avec les données rapportées dans la littérature concernant la structure générale de la coquille des huîtres de la famille Ostreidae, ne permettant pas de mettre en évidence une corrélation quelconque entre le mode d'élevage par cycles d'exondation programmés et la nature de la structure cristalline du carbonate de calcium et de ses arrangements structuraux à l'échelle submicronique.

L'esthétisme si particulier lié à la couleur rose-pourpre des huîtres d'élevage Tarbouriech-Médithau a été étudié dans un second temps, peu de données rapportées de la littérature scientifique permettant d'obtenir des informations précises sur l'origine et la nature de ces pigments. D'un point de vue macroscopique, les motifs rose-pourpres sont distribués sur la couche extérieure de la coquille sous forme de bandes plus ou moins régulières et de tailles variables. A l'échelle submicronique, ces motifs ne présentent pas de différences structurales avec la couche extérieure non colorée, formée de l'assemblage de prismes précédemment mentionné. L'étude des composés contribuant à cette couleur a ainsi été conduite à partir de fragments de coquille entièrement colorés. Un protocole expérimental minutieux a été mis au point puis réalisé. Après décontamination, les fragments colorés ont été dissouts en milieu aqueux acide, la solution filtrée présentant des teintes allant du pourpre au violet en fonction du pH indiquant la présence de pigments solubles en milieux aqueux acides et aux propriétés halochromiques. Si les résidus insolubles caractérisés à l'échelle submicronique ont révélé une structure alvéolaire de polygones, typique de la matrice interprismatique, les solutions de fragments de coquille entièrement colorés dissous dans l'acide (ASMPOS) ont quant à eux été étudiés par spectroscopie de fluorescence et d'absorption UV-visible. Nos études ont démontré qu'à une longueur d'onde d'excitation d'environ 400 nm, l'ASMPOS émet une photoluminescence entre 550 et 750 nm. Cette caractéristique peut être traduite visuellement par une photoluminescence rose-rouge en plaçant un échantillon d'ASMPOS sous une lumière monochromatique d'environ 400 nm. En spectroscopie d'absorption UV-visible, la longueur d'onde d'excitation à environ 400 nm se traduit sous la forme d'une bande connue dans la littérature comme la bande de Soret, caractéristique de nombreuse porphyrines, une famille de pigments hétérocycliques.

Pour définir plus précisément la composition de l'ASM^{POS}, cet extrait a ensuite a été étudié par chromatographie liquide en phase inverse couplée à un détecteur à barrette de diodes ainsi qu'à un spectromètre de masse haute résolution. L'analyse de l'ASM^{POS} a révélé la présence d'une famille de composés absorbant dans le domaine visible du spectre électromagnétique de la lumière. Parmi ces composés, un signal caractéristique de l'uroporphyrine a pu être attribué par analyse comparative avec un standard commercial d'uroporphyrine, permettant pour la première fois d'identifier la présence de porphyrines dans une coquille d'huître comestible. Ce composé contribue ou est très certainement responsable de l'émission rose-rouge sous lumière monochromatique de 400 nm.

Suivant une méthodologie similaire, une autre famille de composés a également pu être identifiée, dont l'acide xanthurénique. Dans le chapitre trois, nous détaillons les expériences et schémas de pensée qui nous ont permis d'identifier ce composé caractéristique de la voie de biosynthèse d'une famille de pigments propre aux invertébrés. L'investigation structurale par spectrométrie de masse en tandem d'un ensemble de pigments a montré une proximité structurelle avec l'acide xanthurénique, laissant supposer l'identification potentielle de cette famille de pigments associée à la voie de biosynthèse de l'acide xanthurénique.

Enfin dans une dernière partie, trois méthodes d'extraction des pigments acido-solubles sont exposées, proposant des méthodologies détaillées pour la préparation d'échantillons décalcifiés et concentrés en pigments.

Résumé

Ces travaux de thèse, ont permis de mettre en évidence pour la première fois la présence de pigments de la famille des porphyrines mais également d'autres composés colorés, squelettes structuraux dérivant de l'acide xanthurénique et évoquant la présence potentielle d'ommochromes. Si les tests d'applicabilité dans différents domaines sont en cours, les méthodes d'extraction des pigments pourpres ainsi que leur identification, ouvrent la voie à des applications en lien avec les secteurs d'activités visés et pourraient ainsi permettre d'imaginer la mise en place dans un futur proche de procédés de recyclage innovants des coquilles de l'huître *Crassostrea gigas*, un secteur économique écoresponsable en expansion dans la Région Occitanie Est, dans lequel la société Tarbouriech-Médithau souhaite s'investir.

Introduction	13
I. Oyster shell recycling: applications and future prospects	18
I.1. Oysters: generalities and environmental issues	20
I.1.1. Phylogenetic classification	20
I.1.2. Production: the main set of data	22
I.1.3. Environmental issues	22
I.2. Structure of oyster shells	23
I.2.1. General morphology	23
I.2.2. General composition	26
I.2.3. Main structural nano-, meso- and macro-organisation in oyster shells	28
I.2.4. Conclusion	33
I.3. Applications of oyster shells	34
I.3.1. Potential applications of NOS	34
I.3.2. Potential applications of CNOS	44
I.3.3. Potential applications of biomolecules extracted from the organic matrix	49
I.4. Critical analysis	57
I.5. Conclusion and perspectives	64
II. Identification of porphyrins in dark and purple patterns of Crassostrea gigas	65
II.1. Introduction	67
II.2. Results	69
II.2.1. Morphology and structure of shell purple and dark patterns	69
II.2.2. Photophysical properties	73
II.2.3. Analysis of acid solutions obtained from shell purple and dark patterns	76
II.2.4. Chemical confirmation of uroporphyrin and derivatives in ASM ^{POS}	81
II.2.5. Identification of uroporphyrin in the shell forming tissue	89
II.2.6. Identification of chlorophyll catabolites in viscera	91
II.3. Discussion	93

II.4. Conclusion and perspectives	96
III. Further investigation of shell purple patterns of Crassostrea gigas: beside porphyrins	,
ommochromes?	97
III.1. Introduction	99
III.2. Results	107
III.2.1. Characterisation of pigments from shell purple patterns	107
III.2.2. Screening of metabolic products and identification of xanthurenic acid	117
III.2.3. Preparation of a sample concentrated in pigments	121
III.2.4. Structural investigation	125
III.3. Discussion	139
III.4. Conclusion and perspectives	142
IV. Acid-soluble pigments of shells of Crassostrea gigas: evaluation of extraction methods	143
IV.1. Introduction	145
IV.2. Results	151
IV.2.1. Sample preparation	151
IV.2.2. Comparison of the methods of extraction of pigments	154
IV.3. Discussion	168
IV.3.1. Impact of extraction methods on extraction yield and scalability	168
IV.3.2. Impact of extraction methods on composition	169
IV.4. Conclusion and perspectives	176
Conclusion	178
Experimental part	181
References	209

Abbreviations

3-HA	3-hydroxyanthranilic acid		
3-HK	3-hydroxykynurenine		
A-C			
AAACa	Active absorbable algal	C18	Octadecyl
	calcium	$Ca(OH)_2$	Calcium hydroxide
AACa	Active absorbable calcium	CaCO ₃	Calcium carbonate
ABTS	2,2'-Azino-bis(3-	CaF ₂	Calcium fluoride
	ethylbenzothiazoien-6-	CCP	Calcitic columnar prismatic
	sulfonic acid)	Cifre	Convention industrielle de
AcOH	Acetic acid		formation par la recherché
ACN	Acetonitrile	CNOS	Calcined natural oyster shell
AIM	Acid-insoluble matrix		•
AMS	Adductor muscle scar	Cryo-SEM	Scanning electron cryo-
ASM	Acid-soluble matrix	3	microscopy
BC	Before Christ		
BPI	Base peak ion chromatogram		
	F 2 8		
D-G			
DAD	Diode array detector	ESI	Electrospray ionisation
DBE	Double bound equivalence	ESM	Ethanol-soluble matrix
DPPH	2,2-diphenyl-1-picrylhydrazil	EtOH	Ethanol
		FIB-TEM	Focused ion beam
E-ASM	Extract of ASM obtain by		transmission electron
	salting out		microscopy
EDTA	Ethylenediaminetetraacetic	FSM	Fat-soluble matrix
	acid	FTIR	Fourier transform infrared
EDTAIM	EDTA-insoluble matrix		spectroscopy
EDTASM	EDTA-soluble matrix	GMP	Good manufacturing practices
EDX	Energy-dispersive X-ray		2
	spectroscopy		
H-M			
HCl	Hydrochloric acid	ICR	Institute for Cancer Research
HF	Hydrofluoric acid	JOS	Juvenile oyster shell
HPLC	High-pressure liquid	LC	Liquid chromatography
	chromatography	LCA	Life cycle assessment
HRMS	High-resolution mass	LED	Light-emitting diode
	spectrometry	MEE	Mantle edge epithelium
IBMM	Institut des Biomolécules Max	MeOH	Methanol
	Mousseron	MS	Mass spectrometry
ICGM	Institut Charles Gerhart	MS/MS	Tandem mass spectrometry
	Montpellier	MS^n	Multistage mass spectrometry
		mRNA	Messenger ribonucleic acid

Abbreviations

N-T				
NaOH	Sodium hydroxide	POR 4	Filter funnel porosity 4µm	
NMR	Nuclear resonance magnetic	POS	Purple oyster shell fragment	
	spectroscopy	PVC	Polyvinyl chloride	
NOS	Natural oyster shell	RNA	Ribonucleic acid	
NPLC	Normal phase liquid	RPLC	Reverse phase liquid	
	chromatography		chromatography	
OSE	Oster shell electrolysate	SEM	Scanning electron microscopy	
P-ASM	Extract of ASM obtained by	spp.	Species pluralis	
	CaF ₂ precipitation	TIC	Total ion chromatogram	
PF	Purple fraction	TFA	Trifluoroacetic acid	
	-			
U-Y				
UV-vis	Ultraviolet-visible	VOT	Viscera oyster tissue	
UV	Ultraviolet	WOS	White oyster shell fragment	
UVA	Ultraviolet-A (400-315 nm)	WSM	Water-soluble matrix	
UPLC	Ultra performance liquid	XPS	X-ray photoelectron	
	chromatography		spectrometry	
UHPLC	Ultra-high-pressure liquid	XA	Xanthurenic acid	
	chromatography	YF	Yellow fraction	

Introduction

This PhD program was carried out in a partnership between the oyster farming company Tarbouriech-Médithau, located on the edge of the Thau lagoon, and two institutes of The Balard Chemistry Centre of The University of Montpellier: The Institute of Biomolecules Max Mousseron (IBMM) and The Institute Charles Gerhart Montpellier (ICGM) (**Fig. 1**). This project is in line with a dynamic economy in Eastern Occitanie (France), aiming to promote local products while supporting industrial and academic partnerships.

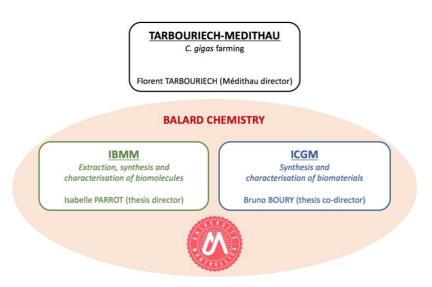


Fig. 1 General project's partnership.

The research program initiated by this thesis is a part of a wider desire to identify valuable compounds from bivalves farmed in the Thau lagoon, in particular by Tarbouriech-Médithau. The longer-term project is interested in the recycling of shells and the identification of compounds with high-performances for application in nutraceuticals, cosmetics and innovative materials. The oyster *Crassostrea gigas* farmed by Tarbouriech-Médithau and studied here benefits from an innovative aquaculture method. It consists to emerge oysters at a given frequency for a given period. This method, protected by a patent¹, allows the production of oysters with organoleptic properties appreciated by gastronomic amateurs and professionals. Beyond its gustatory qualities, its shell has a natural aestheticism, the inner surface is bright

and slightly iridescent and the outer layer is characterised by purple patterns, particularly expressed during periods of high growth (**Fig. 2**). These two characters are studied here. We propose, on the one hand, to characterise the structure of this biomaterial, and on the other hand, to identify the biomolecules contributing to this colour.



Fig. 2 Examples of Crassostrea gigas farmed by Tarbouriech-Médithau.

Oyster farming represents one of the most developed aquaculture activities, obviously producing a direct accumulation of shells. In the first chapter, after a general overview of the morphology and structure of oyster shells, in relation to their phylogenetic distribution, we will describe the recent solutions for the recycling of this natural source of raw materials. Subsequently, an argumentative analysis of the different applications is proposed.

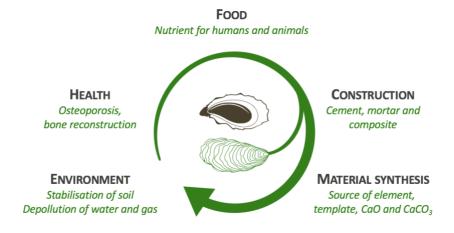


Fig. 3 Application fields of oyster shell as a source of raw materials.

In a second chapter devoted to the shell purple patterns, we will disclose the structural and physicochemical investigations that made possible the identification of a group of compounds well-known among molluscan shell pigments (**Fig. 4**) 2 . A potential metabolic origin is proposed and could provide significant knowledge to the shell pigmentation process.

Fig. 4 Structure of protoporphyrin IX, flavoxanthin, pheomelanin and eumelanin (model structures proposed by Solano 2014^3), representing the three known groups of molluscan shell pigments: tetrapyrroles, carotenoids and melanins.

A second group of pigments is proposed in a third chapter. Based on the identification of a key metabolite of their biosynthetic pathway (**Fig. 5**), we will describe the preliminary results that tend to converge towards this group of pigments.

Fig. 5 Xanthurenic acid.

Finally, we will address in a final chapter the extraction methods that enabled to prepare samples concentrated in pigments ready for structural investigations. In particular, we will examine the concepts and key parameters allowing their selective extraction from the calcareous matrix.

These thesis works, in particular the extraction methods of pigment as well as their identification, open the way to applications related to the targeted sectors and could allow in a near future to innovative recycling of shells of the oyster *Crassostrea gigas*.

I. OYSTER SHELL RECYCLING: APPLICATIONS AND FUTURE PROSPECTS



Oyster farming represents one of the most developed aquaculture activities, producing delicacies unfortunately related to a direct accumulation of waste shells. Facing what is becoming an environmental issue, chemists are currently developing solutions to recycle this wild source of raw material in line with the principles of sustainable chemistry.

An argumentative overview of this question is proposed in this chapter, with a focus on recent data. The reuse of bivalve shells is a well-documented topic for basic applications^{4,5}, but information focusing specifically on the oyster shell, its structure, its use as a valuable waste, its processing and its potential applications are dispersed in the literature. This chapter focuses on the need to find value in the waste oyster shells while avoiding a discussion of the production of pearls and flesh, which is already well documented in the scientific literature^{6–8}.

Starting by a brief overview of the environmental impact of oyster farming, a description of the shell structure is then outlined. Existing and promising applications deriving from oyster shell processing are classified according to the type of raw materials, namely the natural oyster shell (NOS), the calcined natural oyster shell (CNOS) and biomolecules of the organic matrix extracted from the oyster shell. Their relevance is discussed in regard to their scalability, originality and sustainability.

I.1. OYSTERS: GENERALITIES AND ENVIRONMENTAL ISSUES

Oysters belong to the morphological conservative phylum of molluscs. These organisms reveal clues on the Mesozoic and Paleozoic Eras and the history of Earth in general, opening effective windows into the past for palaeontologists^{9–11}. Making the headlines in newspapers few years ago, an unexpected discovery highlighted a large prehistoric oyster fossil of approximately 7 inches wide¹². Naturally and later by farming, oysters have expanded their habitat to reach a global occupancy across salty waters, oceans and seas, excepted in the polar regions¹³. While the research group of Walter *et al.* (2000) reported evidence of oyster consumption by early humans 125,000 years ago, the first historic traces of oyster cultivation date back to 2,000 years BC by Japanese civilisations, 400 years BC by Greeks and approximately 100 years BC by Romans¹⁴. Used for millennia, this mollusc is a familiar seafood and is also used for body art and decoration.

I.1.1. Phylogenetic classification

Oysters are marine invertebrates. In particular, the genus *Crassostrea* includes more than thirty species; the most consumed species, *Crassostrea gigas*, is also known by more than fifteen synonyms and is commonly named Pacific or Japanese oyster (**Fig. 6**). *Ostrea edulis*, well known as European flat or Belon oysters, are sought after for their flavour. Olympia oysters are the only indigenous of the Pacific States. Sydney rock oysters are native to Australia, and Kumamoto oysters must also be mentioned, being the most popular oysters in the United States.

Pearl oysters, members of a distinct order (Pterioida), are farmed for the production of pearl and nacre. The most famous farmed species are from the genus *Pinctada (Pinctada fucata*, *Pinctada martensii, Pinctada maxima*, and *Pinctada margaritifera*) (**Fig. 6**). In the genus *Pteria*, more than thirty different are reported; of particular note are *Pteria penguin* (**Fig. 6**) *Pteria sterna*, and *Pteria avicular*.

Recently, new subfamily and genus were proposed via RNA sequence-structure approach, useful to describe cryptic taxa. These designations are currently not in use by the International Commission on Zoological Nomenclature¹⁵.

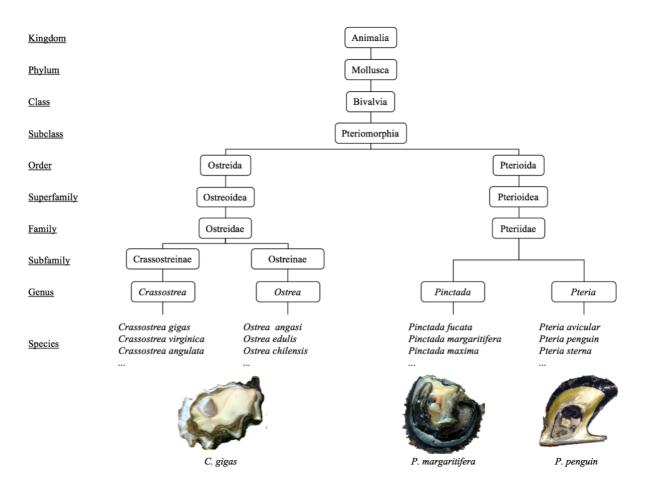


Fig. 6 The phylogenetic classification of oysters according to the World Register of Marine Species, with the most common edible oyster, *C. gigas* (Japanese oyster); the queen of cultured pearl oysters, *P. margaritifera* also known as the black-lipped oyster¹⁶ and *P. penguin*¹⁷.

I.1.2. Production: the main set of data

Whether for consumption or the generation of pearls, the vast majority of oyster production comes from oyster farming. In both cases, the proportion of material that is actually valued in the form of foodstuff or pearls represents a negligible part, less than 10% of the whole mass. According to the FAO, in 2015, the world oyster production totalled nearly 5.2 million metric tons live weight, representing approximately 4.7 million metric tons of shells. Although *C. gigas* is prone to diseases, the production of this most easily farmed species ¹⁸ has remained stable over the last decade. By the beginning of twenty-first century, China is the largest oyster producer, accounting for almost 85% of worldwide production ¹⁹.

I.1.3. Environmental issues

The increasing amount of oyster shells and additional waste starts to be considered a real environmental issue. For example, in South Korea the annual amount is estimated at approximately 300,000 tons of oyster shells covering 4,100 ha of coastline. For Taiwan, this figure is estimated at 25,000 tons²⁰. Without treatment, piles of oyster shells produce sanitation problems and foul-smelling noxious odours due to the decomposition of the remaining attached flesh. Being non-biodegradable, the oyster shells modify local soils, natural waters, and marine ecosystems, especially if their disposal is not controlled²¹. The answer to this ecological challenge should be strongly correlated with the value of oyster shell as a raw material, especially in regions where oyster farming constitutes a large part of the local economy.

I.2. STRUCTURE OF OYSTER SHELLS

I.2.1. General morphology

The soft body of oysters is protected by a shell, an exoskeleton composed of two asymmetrical calcareous valves. The dorsal valve, which acts as a lid, is always less broad and less deep than the ventral valve, which usually rests on the sea bottom or is involved in the cementation process. This variation in shape is particularly pronounced in the genus *Crassostrea*. The beak is the growth origin of the exoskeleton where the two valves are articulated but not joined. Indeed, the valves are joined together by a hinge ligament, a hinge plate and a hinge dentition allowing articulation²². As is the case for most bivalve shells, the hinge ligament is made of two layers²³. The lamellar layer, an elastic organic material, and the fibrous layer, a composite of aragonite and organic material that is elastic only under compressional stress. The umbo is the convex part of the shell, located around the beak, sometimes coinciding with it²².

Oyster shells show ribs as a common sculptural external feature of bivalve shells. Four main categories of ribs can be observed in bivalves, namely, radial, commarginal, oblique and antimarginal; these ribs are not all found in all oyster shells, as described in **Fig. 7**²⁴. Variability is observed among oysters. Ostreidae shells are slightly rounded with ribs, the edge can be elongated, circular or irregular²⁵. Nacreous shells of oysters from the Pteriidae family have a different morphology depending on the species^{6,26}.

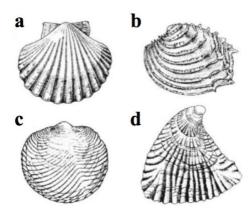


Fig. 7 Representation of the four main categories of rib in bivalves. (a) Radial (Pectinidae). (b) Commarginal (Veneridae). (c) Oblique (Lucinidae). (d) Antimarginal (Ostreidae)²⁴.

The ligostracum, a discrete calcified layer, has been reported in various oysters from the family Ostreidae²⁷, it connects the periostracum to the valves^{27,22} (**Fig. 8**). The adductor muscle scar is a print located on the shell inner surface corresponding to the attachment site of the adductor muscle^{28,29,22}. Depending on the specimen, the scar is generally coloured from bright white to white- and dark-purple in specimens of C. $gigas^{29}$ due to the hypothetical presence of melanin³⁰.

This morphological diversity is the result of concentric mineralisation affected by seasonal and environmental conditions²⁴. The scientific literature is repleted with useful information on the shell formation and biomineralisation processes^{31–36}, structure^{37–40} and mechanical properties^{39,41,42} of mollusc shells in a general, and the interested reader is directed to the corresponding articles.

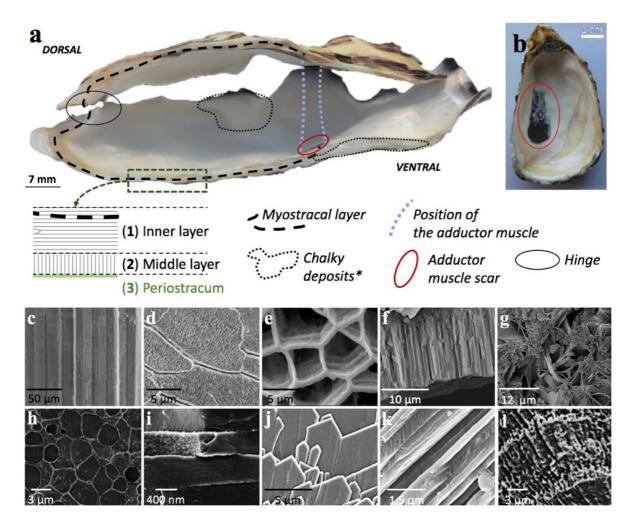


Fig. 8 Structure of shells of adult oysters. (a) Cross section of a shell of *C. gigas* farmed in the Thau Lagoon with a schematic representation identifying the three superimposed layers and their different structures. (b) Dark pigmented adductor muscle scar of a ventral valve³⁰. (c-e) SEM images of the calcitic columnar prismatic (CCP) structure. (c) Cross section of the CCP layer from shell of *O. puelchana*⁴³. (d) Surface of the CCP layer from shell of *O. edulis*⁴³. (e) Interprismatic matrix with a polygonal shape isolated from the CCP layer⁴⁴. (f) SEM image of the myostracum⁴⁵. (g) SEM image of the calcitic chalky structure*. (h) SEM image of the inner nacreous surface layer of shell of *P. margaritifera* with staggered tablets separated by the organic matrix. (i) Cryo-SEM image of nacre in "brick and mortar" from shell of *P. margaritifera* revealing stacked sheets⁴⁶. (j-k) Foliated layer of shell of *O. edulis*. SEM images of (j) blade-like laths with arrow-point tips⁴⁷ and (k) the cross-section. (l) SEM image of the chondrophoral ligostracum of the left valve of *C. virginica*²⁷. *Only observed in Ostreidae specimens.

I.2.2. General composition

The oyster shell is a biogenic composite of mainly anhydrous calcium carbonate (> 95 wt.%) in association with an organic matrix (up to 5 wt.%) secreted by the mantle and constituted by a collection of macromolecules³⁹. Among oyster shells, polymorphs of anhydrous calcium carbonate (CaCO₃) are well known as either calcite or aragonite. No present publication describes the vaterite polymorph; amorphous calcium carbonate has been identified only in larval shells^{48–51} or as a precursor of the aragonite phase in the diseased shell of *P. fucata*⁵². Nevertheless, using focused ion beam transmission electron microscopy (FIB-TEM), recent studies on the microtexture of larval oyster shells of *C. nippona* and *P. fucata* question the occurrence of an amorphous calcium carbonate phase^{53,54}. Considering that FIB-TEM analysis can lead to artefacts⁵⁴, the authors did not observe sufficient evidence of amorphous calcium carbonate. In the same way, *in vivo* confocal Raman microscopy, polarised light microscopy and IR Fourier transform (IRTF) spectroscopy were employed to investigate larval shells of *C. gigas* and *C. virginica*⁵⁵. Again, no evidence for an amorphous calcium carbonate phase instead of aragonite was observed. Thus, the presence of amorphous calcium carbonate in larval oyster shells is still an open question.

On the other hand, biomacromolecules such as proteins, peptides, chitin, polysaccharides, lipids and other low-molecular-weight molecules are part of the shell organic matrix⁵⁶. The composite structure of the oyster shell results from a biomineralisation process that affects each of the specific functional structures³¹. To briefly summarise, oyster shell formation is regulated by haemocytes and mantle edge epithelial cells of the mantle, which cover the shell inner layer^{39,57,58}. As presumed for the formation mechanism of the foliated microstructure in shell of *C. gigas*⁵⁹, the organic matrix plays a critical role in the control of CaCO₃ crystal nucleation, orientation, polymorphism and size^{29,60}. In 2013, Wang *et al.* revisited and proposed a

mechanism of shell growth from the soft body⁶¹. Recently, new insights and hypotheses have been proposed by Cuif *et al.* (2018)⁶⁰ and Zhang *et al.* (2019a)⁶². The interrelatedness of the mineral and organic matrices controls the morphology and the shell mineralisation, having a direct impact on the variety of shapes, colours, mechanical and functional properties that ensure the survival of the living organism.

Shell composition can be affected by exposure of the mollusc to a specific diet in laboratory, as reported for immersion in high Pb(II) concentration⁶³. Passive absorption in the tissues reached the shell through the mantle and influenced the shell amino acid secretion and organic matrix composition. A direct absorption on carbonate calcium is also a possible mechanism. Most of the accumulated Pb(II) did not alter the general appearance of the shell and was likely to be deposited in the prismatic layer of the mineral phase. A long-term study on oysters collected from different places in the Gulf of Mexico highlighted a high variability in shell composition: the composition depended not only on the part of the shell but also on the spatial location along the coast. Bioaccumulation of heavy metals occurred even at very low concentrations (0-70 ppm) in the sediment (Fe > Mn > Cr > Zn > Pb > Cu > Cd). The orders of concentration in tissues (Zn > Cd > Cu > Mn > Pb > Fe > Cr) and shell (Cd > Cu > Zn > Mn > Pb > Fe > Cr) were slightly different from those in the sediment, suggesting a specific accumulation of metals. For Cu and Zn, bioaccumulation is probably related to their role in the physiology of oysters. For Cd(II), the concentration in the shell was approximately 35-42 times higher than that in the sediment; this difference probably resulted from the similarity in charge and size between Cd²⁺ and Ca²⁺, which allows substitution in the carbonate structure⁶⁴.

I.2.3. Main structural nano-, meso- and macro-organisation in oyster shells

The general structural layout of shells of adult oyster is presented in **Fig. 8a**. Each valve can be segmented into three superimposed layers of different structures and compositions^{45,13}. The outermost layer of the shell, named periostracum (3 in **Fig. 8a**)⁶⁵, is a proteinaceous thin layer²². This organic skin seems to protect the shell from decalcification and/or abrasion and is a barrier against fouling⁶⁶. The periostracum is essential for the initial mineralisation⁶⁶. The middle (2 in **Fig. 8a**) and inner (1 in **Fig. 8a**) shell layers, respectively the medial ostracum and hypostracum⁶⁵, are both an assemblage of CaCO₃ with an organic framework. However, those layers exhibit different structural organisation. To describe this organisation, the mesoscale (2-50 nm) and the macroscale (> 50 nm) must be considered⁶⁷. Carter and Clark (1985) proposed a structural classification of molluscan shell microstructures, including those commonly observed in oyster shells (*i.e.*, the prismatic, nacreous and foliated microstructures)^{68,69}. However, prismatic, nacreous and foliated microstructures can undoubtedly be identified based on their visual aspects, with specific surface areas varying from 10⁻⁸ to more than 1 cm². The location of these microstructures differs from one species to another and even within a given species.

I.2.3.1. Calcitic columnar prismatic structure (CCP)

The CCP constitutes the main structure of the shell middle layer (2, **Fig. 8a**) in both Pteriidae and Ostreidae^{70,71}. This structure was initially observed only in the dorsal valve of shells of Ostreidae and in both valves of shells of Pteriidae⁷⁰. More recently, MacDonald *et al.* (2010) revealed the presence of calcitic prisms in the outermost mineralised layer of both the dorsal and ventral valves of shells of *C. virginica* and *C. gigas*, with a lower prevalence in the ventral valve⁴⁵. This can be explained by the cementation of the shell on hard surfaces. Under natural conditions, only the ventral valve is involved in cementation, leading to a modification of the prismatic layer into a structure known as a ridge-and-furrow structure⁷². The CCP layer, which is well defined in the shell of *P. radiata*⁷³, is a fragile layer that can be simply damaged by post manipulation of the shell once out of water.

The CCP structure consists of long irregular prismatic units⁷⁴ comparable to columnar basalt (**Fig. 8c**). Polygonal prisms are densely packed in aggregates and separated by a thick interprismatic organic matrix^{70,75,44}. In shells of Ostreidae, prisms are made of micronized calcitic laths like the underlying foliated layer (**Fig. 8d**)^{43,71}, whereas in shells of Pteriidae, prisms are made of globular or rhombohedral nanounits. The nacre-prism boundary in shells of *P. margaritifera* was described by Dauphin *et al.* (2008) as a distinct fibrous zone with the organic matrix similar to that found in the nacreous layer⁷⁶. The Baronnet research group completed the description by reporting a substructure made of elongated round-shaped microdomains (approximately 100 nm) known as granules⁷⁷. In all cases, the microdomains are always encapsulated by an intraprismatic organic matrix^{70,77,65,78}. Some microdomains are fully amorphous, whereas others are single crystals of calcite^{70,77}. More recently, nanosized monocrystals were identified by means of X-ray absorption spectroscopy in the prism of shell of *P. fucata*⁷⁹. After decalcification, the interprismatic matrix revealed a polygonal shape (**Fig.**

8e)^{44,74}. The intraprismatic matrix, which can be removed by proteolysis of the CCP to observe its location and sinuous shape, has not been extensively described⁷⁴.

A recent study demonstrated the complexity of the prismatic structure in shell of *P. margaritifera* at the nanoscale using X-ray Bragg ptychography⁸⁰. The CCP prism appears to be based on assembled granules that form coherent crystalline domains with a correlation length of approximately 400 nm (larger than the granule size).

I.2.3.2. Myostracal layer

The myostracal layer (or myostracum) is a hierarchically complex structure deposited at the site of adductor muscle attachment, the scar. The layer stretches from the edge of the adductor muscle scar to the umbo in the inner shell layer as a result of shell growth. As observed in the shell of adult *C. gigas* and regardless of the oyster family considered, the myostracum has a prismatic columnar structure of aragonite with an approximate thickness of 5 to 35 μm²⁹. Scanning electron microscopy (SEM) analysis has revealed needle-like, fine (< 0.2 μm) and closely packed prisms without observable interprismatic organic matrix (**Fig. 8f**)⁴⁵. While MacDonald *et al.* did not find any observable organic matrix by SEM, Lee *et al.* (2006), described the extraction of soluble proteins from myostracal prisms, suggesting the presence of an inter- and/or intraprismatic organic matrix²⁸. With the hinge ligament and the ligostracum, these are the only aragonite structures observed in shells of Ostreidae⁴⁵.

I.2.3.3. Nacreous layer

The nacreous layer constitutes the lustrous and iridescent inner layer of shells of Pteriidae. This layer is largely observed among bivalves³⁴ but absent in shells of Ostreidae, for which, in some cases, the term "nacre" is falsely attributed to the foliated layer^{81–83}. In material science, nacre refers to a well-defined "brick and mortar" structural layout, as observed in shells of bivalves³⁴. The nacreous layer has very specific and clear characteristics, including the presence of staggered tablets of aragonite with different shapes and sizes but of similar thickness (from less than 200 nm to 500 nm) (**Fig. 8i**). Densely and closely stacked tablets are separated by an organic layer too thin to be observable by SEM analysis^{65,46,84,85}. Rousseau (2011) reported that nacre tablets from shells of *Pinctada* spp⁸⁴. are pseudohexagonal-shaped with a lateral extension of a few microns (approximately 2 to 10 μm, **Fig. 8h**), organised in parallel lamella of approximately 0.5 μm thick. Electron diffraction has established that each aragonite tablet is a single crystal⁶⁵, but Checa and Rodríguez-Navarro (2005) indicated that in shells of Pteriidae, early nacreous crystals are generally polycrystalline before becoming progressively individualised and monocrystalline⁸⁶. Very recently, Lertvachirapaiboon *et al.* (2018) succeeded in isolating aragonite plates from nacre to characterise their optical properties⁸⁷.

I.2.3.4. Folia structure

The folia structure accumulates at the inner shell layer (hypostracum), as does the nacreous structure³⁸. The foliated layer is visually similar to the nacreous. Folia has not been reported in shells of Pteriidae⁴⁰ but is extensively highlighted in shells of *Crassostrea* spp., representing up to 60-70% of the global shell volume^{88,89}. The foliated structure is characterised by an assembly of thin sheets made of laterally joined calcitic blade-like laths (100-400 nm thick, 2-5 µm wide^{90,91,51}) with arrow-point tips, as presented in **Fig. 8j**^{47,91,40,13}. The sheets are stacked

perpendicular to the inner shell surface, forming a microstructure with a thickness > 100 μ m in shells of *C. gigas*^{88,45,91} (**Fig. 8k**). This highly ordered lamellar structure has a well-defined crystallographic orientation, as reported by Checa *et al.* (2007)⁴⁷. At the mesoscale, Lee *et al.* (2008) highlighted the substructure of folia as single crystal calcitic globular nanograins of 30 to 50 nm encapsulated inside the organic phase, forming what they call an "organised foamlike structure"^{92,59,89}. It was assumed that the foliated microstructure stems from calcitic prisms composed of stacked laths⁷¹.

I.2.3.5. Chalky deposits

Chalky deposits are white lens-shaped domains of more or less extent, randomly distributed throughout the whole inner layer of the shell, interrupting the extent of the folia^{45,91}. Such organisation is phylogenetically typical of oysters from the order Ostreida, as is the case in shells of *C. gigas*¹³, *O. edulis* and *O. angasi*⁹³. The chalky deposits are characterised by the isotropic orientation and packing of the calcite plates, resembling in some aspect to the aggregation in sand-roses. Some deposits form aggregates of several layers^{45,91} with a size of several tens of micrometres in length and 100 to 500 nm in thickness (**Fig. 8g**). In this isotropic organisation, the layers are not closely packed but essentially remain in contact at the edges, resulting in a large void⁵¹ between layers with a volume up to 10 µm³. A more detailed description of this microstructure in the shell of *C. angulata* was recently published⁹⁴. The origin and role of chalky deposits, considered as heterogeneities in the structure of the shell, could be related to a shell disease⁵⁹ or as a response to environmental stimulus⁹⁵. Due to its porosity, the chalky structure has been proposed to act as a shell lightener resulting from an adaptation to soft substrates^{13,96-98}. Similarly, Taylor and Layman, (1972) suggested that chalky deposits could act as crack stoppers, as do pores in bones⁹⁹.

I.2.3.6. Ligostracum

The ligostracum, a discrete layer only observed in shells of Ostreidae, is located in the inner shell layer, it binds the foliated shell layer to the hinge ligament and seems specialised in dorsal flexion. The aragonite polymorph forms a prismatic structure of 8 to 16 μ m thick and approximately 1-6 μ m width (**Fig. 81**)²⁷.

I.2.4. Conclusion

Oysters arise from two distinct orders whose shell composition and structural layout are distinct (**Table 1**). This phylogenetic morphotype is essential in some applications.

Table 1 Phylogenetic distribution of microstructures identified in oyster shells.

Structure	Shell location	Phylogenetic distribution	Minerals	References
Calcitic columnar prism	Medial ostracum	Pteriidae, Ostreidae	Calcite	73,74,44,70,77,43,100,79,45
Myostracum	Hypostracum	Ostreidae, not observed in Pteriidae	Aragonite	45,28,29
Nacre	Hypostracum	Pteriidae	Aragonite	86,65,46,84,34
Folia	Hypostracum	Ostreidae	Calcite	13,40,45,47,59,88
Chalky deposit	Hypostracum	Ostreidae	Calcite	45,51,94
Ligostracum	Hypostracum	Ostreidae, not observed in Pteriidae	Aragonite	27

I.3. APPLICATIONS OF OYSTER SHELLS

The biochemical composition of the shell is highly reliant on the breeding environment and bioaccumulation processes, especially towards heavy metals^{101,64,102}. This point is important to keep in mind from the perspective of health applications, such as the trending use as a source of natural calcium in nutritional supplements for adults and children^{103,104}.

Natural oyster shell (NOS), calcined natural oyster shell (CNOS) and biomolecules of the organic matrix extracted from the oyster shell constitute the raw materials for any potential application. The following sections provide a critical description of valuable routes including processing methods when necessary.

I.3.1. Potential applications of NOS

Before any treatment, shells are generally decontaminated of organic substances and salts by radiation, thermal treatment, brushing or oxidation with soaking solutions. In most cases, shells are roughly crushed to reduce storage and transport volumes. Milling gives a uniform and easy-to-use powder, allowing to increase the available specific surface area for chemical and physical transformations¹⁰⁵. The mother of pearl (the inner layer of shells of Pteriidae) is highly prised especially for body art and fashion purposes. In this case, the animal is specifically farmed for its shell and pearl, only requiring a surface treatment followed by shaping.

I.3.1.1. Food and cosmetic industries

NOS powder is a relevant source of calcium, offering real value for food (animal or human), nutraceutical or cosmetic purposes. Traditional Chinese medicine praises the health benefits of what is commonly known as *Concha ostrea* in Latin (Mu-li in Mandarin). The recent edition

of the Chinese Pharmacopeia lists NOS powders of different species; the shell of *C. gigas* is the major source of this material, and CaCO₃ the major effective constituent^{106,107}. Another review summarising cosmetics in Roman antiquity referred to oyster shell powder as an ingredient for smoothing skin due to the potential local burning effect of lime¹⁰⁸.

NOS powder is a potential natural alternative for synthetic phosphate in pork-based products and has attracted substantial interest 109,110. With a clean label, this calcium source acts as a real additive for food and health products 111,112 or animal feeding 113-116. Different oyster shell powders are commercially available for their benefit effects against bone-related deficiencies. For the development of such products, the granulometry of the oyster shell powder and its association with other elements have a direct influence on the bioavailability and solubility of calcium as was observed on ovariectomised and albino rats by oral administration^{117,118}. The oral uptake of Mg-, Fe-, Cu- and Zn-rich mollusc shell powder carries health benefits, however, the high bioaccumulation ability of oyster shell, higher than that of eggshells, suggests that traces of toxic heavy metals may often be present or can lead to adverse effect by oral or dermal route¹¹⁹. Therefore, caution and safety-oriented approaches are recommended for food, animal feeding or other human uses. To protect humans from exposure and consumption, different organisations have specified allowable levels of heavy metals. As an example, an evaluation of NOS powders of *P. margaritifera* from French Polynesia revealed that calcium constitutes 40% of the total weight of the shell. If we consider a human intake of 2.5 g per day, the levels of hazardous metals such as Cd, As, Hg and Pb are lower than the maximum levels authorised by food committees¹²⁰.

I.3.1.2. Medical uses

Nacre produced by oysters of the genus *Pinctada* have been considered as a prime candidate for bone tissue bioengineering applications, as this biomaterial is compatible with bone tissues and has high mechanical properties⁸⁵. Based on *in vitro* and *in vivo* studies, nacre was described as a natural, biocompatible and biodegradable biomaterial with osteoinductive, osteointegrative and osteoconductive properties and was therefore extensively studied for its bone substitution capacity. One of the first historical instances of the use of nacre in bone tissue bioengineering was reported in 1931 in the lower jawbone of a Mayan individual (**Fig. 9**)¹²¹.

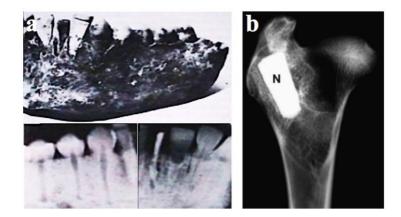


Fig. 9 Examples of nacre bone substitutes. (a) Incisors of the lower jawbone replaced by nacre ¹²¹. (b) Solid nacre (N) implanted in the femur of sheep after 10 months ¹²².

Later, major breakthroughs have been made by the group of Prof. Lopez in the field of bone graft substitution by nacre of shells of *Pinctada* spp., as highlighted by Westbroek and Marin¹²³. This work includes *in vivo* and *in vitro* studies with various nacre preparations, such as nacre powder mixed with blood, nacre chips, and nacre prostheses⁸⁵; alginate hydrogels including nacre powder have also been investigated¹²⁴. In contrast, only one study has focused on the osteogenic capacity of shells of Ostreida¹²⁵. This study is attractive since it shows the potential

use of NOS for bone tissue bioengineering, not only restricted to nacre from shells of *Pinctada* spp.

With the advance of material science, this field of research is in constant progress. The development of functionalised and specific composites with various shapes constitutes one of the main challenges. Promising perspectives were recently obtained with the design of hydroxyapatite nanoparticles coated on substrates of nacre from shell of *P. maxima*¹²⁶, with composite of calcium sulfate and oyster shell¹²⁷ or with scaffold composites of dried oyster shell powder and poly(L-lactide)¹²⁸ or poly(\varepsilon-caprolactone)¹²⁹. Moreover, the use of innovative technologies for the development and production of personalised bone-like implant, with controlled porosity and shape start to be used in research laboratories. A good example is the use of 3D printing technology recently applied to design scaffolds of NOS powder dispersed in a polycaprolactone matrix with a positive osteogenic activity when tested *in vitro* on osteoblast-like cells¹³⁰.

By combining new technologies with material science and biology, these studies show the outstanding properties of NOS in bone grafting. It would be interesting to evaluate the osteogenic performances of NOS compared to others more accessible and less expensive natural composites. Other potential medical uses stay underexplored despite the presence of few preliminary studies in the literature. For example, the stimulation of skin fibroblasts by nacre powder implanted between dermis and hypodermis in rats was observed by Lopez *et al.* (2000)¹³¹, as well as the anticarcinogenic potential of powdered shell of *C. gigas*, when administered to mice with induced tongue tumours¹³².

I.3.1.3. Pollutant remediation

I.3.1.3.1. Soil quality improvement

The p K_b of hydrogen carbonate (6.6) has led to consider NOS as an efficient base to neutralise the acidity of soil in different environments, natural or polluted¹³³. Treatment of acidic soil with pulverised NOS caused neutralisation but also a beneficial increase in Ca^{2+} , Mg^{2+} , K^+ and Na^+ and the stabilisation of heavy metals with low solubility that are less exchangeable upon lixiviation (**Table 2**).

Table 2 Natural oyster shell for the remediation of soils contaminated by metal cations.

Removable pollutants	References
Cu(II)	134
Pb(II)	134-138
Cd(II)	135-137,139,140
AS(III)/As(V)	134,141
Co(II)	142
Ni(II)	142,143
Mn(II)	142,143

Surface adsorption is a possible explanation, in addition to the formation of poorly soluble metal hydroxides or metal carbonates. Such decontamination or stabilisation is also dependent on the CaCO₃ mineral¹³⁵, on the pH, aerobic conditions, ion composition and counter-ion but in general, the efficiency of NOS to stabilise soil has been established. Some studies mentioned a putative role of chitin occurring in the organic matrix of the shell and its possible coordination of heavy metal cations.

Although not enriched in carbon, NOS powder can be a source of carbon for plant growth; besides, the presence of residual NaCl is apparently not injurious in most cases¹⁴⁴. Combining NOS and biochar or biopolymer improves soil fertility, carbon sequestration and worm activity^{145,146}. Given the over-use of fertilisers, especially in agriculture, and the resulting

deterioration in water quality, NOS powders were found to be effective in phosphorus removal and are applicable as a beneficial media in artificial wetland systems ^{147,148}.

I.3.1.3.2. Water treatment

Living oysters are well-known for their capacity to reduce eutrophication in natural water¹⁴⁹, as well as metals cations, plastic particles and other chemicals in some cases^{150–154}. Although, high efficiency is not always achieved, the list of pollutants that can be potentially removed by NOS is summarised in **Table 3**, including anions, cations, organics such as antibiotics¹⁵⁵, neurotoxins¹⁵⁶ and nitrogen¹⁵⁷.

Table 3 Natural oyster shell for the remediation of water contaminated by metal cations and anions.

Removable anionic pollutants	References
PO ₄ ³⁻	148,158-164
F-	164
NO ₃ -	165–168
Removable cationic pollutants	References
Cu(II)	169,170
Ni(II)	169,171
Mn(II)	172
As(V)	173,164
U(VI)	164
Th(IV)	164
Pb(II)	174
Fe(III)	175
Zn(II)	175
Co(II)	142

Two major phenomena can explain the ability of NOS to remove such pollutants: first, the ionic interaction between ions and the surface of NOS; and second, the precipitation on the NOS surface of insoluble salts resulting from the presence of carbonate, calcium and hydroxyl. Unfortunately, many experimental parameters are not systematically reported which limits comparability between the different studies. The shell structure and its microstructures are parameters that can drive the ability of NOS to adsorb pollutants as this was shown for the different adsorption behaviours between the prismatic and nacreous layers 170. The organic

matrix may also participate in the complexation of cations and can explain why removal is more efficient with NOS than with calcined NOS.

Thanks to its porous structure and its buffering properties, NOS in collaboration with microorganisms is also relevant in eco-friendly remediation of wastewater achievable in packed-bed bioreactors ^{176,177,165,178–183}. In general oyster shells served a threefold purpose: as a biofilm carrier, a source of organic carbon and as a basifying agent ^{182,184,185}. Research conducted in this field has also been developed at the pilot-plant scale using oyster shells mixed with inorganic minerals like zeolite for phosphorous and nitrogen removal ¹⁸⁶ or for the growth of biofilms. ¹⁸⁷

NOS is efficient to remove a wide range of pollutants from wastewater at various processing scale, it would be interesting to evaluate its sorption capacity towards highly hazardous pollutants. NOS could also be a relevant fixing support in aquaculture as it is the case for the development of larvae *C. gigas* in hatchery¹⁸⁸ or waste water treatment.

I.3.1.3.3. Dechlorination of waste

This is certainly not the most appealing route for recycling oyster shells, but surely a useful and simple application. When mixed with polyvinyl chloride (PVC), NOS neutralises harmful hydrochloric acid resulting from PVC incineration with an efficiency similar to commercially available calcium carbonate and with CaCl₂ as by-products^{189,190}.

I.3.1.4. Material synthesis

I.3.1.4.1. Composites

Recent researches demonstrate that NOS can be used as filler in polymers such as polyethylene¹⁹¹. Although performances are limited, the thermal decomposition of NOS at high temperature generates CO₂ that is relevant for retarding the thermal decomposition of the polymer and partially preserves from O₂. Composites made of NOS and polyethylene, polypropylene, polyurethane, polyester, natural rubber or asphalt present remarkable mechanical and thermal stability^{192–199}. The granulometry of NOS powder and the mediation of interfacial weak interactions revealed to be crucial points for the development of such composites. These studies show that NOS is a cheap, natural and easy to work substitute of common fillers in polymeric industry.

I.3.1.4.2. Foaming agent

Due to the production of CO_2 resulting from the decomposition of calcite at T > 550 °C, NOS has been used as a foaming agent for the preparation of vitrocrystalline foam. The best results were obtained with 91wt.% glass bottles and 9 wt.% oyster foams fired at 900 °C, demonstrating characteristics and properties similar to (or better than) those of analogous commercial products such as glass and alumina foams²⁰⁰.

I.3.1.4.3. Templates in material science

In this field, the general approach is the replication of natural organs leading to materials biomimicking natural structures. Since it is easily removed by acidic treatment, NOS is an interesting option as sacrificial template for such morphological mimicry. Careful attention should be paid to the shell structure selected as the template and the targeted application. For

example, the design of folded SiO₂ requires a shell substrate made of chalky and foliated structures which only occurred in shells of Ostreidae²⁰¹. Another example is the pyrolysis of powdered NOS of layered structure mixed with soft pitch for the preparation of porous carbon anodes in lithium ion batteries²⁰². However, materials are not performant enough to be an attractive way of recycling.

I.3.1.4.4. Support for catalysts in organic chemistry

The use of NOS as support of catalysts is a growing field of research with high potential. Heterogeneous catalyst was formulated with powders of CuBr and NOS with higher efficacy than a mixture of CuBr and CaCO₃²⁰³. The authors hypothesised an important chelating role of chitin and proteins constituting the organic matrix of NOS for [Cu]-active species. The good chemical stability and reusability (at least eight times) of the [NOS–CuBr] composite is among the attractive points of this approach. Among other recent attractive data, NOS powder has been found to be useful as a support for MgO, Al₂O₃, CaCO₃ and zeolite (ZSM-5) to catalyse gas produced by the pyrolysis of waste tires²⁰⁴. Despite the novelty of the approach, the latter is limited by the necessity to avoid any shell contamination that would disturb the catalytic activity.

I.3.1.4.5. Relevant original source of calcium, calcium carbonate and sodium

The most general way of recycling seashell waste is the use as aggregates for the formulation of concrete^{205,206}. The important points being the granulometry of NOS and other minerals entering in the formulation^{207,208}. Despite the relative simplicity for the implementation of this material, their long-term durability is not well known. Such applications are not innovative but still relevant for a large-scale recycling of NOS.

The use of NOS instead of ores as source of CaCO₃ can also be innovative for the production of advanced materials such as aragonite needles²⁰⁹, high-purity calcite submicron powder⁸³ and CaSO₄:2H₂O powder or whiskers²¹⁰. In this field the hydroxyapatite is the paramount example of a high-demanded Ca²⁺-containing material (**Eq. 1**) and NOS was found useful for its synthesis with different morphologies and specific surface areas depending on the conditions of the hydrothermal process (**Fig. 10a**)^{211–213}. In an innovative approach, NOS was used for the preparation of 1D nanostructured single-crystalline Na₂Ti₆O₁₃ and Na₂W₄O₁₃ with lower processing temperature and higher yield than with chemical mixtures (**Fig. 10b-c**)²¹⁴.

Eq. 1 $10CaCO_3 + 6(NH_4)_2HPO_4 + 2H_2O \rightarrow Ca_{10}(PO_4)_6(OH)_2 + 6(NH_4)_2CO_3 + 4H_2CO_3$

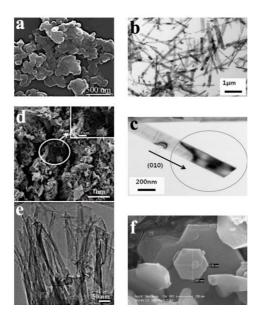


Fig. 10 Examples of advanced materials synthesised with oyster shell (a) SEM image of hydroxyapatite produced by hydrothermal processing of NOS at 200 °C for 92 h²¹¹. (**b-c**) TEM images of Na₂Ti₆O₁₃ nanorods prepared with NOS²¹⁴. (**f**) Ca(OH)₂ nanoplates prepared from CNOS according to Khan *et al.* (2018)²¹⁵. (**d-e**) Calcium silicate prepared with CNOS, reproduced from Ref.²¹⁶ with permission from the Physical Chemistry Chemical Physics Owner Societies.

I.3.2. Potential applications of CNOS

Calcination of NOS leads to the so-called calcined natural oyster shell (CNOS), a potential multi-use raw material, widely employed for the preparation of concrete^{217,218}. Calcination is usually performed on mixed batches of shells with unreliable traceability and poor consideration of the composition and structural differences among oyster shell species. This is a limit to the recycling of shells, especially when targeting specific synthesis of advanced materials. Calcination of NOS starts with water loss and decomposition of the organic matrix at approximately 200-400 °C, leading to a weight loss of 2-4%²¹⁹. In the case of aragonite-rich shells like the shell of *P. margaritifera*, a thermal structural phase transition from aragonite to calcite occurs between 280 and 500 °C^{220,221}. At higher temperatures, the decomposition of calcite leads to the eco-valuable production of calcium oxide, which is concomitant with the release of a non-eco-friendly carbon dioxide between 550 and 800°C (weight loss of 40-45%) but calcite can still be present up to 900 °C (Eq. 2)²²².

Eq. 2
$$CaCO_{3(s)} \rightarrow CaO_{(s)} + CO_{2(g)}$$
 $\Delta H= 178 \text{ kJ/mol}$

In light of the energy required, thermal treatment of NOS should be considered only for attractive applications. An innovative microwave calcination treatment was recently applied to oyster shell powder with quasi-complete decomposition obtained at 900 W (2.45 GHz; 20 min)²²³. Considering the time and energy required, microwave calcination is an attractive method. NOS powder can also be decomposed with high-voltage electric current under a reduced oxygen concentration at approximately 800 °C^{224,225}. Known as active absorbable calcium (AACa) or oyster shell electrolysate (OSE), this powder is mainly composed of lamellar CaO structure (**Fig. 11**)^{224,226} reminiscent of the nacreous and foliated structures in

NOS. However, at present, the description of the preparation of AACa lacks scientific criteria for repeatability.

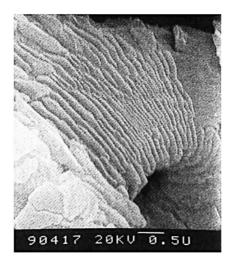


Fig. 11 Structure of AACa. Captured from Fujita et al. (1988)²²⁵.

I.3.2.1. Medical uses

The research group of Fujita extensively studied the effect of preparations of CNOS in the prevention and treatment of calcium metabolism-related diseases. Their review on osteoporosis summarises the contributions of AACa and active absorbable algal calcium (AAACa)²²⁷. Compared to CaCO₃, AACa was described as a readily absorbable form of calcium,²²⁵ favourable for the treatment of osteoporosis by oral route^{228,229} as well as AAACa, which is a mixture of AACa with an extract of the seaweed *Cystophyllum fusiforme*^{230–232}. AAACa was suggested to be the most efficient ingredient at preventing osteoporosis²³³ with positive analgesic effect on joint pain²³⁴. More surprisingly, supplementation with AAACa was reported to prevent light, sound and emotional stress resulting from neuromuscular instability²³⁵. Among these various studies, no adverse effects were observed.

This substantial work displays interesting effects of CNOS toward the prevention of osteoporosis. Combining CNOS with other active ingredients could be an innovative approach for the development of nutraceuticals as it was recently shown for the treatment of inflammatory bowel disease on mice by oral administration of zeolite-CNOS mixture²³⁶. The development of such products has to be evaluated in comparison with NOS-based products given the low sustainability of NOS calcination.

I.3.2.2. Pollutant remediation

I.3.2.2.1. Soil quality improvement

Compared to NOS, CNOS is sometimes more effective for stabilisation and pH neutralisation of contaminated soils, this being related to the higher basicity of the oxo anion in CaO (**Table 4**)¹³³. Comparative researches are needed to evaluate the relevance of CNOS compared to NOS.

Table 4. Calcined natural oyster shell for soil and water remediation.

Applications in contaminated soils and wastewater	References
Sb-contaminated soil	237
As-contaminated soil	238,239
Cu-contaminated soil	239
Pb-contaminated soil	238,239
Cd(II)-contaminated water	240-242
Ni-contaminated water	171
PO ₄ ³ -contaminated water	243,244
B-contaminated water	245
Microbial-contaminated effluent coffee wastes	246
Impurities in palm kern oil refining	247

I.3.2.2.2. Water treatment

CNOS generally removes cationic pollutants more effectively than NOS as described for Cd(II) (**Table 4**)^{241,242}. The higher the temperature of calcination, the better is the efficiency of CNOS. This observation is directly related to the large increase in the specific surface area of the material upon calcination²⁴⁰. This phenomenon can also be explained by the formation of insoluble metal hydroxides by adsorption of the metal on the surface of CNOS. Unlike NOS,

CNOS was applied to remove and recover other chemicals such as boron²⁴⁵, free fatty acids and iodine from the bleaching process of palm kernel oil²⁴⁷, and pathogen like $E.\ coli^{246}$.

I.3.2.2.3. Gas treatment

The basic character of CNOS is well-adapted to remove pollutants such as SO_2 , SO_3 , H_2S and NO_x in dry or wet processes as well as CO_2 sequestration^{248–250}. Obviously, this strategy is relevant only if the cyclability of the process allows higher CO_2 sequestration than CO_2 generation due to calcination of NOS^{251} .

I.3.2.3. Material synthesis

I.3.2.3.1. Standard reagent

Different studies support that NOS-derived CaO powder can be used as a standard chemical reagent and can be classified in the reactive class R4²⁵². Dissolution of CNOS leads to a Ca(OH)₂ solution/suspension that is useful for the preparation of hydroxyapatite²⁵³, unfired fly ash bricks²⁵⁴, mortar²⁵⁵ and nanomaterials like Ca(OH)₂ hydroxide nanoplates (**Fig. 11f**)²¹⁵. Hydroxyapatite can also be obtained by direct solvent-free ball-milling and calcination^{256,257}, an interesting way to produce chemicals with higher added value than NOS.

In the field of nanotechnology, nanomaterials are easily accessible by reacting CNOS with K(MnO₄) to form nanostructured Mn/Ca mixed-oxides decorated with Mn₃O₄ nanoparticles that have potentially high adsorption capacities for Pb(II) and Eu(III)²⁵⁸. Silicate nanofibres prepared hydrothermally with CNOS (**Fig. 11d-e**) are efficient porous absorbent of metal cations, such as Cu(II), Cr(VI)²¹⁶, and anion such as phosphates¹⁶⁰. In the same application field, calcium silicate wollastonite and pseudo-wollastonite were obtained at 1100-1200 °C by

mixing NOS and waste float glass from building demolition. This work represents an additional step towards the synthesis of advanced materials made from 100% waste²⁵⁹.

I.3.2.3.2. Catalyst and support for catalysts

CNOS is potentially attractive for catalysis or co-catalysis in processes that require basic media, a typical case being the transesterification of soybean oil^{260–264}. Very recently, CNOS nanoparticles were employed as a catalyst for the preparation of 1,8-dioxo-octahydroxanthenes via the one-pot condensation of 5,5-dimethylcyclohexane-1,3-dione or dimedone with various aldehydes under solvent-free conditions²⁶⁵. Chemical stability and reusability of CNOS catalysts are among parameters to be investigated.

I.3.2.3.3. Filler in the synthesis of polymer

Applications of CNOS in this area are limited, CNOS powder was reported as a filler in a polypropylene polymer²⁶⁶. Thermal and mechanical properties of this material are comparable to those obtained with commercial CaCO₃, questioning the relevance of calcination.

I.3.2.4. Antibacterial agent

The antibacterial activity of NOS calcined under ohmic heating was evaluated against *E. coli*, *Salmonella* and *Listeria monocytogenes* inoculated on the surface of tomatoes²⁶⁷. CNOS had an efficient antimicrobial activity, higher than that of a preparation with 200 ppm chlorine and distilled water. The antibacterial activity is certainly attributed to the basicity of the preparation due to the hydration of CaO²⁶⁸. This emerging application shows that CNOS is a potential antibacterial agent of interest as a substitute of synthetic commercial chemicals or in the

polymer industry where antibacterial polypropylene/CNOS composites were recently investigated²⁶⁹.

I.3.3. Potential applications of biomolecules extracted from the organic matrix

Frequently described as a set of macro- and low-molecular-weight biomolecules, the organic matrix is actually an extremely complex material whose exact composition, assembly and mechanism of action are not fully defined at the molecular level. The organic matrix can be classified into sets of biomolecules based on their extraction process and solubility, *i.e.*, the water-soluble matrix (WSM), ethanol-soluble matrix (ESM), acid-soluble matrix (ASM), acid-insoluble matrix (AIM), EDTA-soluble matrix (EDTASM), EDTA-insoluble matrix (EDTAIM) and fat-soluble matrix (FSM).

The nature of AIM (initially called conchiolin by Frémy in 1855) has been shown to be proteinaceous and constitutes more than 90% of the organic matrix in the shell of pearl oysters²⁷⁰. ASM and AIM can be obtained after dissolution with acids followed by several separation steps^{270,271}. Calcium-chelating agents, such as EDTA, are also employed at neutral pH. A general protocol was proposed by the research group of Marin which was described to minimise the degradation of proteins and avoids the formation of aggregates^{272,273}. In the nacre of shells of *P. maxima*, the extraction yields of AIM and ASM were 1.20 and 0.17 wt.%, respectively²⁷⁴. WSM extraction from nacre was originally applied and patented by the research group of Prof. Lopez. The extraction method does not allow to recover molecules strongly bound to the mineral phase but is directly compatible with biological purposes such as *in vitro* and *in vivo* trials. The achievable extraction yield varied from approximately 0.2 to 5 wt.%^{275,276}. A method was recently developed to extract and fractionate ESM from the nacre

of shells of *P. margaritifera*²⁷⁷; to the best of our knowledge, the molecular characterisation of ESM has not yet been investigated. In addition, extraction yields were not reported.

Among these extracts, WSM was the most studied but was almost exclusively investigated for its osteogenic activity. The different potential applications of these extracts are summarised in the following subsections.

I.3.3.1. Water-soluble matrix (WSM)

I.3.3.1.1. Bone tissue bioengineering

The osteogenic activity of WSM originally extracted from the powdered nacre of shell of *P. maxima* (50-150 μm) was highlighted by the research group of Prof. Lopez²⁷⁸. WSM was revealed to be osteoinductive, enhancing *in vitro* bone cells differentiation and cellular osteogenic markers. Osteogenic activity studies of WSM were extended to nacre of shells of *P. fucata* and *P. martensii*. As an example, this academic research has been developed in the form of cosmetic and nutraceutical ingredients by the French company StanSea. To the best of our knowledge, no *in vivo* or *in vitro* studies were published on the osteogenic activity of WSM extracted from shells of *Pteria* and Ostreida while the presence of WSM in the shell of *C. gigas* is well known²⁷⁹. Only a few studies have described the relationship between WSM proteins of shells of Ostreida and osteogenic activity^{81,82}. To confirm this assumption, *in vitro* trials are required.

I.3.3.1.2. Other biological activities: antioxidant activity, anti-inflammatory activity and dermal fibroblast regulation

The antioxidant activity of WSM extracted from the nacreous layer of shell of *P. fucata* was investigated in terms of its capacity to scavenge free radicals (DPPH and ABTS tests), to inhibit lipid peroxidation and to reduce damage in human keratinocyte cells after inducing oxidative stress²⁸⁰. The authors showed that WSM can scavenge free radicals in a dose-dependent manner, reducing the effect of oxidative stress in human keratinocytes.

WSM was also tested *in vitro* for its anti-inflammatory and antioxidant activities on mouse macrophages²⁸¹. WSM suppressed or decreased pro-inflammatory factors linked to pro-inflammatory cytokine inhibition and exhibited antioxidant activity. Unfortunately, information on the oyster species used in this study was not presented. For a different purpose, Latire *et al.* (2017) described that WSM extracted from the shell of *C. gigas* can favour the catabolic activities of human dermal fibroblasts *in vitro*²⁷⁹.

In comparison with the numerous osteo-benefits attributed to WSM, these are the only examples found in the literature highlighting other biological properties, and therefore the field is still highly open.

I.3.3.2. Ethanol-soluble matrix (ESM)

Brion *et al.* (2015) originally described the osteogenic effect of ESM from the nacre of shell of *P. margaritifera*^{282,283}. This topic was further investigated *in vitro* by the stimulation of mouse preosteoblasts and human osteoarthritis osteoblasts with ionic fractions of ESM²⁷⁷. This study reveals clues about the cationic nature of the osteogenic compounds found in the nacre of oyster

shells. Proangiogenic effects of ESM were recently obtained *in vitro* on endothelial progenitor cells²⁸³. Comparative osteogenic and scalability studies between ESM and WSM are required knowing that the process by which ESM is obtained did not require a freeze-drying step as it was the case for WSM extraction.

I.3.3.3. Acid-soluble matrix (ASM)

I.3.3.3.1. Prevention of cognitive diseases

Recently, ASM extracted from the nacreous layer of shells of *P. fucata* was tested *in vivo* against scopolamine-induced memory impairment in Wistar rats and ICR mice²⁸⁴. In both cases, ASM improved memory and cognitive impairments, suggesting that ASM can affect brain function by protecting against the dysfunction of glutamate neurotransmission. This mechanism was supported by the examination of the known genes associated with memory.

I.3.3.3.2. Free radical scavenging

A purple organic substance precipitated from a solution of ASM was able to scavenge hydroxyl and superoxide radicals²⁸⁵. With an extraction rate of approximately 2.49 wt.%, this extract could be of great commercial interest, especially for food, nutraceutical or cosmetic products. Unfortunately, the article lacks sufficient experimental details to allow easy reproduction of the protocol.

I.3.3.3. Dermal fibroblast regulation

Latire *et al.* (2017) recently described the regulatory activities of ASM on the metabolism of dermal fibroblasts *in vitro*²⁷⁹. This pioneer work was performed with ASM obtained from the shell of *C. gigas*.

I.3.3.3.4. Material synthesis

Adding supersaturated CaCO₃ solution to ASM extracted from the nacreous layer of shell of *P. margaritifera* produces nanostructured CaCO₃ crystals whose morphology depends on the concentration of ASM²⁸⁶. A protein isolated from the ASM of the nacre from shell of *P. fucata* was employed to induce the formation of aragonite and calcite crystals²⁸⁷. Such innovative results open new pathways for the synthesis of inorganic phases.

I.3.3.4. Acid-insoluble matrix (AIM)

I.3.3.4.1. Natural multifunctional biopolymer

Chitin (poly 2-acetamido-2-deoxy-β-D-glucose) is a non-toxic, biodegradable and biocompatible biopolymer of considerable interest for the pharmaceutical, cosmetic, biochemical, agricultural and food industries. This biopolymer was identified in the AIM of the prismatic layer of shell of *P. fucata*²⁸⁸. Recently, extraction of chitin was reported from undefined raw oyster shell species²⁸⁹, but the reported content of chitin extracted from the shell (69 wt.%) was inconsistent with all other reported mass fractions of the organic matrix in the oyster shell.

I.3.3.4.2. Material synthesis

In the design field of crystal growth, a promising application described the preparation of macro-mesoporous TiO₂²⁹⁰. TiO₂ nanoparticles were grown onto AIM macrotemplate by solgel. The resulting anatase showed interesting photocatalytic activity, especially for samples calcined at 450 °C. However, the chemistry by which AIM and TiO₂ nanoparticles interact was not described. This study shows the prime importance of the shell structure for such material synthesis.

I.3.3.5. EDTA-soluble matrix (EDTASM)

The only application found in the literature regarding the use of EDTASM concerns material synthesis. Calcite and aragonite crystals were selectively prepared with the help of EDTASM proteins extracted from specific microstructures of shells of *C. gigas* (**Fig. 12**)^{28,291}. In this case, a contribution of EDTA to crystal nucleation is not to exclude.

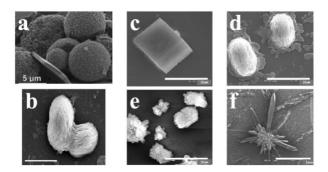


Fig. 12 Examples of materials synthesised with AIM and EDTASM. (a) Hollow spherical particles of CaCO₃ prepared with AIM of shell of P. $fucata^{292}$. (b) Aragonite crystal prepared with EDTASM protein from the myostracum of shell of C. $gigas^{28}$. (c) Calcite crystal prepared without the addition of EDTASM proteins of shell of C. gigas, (d) aragonite crystals prepared with aragonite-specific EDTASM protein extracted from shell of C. gigas, (e) calcite crystals produced with EDTASM calcite-specific protein extracted from the folia of shell of C. gigas, and (f) aragonite crystal produced with EDTASM protein extracted from diseased areas of shell of C. $gigas^{291}$.

I.3.3.6. EDTA-insoluble matrix (EDTAIM)

A single article relates the use of the proteinaceous fraction of EDTAIM to induce aragonite crystals formation in saturated $CaCO_3$ solution with the addition of $Mg^{2+\ 293}$. It is important to note that the aragonite crystals do not grow either without Mg^{2+} or with individual components of the fraction.

I.3.3.7. Fat-soluble matrix (FSM)

Perhaps more unexpected, lipids are part of the shell organic matrix. The research group of Prof. Lopez highlighted that FSM extracted by maceration of nacre with a mixture of methanol and chloroform can promote the restoration of the stratum corneum *in vitro*²⁹⁴.

I.3.3.8. Shell colour related compounds

A potential application is never mentioned in reviews on the topic: the use of pigments and dyes extracted from the oyster shell. Shell colour generally varies from dark-red to brown, and sometimes golden or even pink (**Fig. 13**). In the current industrial context, synthetic pigments and dyes tend to be substituted by natural equivalents, especially in health products. One key challenge to be resolved lies in the identification of compounds at the origin of shell colouration and thus their selective extraction. The presence of melanin extracted in black shell of *C. gigas* is a hypothesis but has not yet been convincingly established²⁹⁵. To date, no biomolecules have been associated with shell colouration other than black excepted for the presence of fluorescent porphyrins in the shells of *Pinctada* and *Pteria*^{296–298}. This innovative recycling of oyster shell is still at the level of fundamental research and lacks of substantial and exhaustive works.

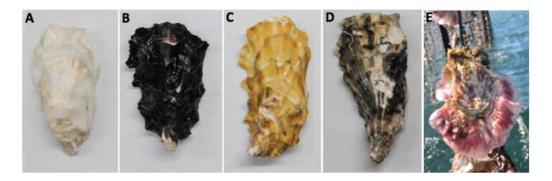


Fig. 13 Shells of *C. gigas* **with six colours.** (a) Whole white shell, (b) whole black shell, (c) whole golden shell, (d) partially coloured shell²⁹⁹. (e) Pink oyster from the French oyster farming Tarbouriech-Médithau (Thau, France)¹.

I.4. CRITICAL ANALYSIS

The economic viability of any recycling process depends on two essential parameters: the cost and the logistic to collect the shell on one hand, and the added-value of the product resulting from recycling on the other hand. The generation of pollutants, emissions or new waste must be minimised in an environmental-friendly philosophy; however, this might be acceptable if the added value of the final product can cover the expend of the treatment in eco-friendly conditions.

So far, oyster shells collection remains to be organised since it is actually considered as a diffuse pollution (generated by consumers, factories and farms). Recently, de Alvarenga *et al.* (2012) examined the LCA of oyster shell waste according two scenarios: *i)* the direct deposit of shells in a landfill or *ii)* the implementation of a simple process to produce CNOS powder (< 20 µm)³⁰⁰. They concluded in favour of the chalk production process. Although this option is strongly dependent on the distance between the source point and the shell-processing facility. The **Fig. 14** gives an overview of possible application fields for the recycling of waste oyster shells.

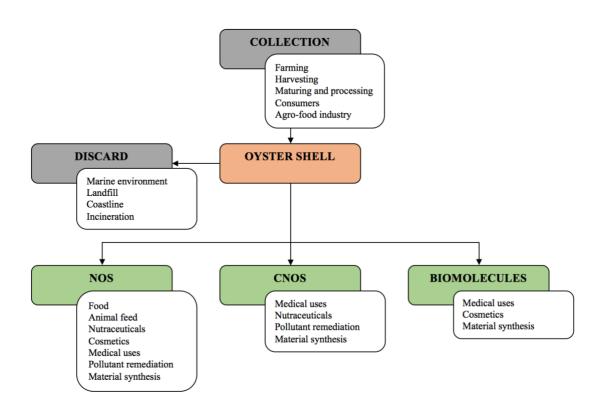


Fig. 14 Application fields of waste oyster shell described in this chapter.

As raw material, NOS is useful for basic applications requiring simple and low-cost processing technologies at large-scale such as animal feeding (**Table 5**). In economic terms, these applications do not bring high added-value but allows to distribute large quantities of NOS with adapted performances. For the other highly documented applications of water and soils depollution, the use of NOS is performant and cheap, but probably requires standardisation of the manufactured product. It also raises the question of the elimination of the resulting contaminated NOS. An alternative remaining to be explored would be to consider the presence of metals at the surface of NOS as a possible catalyst. This would be similar to what has been successfully developed by the team of C. Grison using metal-hyperaccumulating plants to produce metal oxide catalyst³⁰¹.

The use of NOS in building materials or as filler in composites represents an interesting option with more added-value but probably requires here again a standardisation of materials. Besides,

the durability of these materials remains limited, still relatively unknown²⁰⁷, not fully studied and hardly documented.

Other applications with higher economic potential concern NOS and CNOS in material and health fields. NOS as a source of calcium in food requires simple treatments without altering its quality in line with consumer's expectations. The major limit lies in human safety directly related to heavy metals and hazardous chemicals content as a consequence of the possible bioaccumulation of toxics in shell. As an excipient or source of calcium in pharmaceutical products, NOS has to be declared and requires to be proceeded following GMP guidelines. Besides, the real economic advantage of NOS compared to other CaCO3 sources is not always obvious. The answer may probably be driven by a significant shift in mind-sets and ways of working. This is actually the case in cosmetic industry, where the naturalness of ingredient is marketed in a high way range. As cosmetic ingredient, NOS powder has a real interest, especially for its soft abrasive properties (skin soft-peeler) making a potential substitute of plastic microbeads used in cosmetic. This expanding market meets a growing demand for natural, safe and effective ingredients. This may be reinforced if further research demonstrates additional biological activities of NOS, especially of the organic matrix.

Among the applications with high economic value, the use of NOS in bone grafting seems to be a promising route but requires deeper knowledge about long-term biocompatibility and stability. Concerning materials chemistry, NOS is an interesting template of advanced material or support for catalysts as evidenced by the increasing number of publications on this subject. However, the scalability and the repeatability of these applications remains linked to the collection, selection and standardisation of the shell.

The unsustainability of NOS calcination in oven questions the relevance of CNOS, especially since these applications are frequently similar to those with NOS. Few applications reported better performances of CNOS compared to NOS but do not seem high enough to justify the calcination cost and the carbon dioxide emission. Thus, calcination in oven has to be considered only for applications where the required performance level is not achievable with NOS³⁰². In this instance, the development of sustainable calcination processes is needed³⁰³ such as fast microwave calcination²²³, or solar oven combined with carbon dioxide sequestration.

Table 5 Comparative analysis of NOS applications.

Applications and functions	Limits	Challenges
Animal feed – Calcium source	Level of toxic or harmful (heavy metals, pesticides and organic waste). Requires post-treatment (pasteurisation, sterilisation). Low added-value.	
Food – Functional ingredient	Level of toxic or harmful (heavy metals, pesticides and organic waste). Requires post-treatment (pasteurisation, sterilisation).	Interactions with other ingredients. Traceability.
Nutraceutical – Calcium source	Level of toxic or harmful (heavy metals, pesticides and organic waste). Requires post-treatment (pasteurisation, sterilisation).	In vivo clinical studies on absorption and bioavailability highlighting a role of the organic matrix. Comparison with other calcium sources by oral administration. Interactions with other ingredients. Traceability.
Cosmetic – Ingredient	Level of toxic or harmful (heavy metals, pesticides and organic waste). Requires post-treatment (pasteurisation, sterilisation). Powder size and shape.	Identification of potential cosmetic added- value. Role of the organic matrix. Interactions with other ingredients. Traceability.
Pharmaceutical – Calcium source or excipient	Level of toxic or harmful (heavy metals, pesticides and organic waste). Requires post-treatment (pasteurisation, sterilisation). Requires GMP environment.	In vivo clinical studies on absorption and bioavailability highlighting a role of the organic matrix. Comparison with other calcium sources by oral administration. Interactions with other ingredients. Traceability
Bone grafting – Bone substitute	Level of toxic or harmful (heavy metals, pesticides and organic waste). Requires post-treatment (pasteurisation, sterilisation).	Long-term biocompatibility and stability in vivo. In vitro and in vivo osteogenic activity of shell structures other than nacre. Comparison with other calcium sources. Long-term clinical studies. Development of bio-printing. Traceability.
Water treatment – Filter and sorbent	Low added-value.	Adsorbing properties of highly hazardous compounds. Future of the contaminated NOS.
Soil conditioner – pH buffer, sorbent, or fertiliser	Low added-value.	Adsorbing properties of highly hazardous compounds. Future of the contaminated NOS.
Dechlorination of waste -	Low added-value.	Scalability.
Neutraliser	Limited application fields.	Future of the contaminated NOS.
Building material - Limestone and	Low added-value.	Durability of the material.
aggregate		Studies with high substitution level.
Material synthesis – Filler in composite, foaming agent, template, support for catalysts, source of sodium, calcium and calcium carbonate	Low-scalability except for composite synthesis. Use of acidic or thermal treatments.	NOS surface properties and reactivity. Scalability.

Biomolecules of the organic matrix (**Table 6**) are perhaps the best candidates for applications with high value, being entirely competitive with chemical source of calcium carbonate. The high performances of these biomolecules compensate for the low scalability of the extraction process. WSM used as a cosmetic and nutraceutical ingredient commercialised by StanSea is a good example. This research area is still highly open both for the identification of new biological activities for health applications and for the synthesis of innovative advanced materials. The future development of these applications depends on the progress made in the characterisation of these extracts, in particular their composition and mechanisms of action. The difficulty relies on low yields and does not solve the problem of the recycling calcium carbonate wastes, which should be handle together.

Table 6 Comparative analysis of biomolecules applications.

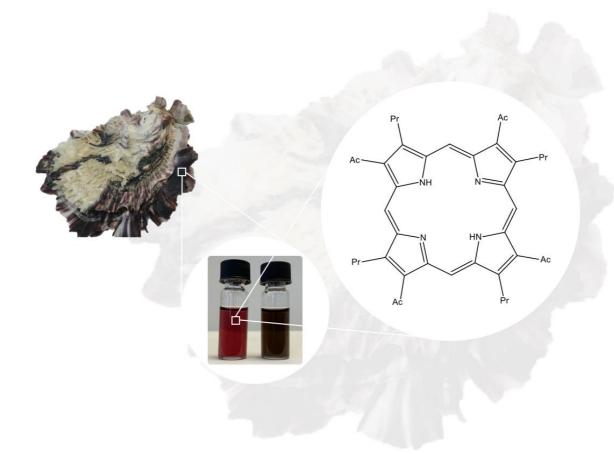
Organic extracts	Limits	Challenges
WSM	Energy required (cold water maceration,	Scalability.
	centrifugation, freeze-drying).	Reduction of processing steps.
	Extraction yield (< 5 wt.%).	Biomolecules identification.
	Variability of the raw material.	Biological activities identification.
	•	In vivo and in vitro osteogenic activities of Ostreidae shells.
		Recycling of by-products.
ESM	Extraction yield (< 5 wt.%).	Scalability.
	Variability of the raw material.	Reduction of processing steps.
	•	Exact composition of the extract.
		Identification of biological activities.
		In vivo and in vitro osteogenic activities of Ostreidae shell.
		Recycling of by-products.
ASM	Use of acids.	Scalability.
	Extraction yield (< 0.2 wt.%).	Exact composition of the extract.
	Variability of the raw material.	Identification of biological activities.
	Production of waste and by-products.	•
AIM	Use of acids.	Scalability.
	Extraction yield (< 2 wt.%).	Exact composition of the extract.
	Variability of the raw material.	Identification of biological activities.
	Production of waste and by-products.	Solubility of the extract.
EDTASM	Use of EDTA.	Scalability.
	Extraction yield (< 5 wt.%).	Exact composition of the extract.
	Variability of the raw material.	•
	Production of waste and by-products.	
EDTAIM	Use of EDTA.	Scalability.
	Extraction yield (< 5 wt.%).	Exact composition of the extract.
	Variability of the raw material.	Solubility of the extract.
	Production of waste and by-products.	·
FSM	Use of toxic organic solvents.	Scalability.
	Extraction yield (< 1 wt.%).	Exact composition of the extract.
	• • •	Identification of biological activities.
		Production of by-products.

I.5. CONCLUSION AND PERSPECTIVES

The globalisation of oyster farming generates short-term profits for local economic actors, but the massive production of shells starts to raise ecological questions. In this context, several studies disclose promising recycling applications from low to high value. The economics of recycling is dominated by the balance between the cost of collection / decontamination / processing and the added value of the product and its use.

This can change due to the great consideration of environmental issues and the demand for natural product from consumers. From depollution of soil and water to bone tissues reconstruction and production of nanomaterials, oyster shell has plenty to offer for chemists. To effectively treat the recycling and recovery of this by-product, diverse issues need to be addressed, especially those related to the variability of composition and microstructures of the shell. Some other aspects still need to be better explored, such as parts of the shell, including pigments and the organic matrix, that still lack detailed characterisation but can lead to new valuations.

II. IDENTIFICATION OF PORPHYRINS IN DARK AND PURPLE PATTERNS OF *Crassostrea gigas*



Despite the functional roles of shell colours in camouflage, thermoregulation or immunity, the molecular mechanisms related to shell colouration remain poorly documented. This gap of knowledge is partly due to the lack of elucidation of the chemical nature of shell pigments, particularly in the genus *Crassostrea*. By combining the identification of shell pigments with corresponding biosynthetic pathways and associated genes, key information on the relation between shell colouration, mineralisation or other molecular mechanisms can be obtained as previously reported in marine snails³⁰⁴. In addition, the identification of shell pigments could lead to the development of a broad range of applications in health or material science as mentioned in the previous chapter.

The colour of oyster shells is a very diverse characteristic morphotype, forming intriguing vivid patterns on the shell of *Crassostrea gigas*. In the present chapter, we report the identification of several porphyrins in the purple and dark patterns of the shell of this oyster. The structure of halochromic, fluorescent and acid-soluble porphyrins, such as uroporphyrin and turacin, were determined by reverse phase liquid chromatography combined with electrospray ionisation-mass spectrometry. We also report preliminary investigation on their origin and propose a specific accumulation by the shell forming tissue (mantle), possibly as haem biosynthesis side-products.

II.1. INTRODUCTION

Pteriomorphian bivalves that include edible and pearl oysters, the distribution of shell colours has been classified by Grant *et al.*³⁰⁵ in eight phenotypes, varying from yellow to orange, red, blue, green, purple, brown and black, more or less associated together, the brown and black colours being often assigned to melanins with poor analytical evidences. Besides, shell colours can result either from pigments such as melanins, tetrapyrroles and carotenoids, but can also be the result of the interference of diffracted light over nanostructured material, known as structural colour. A combination of pigments and structural colour is also possible², this is particularly the case of highly prised shells and pearls of *Pinctada margaritifera* where the iridescent nanostructure of mother-of-pearl is often associated with a fluorescent cyclic tetrapyrrole^{297,306}. So far, little is known about the chemical structure of oyster shells pigments since the early work of the pioneer A. Comfort postulating on the basis of paper chromatography and ultraviolet spectroscopy that uroporphyrin is the major pigment deposited in pearl oysters shells^{307,308}.

Compared to the shell of pearl oysters (*e.g. Pinctada maxima*), the shell of the edible oyster *Crassostrea gigas* has a distinct calcareous microstructural layout with an adductor muscle scar frequently coloured³⁰⁵. Only this small coloured part of the inside shell has been studied for pigment identification³⁰, the other coloured shell patterns totally lacking in-depth chemical studies. In this particular case, melanin polymers have been proposed to contribute to the black colour of the adductor muscle scar (AMS), but the reported data are questionable. Indeed, as a consequence of its low solubility, the chemical investigation of melanin was only based on limited spectroscopic data (infrared and UV spectroscopy). In this regard, the recent investigation on dark AMS of *C. gigas* by mass spectrometry has demonstrated the absence of melanins markers usually obtained after alkaline oxidation (pyrrole-2,3-dicarboxylic acid,

pyrrole-2,3,5-tricarboxylic acid, thiazole-4,5-dicarboxylic acid and thiazole-2,4,5-tricarboxylic acid)³⁰⁹. Identifying pigments associated with black and other frequent shell colours (*e.g.* yellow, red and purple) would constitute an important knowledge on their origin and possible related function. Recently, Feng *et al.*³¹⁰ have evidenced in *C. gigas* the key role of different expressed long non-coding RNA and mRNA transcripts potentially associated with mineralisation and shell pigmentation, among which 6 mRNAs are identified to influence the biosynthesis of pigments including melanins, carotenoids, tetrapyrroles and ommochromes. However, the occurrence of these pigments in *C. gigas* oyster shells remains to be established, as for many other molluscan shells.

In this chapter, we propose to investigate the nature of shell purple and dark patterns of *C. gigas*. This Japanese oyster, introduced in France on large scale, usually displays pink, bright-and dark-purple patterns on its shell, with a natural aestheticism and a marked AMS. In order to distinguish colours due to a structure or to a pigment, shell purple patterns and dark AMS were first investigated by scanning electron microscopy and compared to white patterns as negative controls. A group of tetrapyrroles was identified on the basis of photophysical properties of samples dissolved in acid. Their identification in shell purple patterns and dark AMS was achieved by reverse phase liquid chromatography combined with high-resolution tandem mass spectrometry (electrospray ionisation). The constant progress made in mass spectrometry with adequate chromatographic separation appears as the best standard method, at present, for the unambiguous identification of pigments from complex natural calcareous shells, as recently demonstrated by Verdes *et al.*^{311,312}.

II.2. RESULTS

II.2.1. Morphology and structure of shell purple and dark patterns

II.2.1.1. Morphological description

In order to provide complete information on the nature of coloured patterns of shells of *C. gigas*, we first conducted a visual description of oyster shells at different stages of development from juvenile to adult, collected from different location (**Fig. 15**).



Fig. 15 Photographs of purple patterns distributed on shells of juvenile and adult *C. gigas* collected from France. (a) Decontaminated shells of juvenile oysters bred in Bouin, France (supplied in August 2017). (b-d) Decontaminated shells of juvenile oysters farmed in Marseillan, France (supplied in August 2017 and December 2018). (e-f) Decontaminated shells of adult oysters collected in Ile d'Oleron, France (collected in December 2018). (g-j) Decontaminated shells of adult oysters collected in Marseillan, France (collected in January 2017 and 2018). (k) Adult oyster farmed in Bouzigues, France (purchased in November 2019). (l) Decontaminated valves with dark AMS, farmed in Marseillan, France (collected in August 2017).

In general, epibionts and brown organic periostracum cover the outer mineralised shell layer (**Fig. 15k**)^{305,313}. Shades of the coloured patterns found in shells of *C. gigas* vary from pink to dark-purple and yellow-brown over the whitish calcium carbonate (**Fig. 15a-j**). Purple patterns are random distributions of irregular developing bands and radiating sectors of variable widths usually originating from the beak (**Fig. 16a**). No obvious and specific morphological or macrostructural differences can be observed compared to white patterns. Concerning AMS, in most cases, dark, potentially black or purple-black colours are observed (**Fig. 15l** and **Fig. 16f**), with no systematic correlation with the colour of the outer calcified layer.

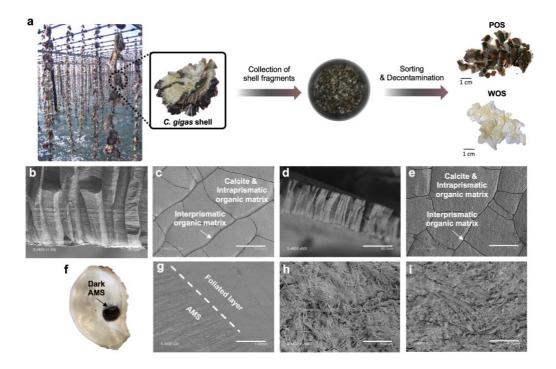


Fig. 16 Schematisation of shell samples collection, preparation and structural characterisation by SEM. (a) Schematic figure of decontaminated WOS and POS collected from adult living *C. gigas* (Thau lagoon, France). (b-c) Characteristic SEM images of decontaminated WOS (cross-section and top view, scale bars = 30 and 20 μm, respectively). (d-e) Characteristic SEM images of decontaminated POS (cross-section and top view, scale bars = 50 and 12 μm, respectively). (f) Representative photograph of a decontaminated dorsal valve with a dark adductor muscle scar (AMS), obtained from waste shells of adult *C. gigas*. (g-i) Characteristic SEM images of decontaminated dark AMS (top views, scale bars = 1 and 6 μm).

II.2.1.2. Structural description

Although not identifiable by naked eyes, we speculated on a possible structural colour related to purple patterns and dark AMS at micro- or sub-micrometre scale. We also wanted to check whether, in the case of colouration resulting from a pigmentation, the latter was associated with any structural modifications of the shell at the submicron scale. While the layout of shells of *Pinctada* spp. is made of an inner iridescent nacreous and an outer prismatic layer often associated with melanins deposition^{314,315}, the calcitic shell of *C. gigas* consists of a prismatic outer layer and a foliated inner layer more or less interrupted by chalky deposits (**Fig. 17**).

Epibionts (*e.g.* diatoms, rhodophytes or chlorophytes) and periostracum may contribute to orange, red, blue, green and brown colours^{305,313}, therefore they are removed by decontamination (detailed in Chapter IV) before scanning electron microscopy (SEM) analysis of white oyster shell fragments (WOS), purple oyster shell fragments (POS) and dark AMS. Both WOS and POS are constituted by the typical columnar prismatic structure of shells of edible oyster (**Fig. 16b-e**), known to be the richest in organic matrix among microstructures occurring in molluscan shells³¹⁶. At micron scale, no specific structure-colour relationship can be observed. In contrast, AMS has specific networks of fibres, needles and pores (**Fig. 16f-i**). This structural layout is clearly different from the columnar prismatic structure of WOS and POS. At this stage, we hypothesise that POS colouration is due to the deposition of one or more pigments and that no specific microstructure is associated with this pigmentation since no differences are observed by comparison with the negative colour control (WOS). In contrast, it is more difficult to be as affirmative concerning AMS of a different microstructure.

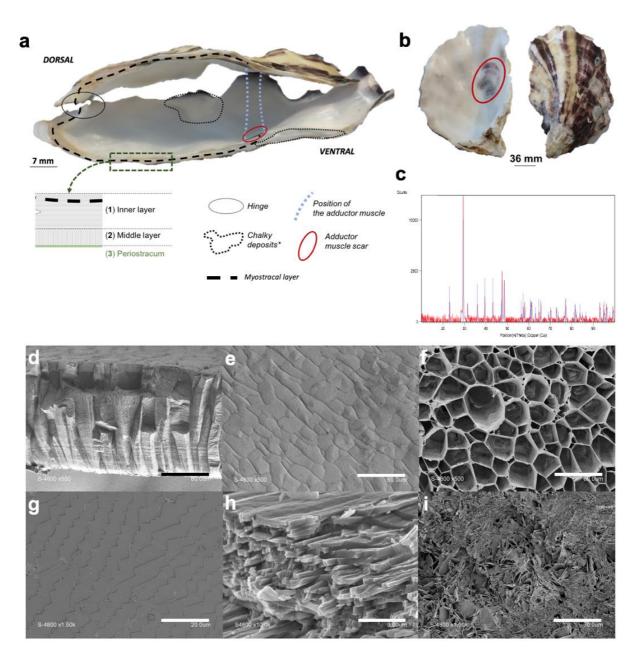


Fig. 17 Schematic of the structure of shell of adult *C. gigas*. (a) Cross-section with a scheme of the shell layout. (b) Purple AMS of a ventral valve. (c) XRD powder diffractogram of decontaminated and powdered shell of *C. gigas* (red) superimposed with a reference diffractogram of calcite. (d-e) Characteristic SEM images of decontaminated outer prismatic layer (cross-section and top view, respectively). (f) Characteristic SEM image of the interprismatic organic matrix obtained after dissolution of POS in 1M HCl_(aq). (g-h) Characteristic SEM images of decontaminated inner foliated layer (top view and cross-section, respectively). (i) Characteristic SEM image of decontaminated chalky structure interrupting the foliated inner layer.

II.2.2. Photophysical properties

II.2.2.1. Solid-state fluorescence of shell purple and dark patterns

Fluorescence in molluscan shells is generally attributed to photoluminescent tetrapyrroles like porphyrins². To date, no other groups of fluorescent pigments extracted from mollusc shells have been reported. Porphyrins are highly fluorescent in solution, but in solid state, their aggregation leads to fluorescence quenching, a well-documented property resulting from π -stacking^{317,318}. Binding with proteins may also result in fluorescence quenching³¹⁹. In the Pteriomorphia group, limited to oysters, the emission of bright pink-red fluorescence has only been reported from the shell of *Pinctada vulgaris* exposed to UV light at approximately 400 nm³²⁰. In our study, under three different monochromatic lights $\lambda \sim 254$, 366 and 400 nm, no fluorescence is observed from WOS, POS, AMS and the black shell of *Pinctada margaritifera*. This is in contrast with the brown-purple patterns on shells of *Pinctada radiata* under $\lambda_{ex} \sim 400$ nm, where a pink-red photoluminescence is emitted (**Fig. 18**).

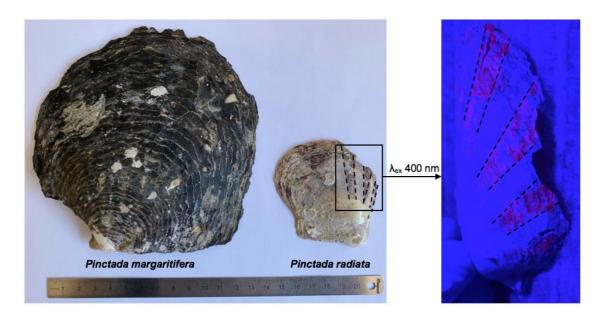


Fig. 18 Pink-red fluorescence of the brown-purple patterns of a shell of *Pinctada radiata* under 400 nm. The black shell of *Pinctada margaritifera* emits no photoluminescence.

II.2.2.2. Fluorescence and UV-visible analysis of acidic solutions of dissolved shell samples

At this stage, we undertook to study the fluorescence and UV-visible absorption properties of acidic solutions of shell samples dissolved in acids. The dissolution of POS result in a purple-red suspension in 1M $HCl_{(aq)}$ (pH ~ 1) and purple-dark in 1M $AcOH_{(aq)}$ (pH ~ 5), revealing a halochromic or ionochromic property of acid-soluble pigments (**Fig. 19a**). Besides, solid residues of the acid solution are isolated as colourless soft materials. Their examination by SEM reveals a polygonal structure related to the interprismatic organic matrix of the prismatic microstructure (**Fig. 17f**).

This general behaviour is also observed on the acid solution of AMS. In contrast, the dissolution and filtration of WOS results in a colourless solution (**Fig. 19b**). These data support the first hypothesis that colours of shell purple patterns and AMS are not the result of a specific mesostructuration of the shell but are due to acid-soluble pigments. The halochromic or ionochromic property of such shell pigments is fully compatible with bile pigments and porphyrins³²¹.

After acid dissolution and filtration, solutions of WOS (ASM^{WOS}), POS (ASM^{POS}) and AMS (ASM^{AMS}) are exposed to a monochromatic light at $\lambda \sim 400$ nm (**Fig. 19b**). Unsurprisingly, no photoluminescence is emitted by ASM^{WOS}. On the opposite, a bright pink photoluminescence is observed from ASM^{POS} and ASM^{AMS}. The pattern of the emission spectrum of ASM^{POS} at $\lambda_{ex} = 405$ nm has a three-peak profile in the 550-750 nm range (**Fig. 19c**), similar with those of carboxylic acid porphyrins reported in the literature from natural and biological samples^{322,323}.

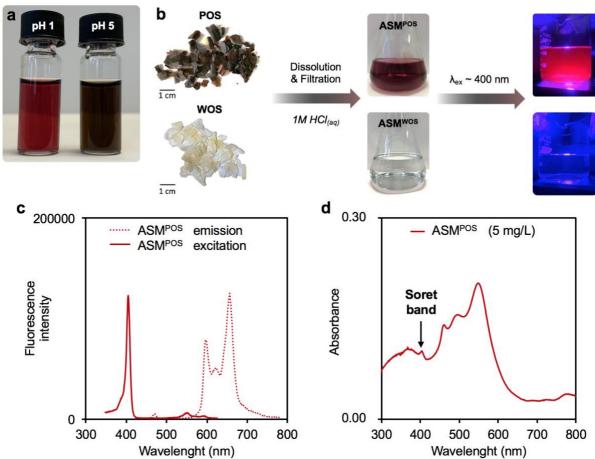


Fig. 19 Photophysical properties of shell samples of *C. gigas*. (a) Photograph of the halochromic or ionochromic property of POS dissolved in 1M $HCl_{(aq)}$ (pH ~ 1) and 1M $AcOH_{(aq)}$ (pH ~ 5). (b) Schematisation of the protocol for photoluminescence investigation on WOS an POS dissolved in 1M $HCl_{(aq)}$. (c) Excitation and emission spectra of ASM^{POS} . (d) UV-vis absorption spectrum of ASM^{POS} .

UV-vis adsorption spectroscopy provides additional information (**Fig. 19d**). The ASM^{WOS} does not absorb in the visible region (**Fig. 79** – **experimental part**). The shoulder observed at 404 nm in the ASM^{POS} absorption spectrum matched the Soret band of fluorescent carboxylic acid porphyrins described in the literature, such as uroporphyrin³¹⁹. The supplemental absorption bands at 464, 496 and 552 nm with higher intensities than the Soret band can be explained by multiple factors. First, a mixture of different types of porphyrins (free-base or metaled) may have different Soret band and Q-bands values. Second, aggregations of porphyrins due to the ionic strength of ASM^{POS} containing Ca²⁺, are well known to form additional absorption bands

in visible region and/or to increase/decrease the Soret band intensity^{324,325}. Third, the presence of multiple absorbing species associated with porphyrins by complexation and/or ionic interactions, may lead to superposition of individual absorption spectrum as already observed with mixtures of melanins and porphyrins³²⁶. However, the absorption spectrum of ASM^{AMS} is less exploitable, certainly due to the low concentration of absorbing species (**Fig. 80b** – **experimental part**). Only the absorption bands at 496 and 552 nm are observed in the visible region. Despite the emission of photoluminescence under $\lambda_{ex} \sim 400$ nm, the Soret band is not observable.

II.2.3. Analysis of acid solutions obtained from shell purple and dark patterns

II.2.3.1. Composition profile of ASMPOS

Reverse phase liquid chromatography (RPLC) combined with electrospray ionisation high-resolution mass spectrometry (HRMS) is a method recently and successfully applied by Verdes *et al.* to identify molluscan shell pigments³¹¹. Similarly, we undertook these analyses to access to the exact mass and molecular formula of ionisable pigments. Briefly, after separation, compounds are infused into the electrospray ionisation source for the generation of a charge by protonation/deprotonation and are transferred to gaseous phase³²⁷. The ionic compound is then analysed by a high-resolution mass spectrometer, in that case a single quadrupole time-of-flight analyser that allows a determination of the m/z (mass to charge ratio) of the ion with an accurate mass measurements within the ppm range. In addition, it also gives information on the isotopic distribution of the ion, useful to identify particular elements with abundant isotopes. Given the complex set of molecules constituting a natural sample, the main limitation of such analysis is the large amount of data to proceed and more particularly the selection of ions of interest during post-acquisition data processing and interpretation.

The composition of ASM^{POS} was investigated by RPLC-DAD-HRMS in electrospray positive ionisation mode (ESI+). This mode of ionisation was preferred since a vast majority of compounds are more easily ionisable in ESI+ than in negative mode (ESI-). UV-vis detection fixed at 405 nm was chosen in order to identify the retention time of potential tetrapyrroles, 405 nm corresponds to the Soret band of fluorescent acid-soluble tetrapyrroles previously suspected. The resulting chromatographic profile displays a high number of compounds eluted from 6 to 15 min (**Fig. 19a**). The examination of their corresponding mass spectrum indicates that compounds eluted from 7.5 min to 11.5 min are characterised by clusters of multiple charged ions (z = 2 and 3) in the 500-850 m/z range (**Fig. 19b-c**). Their exact mass, varying from 1039.2924 to 1563.2572 Da, are significantly higher than those reported for known acid-soluble tetrapyrroles in molluscan shells (< 1000 Da)². These compounds are detailed in Chapter III.

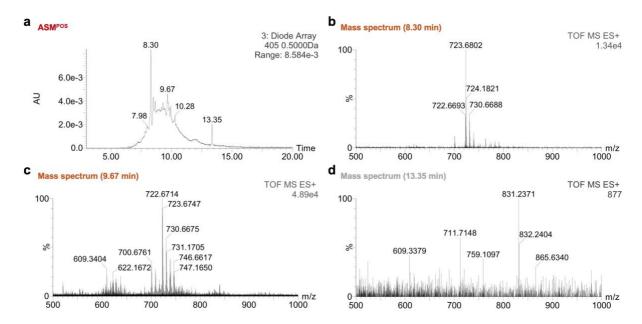


Fig. 19 Composition profile of ASM^{POS}. (a) Chromatogram obtained at 405 nm. (b-d) Mass spectra of compounds eluted at 8.30, 9.67 and 13.35 min, respectively.

The mass spectrum of the peak eluted at 13.35 min is considerably simpler than the previous ones, however, the intensity of the signal is relatively low (877, **Fig. 19d**). In particular, the molecular ion at m/z 831.2371 (exact mass of 830.2293 Da), is in agreement with the theoretical exact mass of uroporphyrin (830.2283 Da, C₄₀H₃₈N₄O₁₆, **Fig. 20**) since the accuracy of the measure is \pm 0.0030 Da. However, 20 substances are referenced in SciFinder for this molecular formula, almost exclusively corresponding to macrocyclic tetrapyrroles. Therefore, these mass spectrometry data alone are not sufficient to establish unambiguously the presence of uroporphyrin. A comparative analysis with a chemical standard is required.

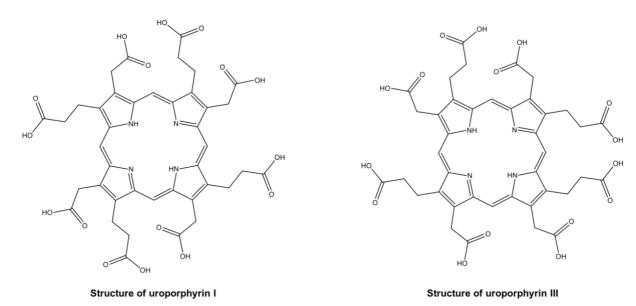


Fig. 20 Structure of uroporphyrin I and III.

II.2.3.2. Identification of uroporphyrin in ASM^{POS}

The identification of porphyrins in ASM^{POS} is further investigated by comparison with a chemical standard of uroporphyrin I and ASM^{WOS} as a negative control. Given the high number of compounds eluted before the hypothesised uroporphyrin peak, the chromatographic separation was improved by adjusting the gradient system to limit the risk of co-elution (the gradient separation has been elongated). The molecular ion of hypothesised uroporphyrin is detected in ASM^{POS} (*m*/*z* 831.2365, retention time of 29.04 min, Fig. 21a-b) and is in good agreement with the isotopic distribution of the uroporphyrin standard ([M+H]⁺ monoisotopic peak at *m*/*z* 831.2365, proton+1: p+1 peak, proton+2: p+2 peak, retention time of 28.66 min, Fig. 21c-d). The minor shift of retention time between ASM^{POS} and the standard can be due to different isomers which do not elute at the exact same retention time. It shows with a good level of confidence that the fluorescent acid-soluble porphyrin can be attributed to uroporphyrin. In contrast, no signal corresponding to the *m*/*z* of uroporphyrin molecular ion was detected in ASM^{WOS} (Fig. 21e-f), suggesting that the presence of uroporphyrin is specific to shell purple patterns.

In natural shell samples, only the isomeric type I and type III of carboxylic acid porphyrins are described³¹⁹ (**Fig. 20**). At this stage, it is not possible to ascribe the isomeric form of uroporphyrin identified in ASM^{POS} solely on the basis of mass spectrometry.

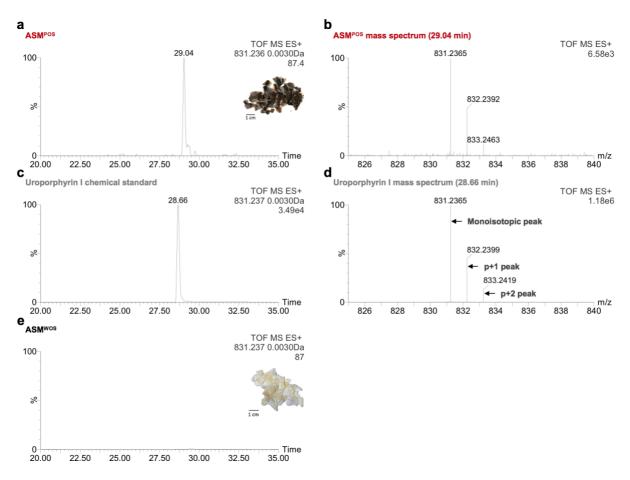


Fig. 21 RPLC-HRMS analysis of ASM^{POS}, **ASM**^{WOS} **and a commercial standard of uroporphyrin I.** (a-d) Chromatograms of extracted uroporphyrin ion with the corresponding mass spectrum showing the molecular isotopic distribution, in ASM^{POS} and the commercial standard, respectively. (e) Chromatogram of extracted uroporphyrin ion ASM^{WOS} with no signal.

II.2.3.3. Identification of uroporphyrin in dark AMS

The previous UV-vis absorption analysis of ASM^{AMS} (**Fig. 80b** – **experimental part**) suggests that the concentration level of acid-soluble porphyrins might be below the detection limit in current RPLC-HRMS conditions. In order to allow their detection and characterisation, an extraction method was developed to eliminate the calcium salt of the ASM^{AMS} by calcium fluoride precipitation with aqueous hydrofluoric acid (HF). This treatment, detailed in Chapter IV, enabled to prepare a sample with organic species up to 10 mg/mL. The RPLC-DAD-HRMS

(ESI+) analysis of the extract obtained from ASM^{AMS} shows the presence of the expected uroporphyrin molecular ion but also the detection of heptacarboxylic acid porphyrin molecular ion (respectively m/z 831.2362, retention time of 28.06 min and m/z 787.2471, retention time 28.93 min, **Fig. 80c-f** – **experimental part**). These data provide an evidence of the identification of uroporphyrin and derivatives in AMS of shells of *C. gigas*.

II.2.4. Chemical confirmation of uroporphyrin and derivatives in ASM^{POS}

In order to identify other potential acid-soluble porphyrins from shell purple pattern as hypothesised by the UV-vis absorption analysis of ASM^{POS} , sample decalcification is achieved by CaF_2 precipitation with $HF_{(aq)}$ prior to RPLC-DAD-HRMS (ESI+) analysis.

This approach allows to concentrate acid porphyrins in the sample. Indeed, starting from the retention time corresponding to the elution of uroporphyrin, an entire set of more or less carboxylated and hydroxylated porphyrins can be identified based on the m/z of their molecular ions (**Fig. 22**). This set of porphyrins is classified as major and minor porphyrins in **Table 7**. The higher retention time compare to uroporphyrin can be ascribed to porphyrins with a reduced number of carboxyl groups on the side chain substituents that interact with the mobile phase. The presence of isomers is another possible explanation. Indeed, as shown in the literature with the example of uroporphyrin and derivatives^{319,328–331}, the type III isomers has two successive acetic acid and two successive propionic side chains substituted on the macrocycle, unlike type I which is characterised by an alternation of acetic and propionic acid side chains (**Fig. 23**). Thus, the chains of same size located side by side are more prone to interact together, which results in a slightly delayed elution of type III isomers compared to the type I forms.

Table 7 Major and minor carboxylic acid porphyrins potentially identified in the extract obtained from $\mathbf{ASM}^{\mathbf{POS}}.$

Major carboxylic acid porphyrins	Retention time (min)	Calculated exact mass (± 0.003 Da)	m/z observed [M+H] ⁺	m/z calculated [M+H] ⁺
Uroporphyrin I & III $C_{40}H_{38}N_4O_{16}$	28.40 & 28.69	830.2283	831.2377 & 831.2356	831.2361
Heptacarboxylic acid porphyrin I & III $C_{39}H_{38}N_4O_{14}$	29.33 & 29.58	786.2384	787.2458 & 787.2485	787.2463
Turacin I & III C ₄₀ H ₃₆ N ₄ O ₁₆ Cu	29.58 & 29.76	891.1422	892.1512 & 892.1498	892.1501
Minor carboxylic acid porphyrins	Retention time (min)	Calculated exact mass (± 0.003 Da)	m/z observed [M+H] ⁺	m/z calculated [M+H] ⁺
Hydroxy-heptacarboxylic acid porphyrin $C_{39}H_{38}N_4O_{15}$	28.23	802.2333	803.2430	803.2412
Hydroxy-hexacarboxylic acid porphyrin $C_{38}H_{38}N_4O_{13}$	29.00	758.2435	759.2573	759.2514
Ketoacid heptacarboxylic acid porphyrin $C_{39}H_{36}N_4O_{15} \label{eq:c39}$	30.03	800.2177	801.2264	801.2255
Hexacarboxylic acid porphyrin $C_{38}H_{38}N_4O_{12} \label{eq:c38}$	30.18	742.2486	743.2563	743.2564
$Cu(II) heptacarboxylic \ acid \ porphyrin \\ C_{39}H_{36}N_4O_{14}Cu$	31.21	847.1524	848.1592	848.1602
Pentacarboxylic acid porphyrin $C_{37}H_{38}N_4O_{10} \label{eq:controller}$	32.40	698.2589	699.2664	699.2666
Coproporphyrin $C_{36}H_{38}N_4O_8$	32.50	654.2690	655.2742	655.2768

By order of elution, major porphyrins are proposed as uroporphyrin (C₄₀H₃₈N₄O₁₆, **Fig. 23**), heptacarboxylic acid porphyrin (C₃₉H₃₈N₄O₁₄, **Fig. 23**) and turacin (C₄₀H₃₆N₄O₁₆Cu, **Fig. 23**), with type I isomers eluted before the corresponding type III (**Fig. 22a-j**). Turacin, a coppermetallised uroporphyrin³³², is proposed here on the basis of the *m/z* of its molecular ion and its isotopic distribution which shows the presence of an abundant isotope such as ⁶⁵Cu (**Fig. 22i-j**).

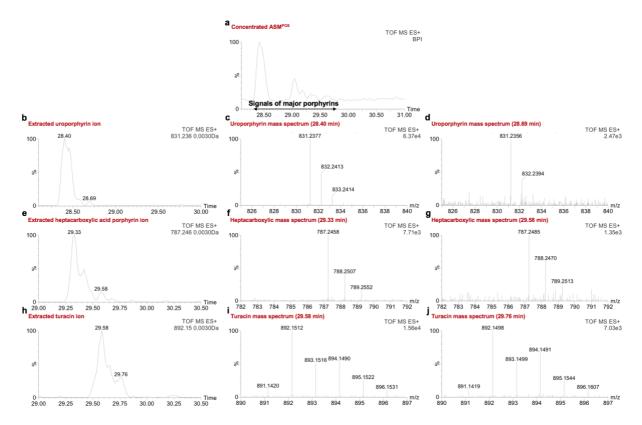


Fig. 22 Proposed identification of major porphyrins in the extract obtained from ASM^{POS}. (a) Elution profile of major porphyrins. (b-d) Chromatogram of extracted uroporphyrin ions with corresponding high resolution mass spectra. (e-g) Chromatogram of extracted heptacarboxylic acid porphyrin ions with corresponding high resolution mass spectra. (h-j) Chromatogram of extracted turacin ions with corresponding high resolution mass spectra.

More surprisingly, the molecular ion of Cu(II)-metallised heptacarboxylic acid porphyrin can also be proposed from the set of minor porphyrins (**Fig. 81d** – **experimental part**). This is the first case of detection of this porphyrin in a natural sample. Minor porphyrins are proposed as hexacarboxylic and pentacarboxylic acid porphyrins, coproporphyrin and traces of hydroxylated and isomeric forms (**Fig. 81** – **experimental part**).

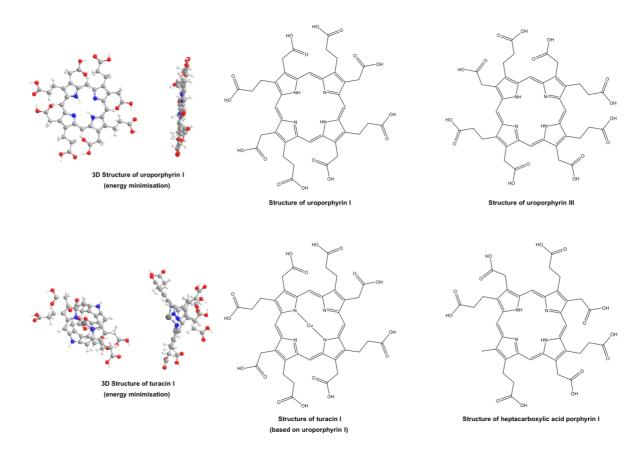


Fig. 23 Structure of major porphyrins. Energy minimisation was predicted by ChemDraw (Ultra 12.0).

The confirmation of the chemical nature of major porphyrins is conducted by tandem mass spectrometry (MS/MS). Briefly, in MS/MS, a specific ion of interest, detected during the first stage of mass detection, is selected to collide with an inert collision gas, argon in that case. The ion is in an excited state, decomposes immediately and is converted into product ions³²⁷. For a given ion, the decomposition depends mainly on the energy of collision. In the case of protonated or deprotonated compounds, two fragmentation mechanisms are possible, charge retention and charge migration³²⁷. It indicates that in general, the difference of mass between a parent ion and its product ions correspond to a neutral molecular loss. In these conditions, only the carboxylated side chains of porphyrins can be observed as neutral loss resulting from fragmentation^{330,333}. The fragmentation by these mechanisms does not allow to "break" the conjugated macrocyclic structure of porphyrins.

The MS/MS spectra of major porphyrins are in agreement with this theoretical background. Indeed, only the carboxylic acid side chains are fragmented (**Fig. 24**), corresponding to neutral loss of CH₃CO₂H and HCO₂H systematically observed. Neutral loss of CH₃CH₂CO₂H side chains are also observed. These fragmentations are in agreement with those reported in in the literature^{330,333}, and support the identification of uroporphyrin, heptacarboxylic acid porphyrin and turacin.

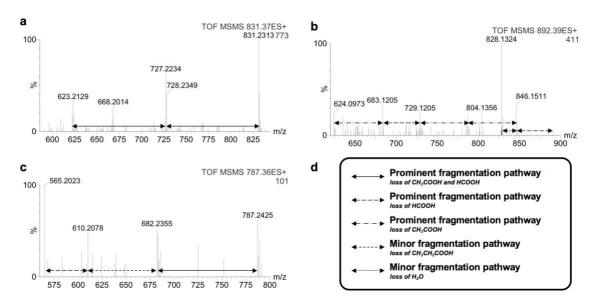


Fig. 24 MS/MS of major porphyrins. (a-c) MS/MS spectra of uroporphyrin, turacin and heptacarboxylic acid porphyrin I or III ions, respectively. (d) Fragmentation pathways of carboxylic acid porphyrins.

A study by NMR spectroscopy was initiated with the objective to unambiguously confirm the identification of carboxylic acid porphyrins, and to possibly elucidate one or more isomeric forms. Metal-free porphyrins, such as uroporphyrin, have a very characteristic signature in ¹HMR spectroscopy, the proton of NH groups being observable in the range of negative chemical shifts³³⁴. Indeed, the uroporphyrin I standard presents a signal at -3.90 ppm (**Fig. 25b**).

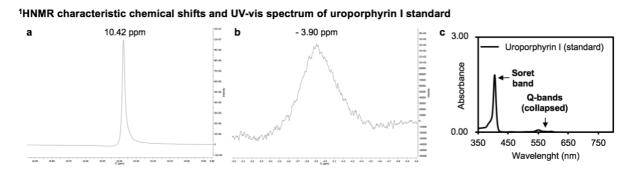
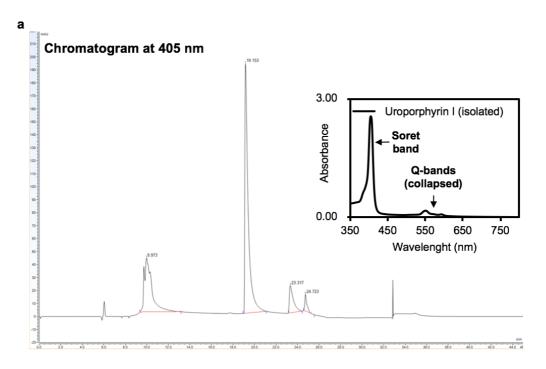


Fig. 25 Characteristic ¹HMR chemical shifts and UV-vis spectra of uroporphyrin I standard. (a-b) Proton chemical shifts of COOH and NH of uroporphyrin I standard. (c) UV-vis absorption spectrum of uroporphyrin I standard.

Several purification experiments were conducted by preparative chromatography on the sample obtained by CaF₂ precipitation for the isolation of major porphyrins, but were not sufficient for ¹HMR experiments. Consequently, we prepared a sample concentrated in porphyrins by separation on C18 grafted silica gel in open column, this method being detailed in Chapter IV. The resulting porphyrin-rich fraction is further separated by semi-preparative chromatography (**Fig. 26a**), several runs of isolation allowed to obtain a sample sufficiently concentrated to observe the characteristic NH chemical shift at -3.90 ppm (**Fig. 26c**). The chemical shift at 10.40 ppm, corresponding to COOH is also comparable to that of uroporphyrin I standard (**Fig. 26a and 25a**). If this result suggests that uroporphyrin isolated by semi-preparative chromatography is the type I isomer, a comparative analysis with a type III standard is required since the only structural variation resides in the alternation of the carboxylic acid side chain substituents. To date, only the esterified type III derivative is commercially available.



¹HNMR characteristic chemical shifts and UV-vis spectrum of isolated uroporphyrin

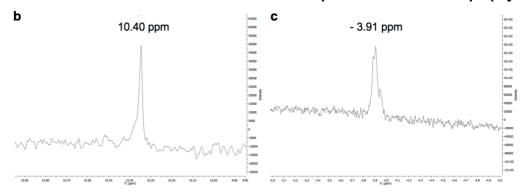


Fig. 26 Purification of uroporphyrin.

II.2.5. Identification of uroporphyrin in the shell forming tissue

The identification of porphyrins raises many questions on their origins and functions. Are they synthesised by the oyster? Are they accumulated from the aquatic environment? How are they transported to the shell? How do they contribute to shell mineralisation? Do they result from a particular metabolism, influenced by exogenous factors such as diet and salinity, or endogenous factors like shell formation or respiration? In order to identify some possible preliminary answers, we examined the tissues of an adult oyster.

Upon observation, the light milky colouration of most organs is apparently unrelated to colours of the shell. Only viscera and the edge of the mantle have strong dark and brown colours which drew our attention to a possible link with colours of the shell. The colour of the mantle edge turns purple-red in contact with concentrated HCl_(8q) (**Fig. 27a**), suggesting a possible connection with shell pigmentation. Consequently, the mantle edge epithelium (MEE) was collected from adult specimens (n = 10 animals), freeze-dried and subjected to immersion and agitation in 1M HCl_(8q). The identification of porphyrins in the acidic extract (ASM^{MEE}) is first suggested by its pink photoluminescence under a monochromatic light at $\lambda \sim 400$ nm (**Fig. 13b**). Furthermore, its absorption spectrum in the visible region is similar to that ASM^{POS} in **Fig. 19d** (a shoulder at 406 nm and supplemental bands at 464, 496 and 552 nm in **Fig. 27c**), The analysis of ASM^{MEE} by RPLC-HRMS allows to identify the molecular ion uroporphyrin (m/z 831.2346, retention time of 28.60 min, **Fig. 27d-e**). These findings indicate that purple and dark colours of the shell have an important connection with the mantle, known to control the shell mineralisation.

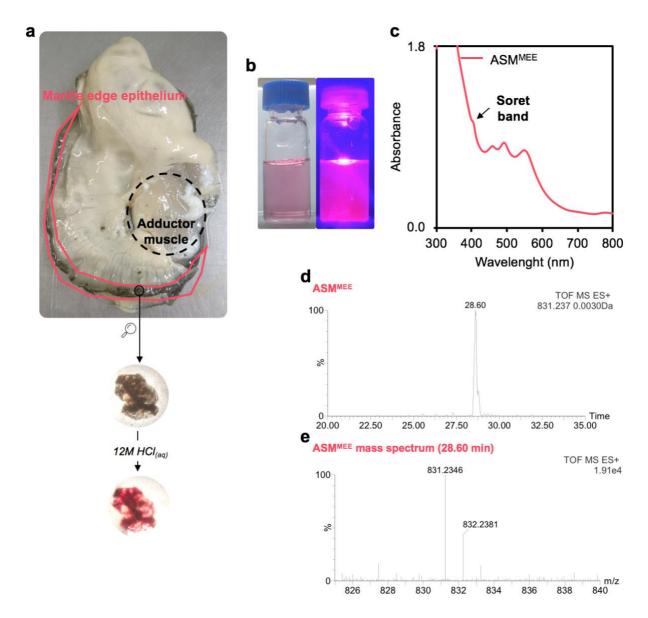


Fig. 27 Identification of uroporphyrin in the mantle edge epithelium (MEE) of *C. gigas*. (a) Location of the brown-to-black secretions of the MEE, turning red in concentrated $HCl_{(aq)}$. (b) Pink photoluminescence of ASM^{MEE} at $\lambda_{ex} \sim 400$ nm. (c) UV-vis absorption spectrum of ASM^{MEE} . (d-e) Chromatogram of the extracted uroporphyrin ion from ASM^{MEE} with the corresponding high resolution mass spectrum.

II.2.6. Identification of chlorophyll catabolites in viscera

Viscera, including intestine, are the only other coloured tissues of *C. gigas* (**Fig. 28a**). Viscera (VOT) from 10 animals were collected and freeze-dried. After immersion in 1M $HCl_{(aq)}$, the acidic extract (ASM^{VOT}) emits a red photoluminescence under a monochromatic light at $\lambda \sim 400$ nm. Its absorption spectrum has a broad band at 417 nm and a weaker band at 667 nm (**Fig. 28b**), which are characteristics of the Soret band and Q-bands of chlorophyll a and derivatives³³⁵. No signals corresponding to the carboxylic acid porphyrins ions previously identified are observed from the RPLC-HRMS analysis of ASM^{VOT}. On the other hand, molecular ions corresponding to degradation products of chlorophyll (catabolites) are observed, forming characteristic dimer ions (**Fig. 28c-e**)³³⁶. Chlorophyll catabolites certainly derive from the digestion of chlorophylls as a result of the algae-based diet of oysters. These findings converge towards the MEE-specific accumulation of carboxylic acid porphyrins.

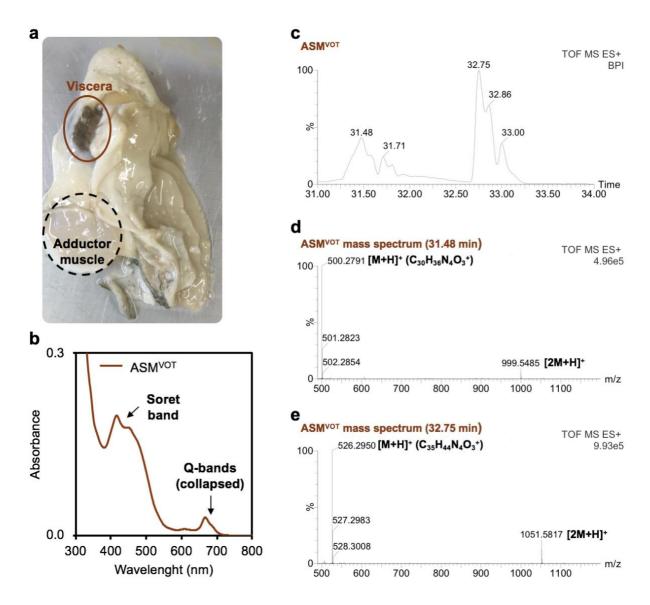


Fig. 28 Identification of chlorophyll catabolites in viscera of *C. gigas.* (a) Location of the brown viscera. (b) UV-vis absorption spectrum of ASM^{VOT}. (c-e) Chromatogram of ASM^{VOT} showing signals of chlorophyll catabolites and corresponding high resolution mass spectra.

II.3. DISCUSSION

Shell colours is supposed to result from a periodic and repetitive deposition of pigments into the shell, a process achieved by the secretory cells of the mantle edge epithelium³³⁷. In this chapter, we have observed that the shell purple patterns of *C. gigas* are characterised by a random distribution of irregular developing bands and radiating sectors of highly fluctuating widths. We also noticed high variability in the distribution of the purple colour from one specimen to another. We have identified a set of porphyrins in different parts of the edible oyster *C. gigas*, with a possible correlation between the purple pigmentation of outer shells, the dark colour of adductor muscle scars and the mantle edge epithelium. Conversely, none of these porphyrins were identified in viscera, suggesting their MEE-specific accumulation or origin. Chlorophyll catabolites, a class of porphyrins, were identified in viscera, thus a possible relation with porphyrins identified in the mantle cannot be ruled out.

Recently, the pink-red and yellow-brown colours of shells of marine snails have been attributed to carboxylic acid porphyrins³¹⁹, such as those proposed in our study. These porphyrins are considered as side products of the haem biosynthetic pathway in marine snails³⁰⁴. Haem is a well-known porphyrin complexed with Fe(II), able to transport oxygen indispensable for cellular aerobic respiration. The haem biosynthetic pathway consists of a succession of reactions enzymatically driven. The non-enzymatic side path leads to the production of uroporphyrin and derivatives by the oxidation of uroporphyrinogen I and III (**Fig. 29**).

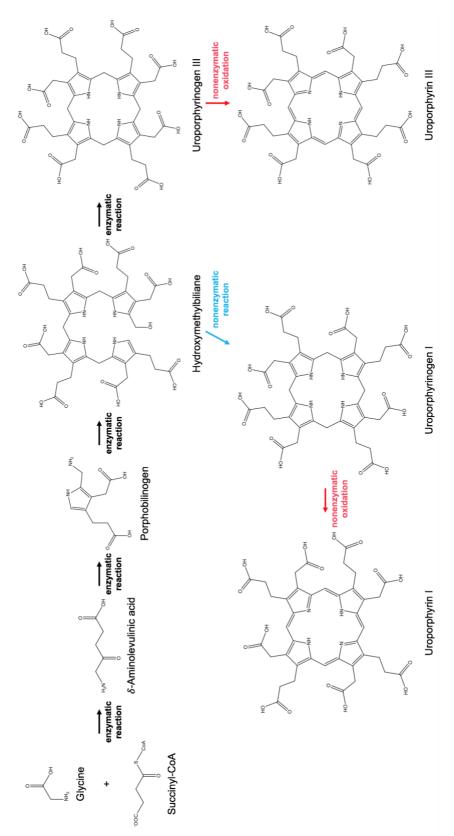


Fig. 29 Schematic representation of the fourth first enzymatic-catalysed reactions of the haem biosynthetic pathway including the non-enzymatic side path³⁰⁴.

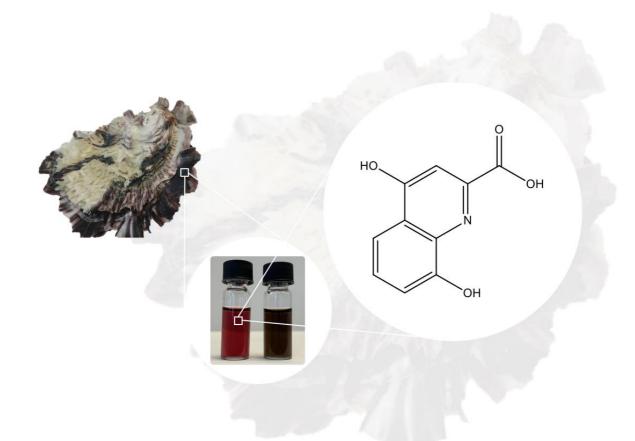
Accordingly, a similar process could occur in the present case of *C. gigas*, oyster shell porphyrins may derive from the non-enzymatic oxidation of uroporphyrinogen I and III associated with the cellular respiration of the shell forming tissue, especially in periods of high loading. This assumption is supported by the recent elucidation of the *C. gigas* genome where genes associated with enzymes of the haem pathway are expressed, such as ferrochelatase, protoporphyrinogen oxidase, or delta-aminolevulinic acid dehydratase³³⁸.

As we see, the synthesis pathways of these pigments begin to emerge, however the mechanism of their deposition in the shell is an open issue, closely related to shell mineralisation. From a material science point of view, it has been reported that carboxylate-containing molecules are possible structure directing agents that can preferentially adsorb on calcium carbonate and orient the crystal growth³³⁹. Also, monolayers of an amphiphilic porphyrin bearing carboxylic acid groups are reported to nucleate calcite³⁴⁰. Therefore, a possible scenario may be the production of uroporphyrin and its derivatives resulting from the oxidation of uroporphyrinogen I and III, especially during periods of high activity of the respiratory cells of the contractile tissues of MEE and adductor muscle. These porphyrins being then integrated into the shell structure by the ionic binding between carboxylate groups and Ca²⁺. Uroporphyrin and derivatives are necessarily present in the shell mineralisation matrix, possibly as a mineralisation cofactor, in addition to achieving, supporting or catalysing one or more biological functions. Another option would be a kind of recycling of this metabolic wastes into the shell formation process. At present, we must admit that the reason or function of this colouration is absolutely not understood. It can be noticed that among juvenile and adult edible oysters, purple is a common colour of the outer shell but not systematically found. During the early stages of mineralisation when the shell is thin, shell colouration may provide protection from sunlight, especially at low tide.

II.4. CONCLUSION AND PERSPECTIVES

The discovery of natural source of porphyrins offers here an opportunity to give more value to waste oyster shells. Although extraction yield and purification still need to be improved, the extraction of porphyrins may have significant potentials for biotechnology or photoactivation applications^{341,342}. A possible correlation between the shell pigmentation and shell formation is presented in this study. It would be interesting to conduct an in-depth study at the biomolecular level to better understand this relationship. In addition, the investigation of oyster's respiration would constitute an important advance.

III. FURTHER INVESTIGATION OF SHELL PURPLE PATTERNS OF *Crassostrea gigas:* BESIDE PORPHYRINS, OMMOCHROMES?



The identification of carboxylic-rich porphyrins in the shell pigmentation of *C. gigas*, considered as side-products of the haem pathway in animal biology, constitute a preliminary evidence of the haem biosynthetic route in *C. gigas*. However, the presence of other compounds was evidenced by the RPLC-DAD-HRMS analysis of ASM^{POS}. As stated in Chapter II, many compounds generally known in Life for colour and pigmentation could be proposed.

In this chapter, we present the identification of xanthurenic acid (4,8-dihydroxyquinoline-2-carboxylic acid) and some of its possible derivatives. In invertebrates, xanthurenic acid is described as a key metabolite of the biosynthesis of a group of pigments deriving from the metabolism of tryptophan and are named ommochromes. Suspecting their presence in ASM^{POS}, we undertook a detailed characterisation by mass spectrometry of compounds eluted separately from uroporphyrin in **Fig. 19**. The presence of ommochromes and absence of melanins is discussed on the basis of our experimental data and those available in the literature.

III.1. INTRODUCTION

Natural dyes and pigments are usually represented by few dominant groups achieving numerous vital functions in living systems³⁴³. They include anthocyans, carotenoids, melanins and tetrapyrroles such as porphyrins. The occurrence and importance of the latter, known as "the pigments of life"³⁴⁴, has been discussed in Chapter II. Ommochromes are another relatively unexplored group of pigments. Indeed, a rapid overview of the number of references containing the concept of some well-known natural dyes and pigments in SciFinder (**Fig. 30**) reveals that ommochromes are poorly represented compared to melanins and tetrapyrroles.

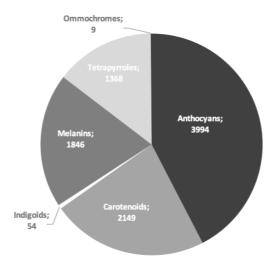


Fig. 30 Overview of the number of references containing the concept of some well-known natural dyes and pigments compared to indigoids and ommochromes (SciFinder, key words: "natural tetrapyrroles", "natural melanins", etc., acceded the 9th September 2020).

Ommochromes are animal pigments that are only observed in invertebrates, forming colours ranging from yellow to orange, red, purple and brown^{345,321,346}. Early studies have proposed a subdivided classification according to their dialysis profile: ommatins (rather dialyzable), ommins (almost non-dialyzable) and ommidins (intermediate)^{345,347}. To date, the structures of approximately fourteen natural ommatins have been described by mass spectrometry (**Table 8**), among which xanthommatin is well established^{348,349} (**Fig. 31a**). Differently, the structures of ommins and ommidins are much less identified so far.

Table 8 Natural ommatins described by mass spectrometry.

Ommatins	Exact mass (Da)	Specimen
Xanthommatin	423.0703	Cuttlefish ³⁵⁰ ,
$C_{20}H_{13}N_3O_8$		Palmfly butterfly ³⁴⁸ , Housefly ³⁴⁹
		Jumbo squid ³⁵¹ , Longfin inshore squid ³⁵²
Decarboxylated xanthommatin	379.0804	Cuttlefish ³⁵⁰ ,
$C_{19}H_{13}N_3O_6$		Palmfly butterfly ³⁴⁸ , Housefly ³⁴⁹
		Longfin inshore squid ³⁵²
Dihydroxanthommatin	425.0859	Cuttlefish ³⁵⁰
$C_{20}H_{15}N_3O_8$		
Decarboxylated dihydroxanthommatin	381.0961	Cuttlefish ³⁵⁰
$C_{19}H_{15}N_3O_6$		
Tinctoriommatin	379.0804	Palmfly butterfly ³⁴⁸
$C_{19}H_{13}N_3O_6$		
iso-tinctoriommatin	379.0804	Palmfly butterfly ³⁴⁸
$C_{19}H_{13}N_3O_6$		
α-hydroxy xanthommatin dimethyl ester	452.0856	Palmfly butterfly ³⁴⁸
$C_{22}H_{16}N_2O_9$		
Oranyeommatin methyl ester	366.0488	Palmfly butterfly ³⁴⁸
$C_{18}H_{10}N_2O_7$		
Elymniommatin	423.0703	Palmfly butterfly ³⁴⁸
$C_{20}H_{13}N_3O_8$		
iso-elymniommatin	423.0703	Palmfly butterfly ³⁴⁸
$C_{20}H_{13}N_3O_8$		
Xanthommatin methyl ester	437.0859	Palmfly butterfly ³⁴⁸
$C_{21}H_{15}N_3O_8$		
α-hydroxy-xanthommatin methyl ester	438.0699	Palmfly butterfly ³⁴⁸
$C_{22}H_{16}N_2O_9$		
β-mercaptoethanol-added xanthommatin	499.0685	Housefly ³⁴⁹
$C_{22}H_{17}N_3O_9S$		
β-mercaptoethanol-added decarboxylated xanthommatin	455.0787	Housefly ³⁴⁹
$C_{21}H_{17}N_3O_7S$		-

Natural xanthommatin and derivatives are extracted with acidified alcohols (MeOH, EtOH + 0.1-5% conc. HCl_(aq)) from invertebrates like squids (**Table 8**)^{348–352}. Without the use of acidifiers, ommatins are insoluble in most aqueous or organic solvents. In solution, compared to porphyrins, they are not photoluminescent but tend to form aggregates³⁴⁷. The structure of xanthommatin is characterised by a phenoxazone unit (**Fig. 31a**) while its reduced form (dihydroxanthommatin, **Fig. 31b**) is characterised by a phenoxazine unit (**Fig. 31b**). Both contain a xanthurenic acid sub-molecular unit (**Fig. 31c**). The diversity of ommatins is generally closely related to their reactivity, which can lead to important structural modifications during extraction and solubilisation.

Fig. 31 Structure of (a) xanthommatin, (b) dihydroxanthommatin and (c) xanthurenic acid.

To date, the reactivity of ommatins is poorly described in the literature to the notable exception of xanthommatin, especially in acid conditions. The aspartic amino acid side chain substituted in position 6 of the aromatic cycle is prone to deamination³⁴⁷. The carboxylic acids in position 22 and 28 are reactive toward alcohols and form esters³⁴⁸. Glycosides and sulfate functions substituted to the oxygen in position 27 of reduced forms are also reported³⁴⁷. Structural modifications catalysed by light irradiation are also known, leading to decarboxylation in position 16, solvent addition on OH functions and reduction of the phenoxazone to form phenoxazine³⁴⁷. The phenoxazone ring opening by hydrolysis of O bonds is induced by light

exposition in aqueous acid medium, and can also lead to reduction of the phenoxazone unit (**Fig. 32**)^{347,353}. Subsequently, the closure of the phenoxazone ring can give new forms of ommatins.

Fig. 32 Phenoxazone ring opening induced by light exposition.

According to B. Linzen (1974), the biosynthesis of ommatins and more generally ommochromes, results from the metabolism of tryptophan³⁴⁵. Two main biological processes have been recently proposed. The first involves the condensation of xanthurenic acid (XA) with 3-hydroxyanthranilic acid (3-HA in **Fig. 33**) and/or 3-hydroxykynurenine (3-HK in **Fig. 33**) by the action of enzymes such as carboxyl methyltransferase³⁴⁸. The second involves only 3-HK as an intermediate precursor by condensation of two units³⁴⁹. In this case, xanthurenic acid is described either as a side product of the intermolecular cyclisation of 3-HK or as a degradation

product of xanthommatin. In a general point of view, depending on the nature of precursors, it suggests that a high variety of chemical function can be substituted in position 1, 2, 3 and 6 of the phenoxazone/phenoxazine skeleton. Thus, a precise identification and structural description is not always possible in natural samples. For example, the red, red-brown and yellow pigments of wings of *Junonia coenia* (common buckeye) were assigned to dihydroxanthommatin, ommatin D and xanthommatin on the basis of UV-vis absorption and thin layer chromatography³⁵⁴, but none were detected by LC-MS-MS/MS³⁵⁵. Only xanthurenic acid was identified among the known precursors and intermediate metabolites.

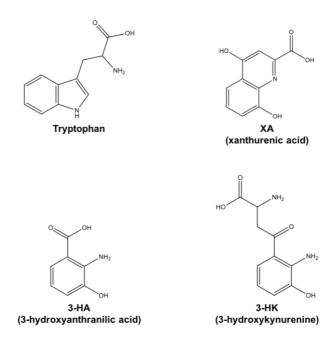


Fig. 33 Main precursors of ommatins.

To finish on this group of pigments, it is important to remind that other classes of ommochromes are reported in the literature: ommins and ommidins. The latter have completely disappeared from experimental investigations subsequent to the work of B. Linzen in 1974^{345,356}. A recent article pointed out their possible occurrence in invertebrates, but no characteristic and unambiguous structures or precise physicochemical properties have been reported to date³⁴⁷.

Ommins are very striking. In 1958, Butenandt *et al.* initially investigated their distribution in the animal kingdom by paper chromatography, degradation in alkali and acids and spectroscopy (UV-vis absorption and IRTF)³⁵⁷. A single structure has been predicated³⁵⁸ solely on the basis of chemical properties³⁴⁵ and elemental determination³⁵⁹, that is nowadays surprisingly well accepted as ommin A (**Fig. 34**)^{360,347}. To date, the structure of the latter was not confirmed by structural investigations. The structure of ommin A derives from three 3-HK sub-molecular units, the sulfur is proposed to arise from cysteine and/or methionine³⁴⁹. While ommatins have an absorption band around 450-500 nm, ommin A absorb around 520 nm³⁴⁷. The biosynthesis of ommins is proposed to arise as a side route of ommatins³⁴⁷. A connection with the biosynthesis of haem is also mentioned.

Fig. 34 Proposed structures of ommin A³⁴⁷.

In bivalves, the occurrence ommochromes in the pigmentation of molluscan shells is not mentioned²⁰. In contrast, ommochromes are proposed as possible pigments contributing to the black colour of molluscs, similar to melanins²¹. The presence of ommochromes, melanins, carotenoids and tetrapyrroles can be hypothesised in the case of *C. gigas* since six genes associated with their biosynthetic pathways were recently identified in the mantle³¹⁰. The occurrence of ommochromes should be considered with the presence of melanins. Indeed, the latter are frequently postulated on the basis of UV-visible absorption without considering ommochromes and effort to differentiate. Some of the physicochemical properties of

ommochrommes are similar to those of melanins, slightly soluble in water, forming aggregates in solution and granules in solid state *in vivo* making their discrimination challenging in a given sample^{345,361}. In animals, the biosynthesis of melanins derives from the metabolism of tyrosine³, different from ommochromes deriving from the metabolism of tryptophan where xanthurenic acid is a specific metabolite. Mainly two classes of melanins are listed in the literature: eumelanin and pheomelanin (**Fig. 35**)³. Neuromelanin is described as a mixture of eumelanin and pheomelanin. Eumelanin is a polycyclic biopolymer of 5,6-dihydroxindole and 5,6-dihydroxyindole-2-carboxylic acid sub-molecular units. Differently, pheomelanin is characterised by the presence of sulfur from benzothiazine and benzothiazole units, formed from cysteinyldopa. The diversity of structures, molecular weights and physicochemical properties of melanins is complex, certainly explaining why no data are available in the literature on their analysis in natural state by RPLC-HRMS.

Fig. 35 Model structures of melanins proposed by Solano (2014)³.

Back to our work, the investigation of the chemical composition of the acid soluble compounds in dissolved POS (ASM^{POS}) conducted by RPLC-DAD-HRMS (ESI+) in the previous chapter (II.2.3.1 Composition profile of ASM^{POS}) has pointed out an entire set of compounds characterised by clusters of di-charged ions. Based on their exact mass (> 1000 Da), these compounds seemed not attributable to any known molluscan shell pigments excepted melanins. Indeed, only eumelanin and pheomelanin can have a molecular weight higher than 1000 Da. Thus, given that both melanins and ommochromes have protonatable/deprotonatable groups, the analysis of ASM^{POS} was also conduct in ESI-, a method of ionisation particularly adapted for deprotonatable compounds. Besides, our attention was caught by the identification of the "unexpected" xanthurenic acid which is linked to the biosynthesis of ommochromes, specially xanthommatin and derivatives. This possible existence of an ommochrome biosynthetic pathway in the oyster C. gigas led us to explore the structural nature of this set of compounds. If converging evidence tends to support this hypothesis, it questions their origin and function in a more general way.

III.2. RESULTS

III.2.1. Characterisation of pigments from shell purple patterns

III.2.1.1. Separation monitored by UV-vis absorption

The ASM^{POS} investigated in Chapter II was first analysed by RPLC with UV-vis detection from 200 to 800 nm in order to define the entire absorption profile of compounds eluted before uroporphyrin (**Fig. 19a**). Indeed, the RPLC method employed in Chapter II allowed to record absorption spectra only until 500 nm whereas the absorption spectrum of ASM^{POS} shows bands beyond 500 nm potentially assignable to multiple pigments in mixture with porphyrins.

The separation of compounds of ASM^{POS} was tested using different methods by varying the water/acetonitrile (+ 0.1% formic acid) gradient system over time and with stationary phases of different polarity. In none of the cases, compounds eluted before uroporphyrin were clearly separated. The best separation was obtained with a water/acetonitrile gradient method of 65 minutes and with a C18 reverse stationary phase (the method is detailed in the experimental part). In these conditions, uroporphyrin is identified at 30.08 min according to its Soret band at 400 nm (**Fig. 36**). The compounds eluted from 10 to 26 min have a broad absorption band from 430 to 600 nm (**Fig. 36**), among which six major signals are identified with λ_{max} ranging from approximately 530 to 486 nm, suggesting a strong contribution to the purple colour of ASM^{POS}. Based on their λ_{max} , the purple colour is apparently composed by violet, pink, red and orange pigments (by order of elution). Their UV-vis absorption profiles significantly differ from those of melanins which are characterised by a continuous decreasing absorption towards the visible region without characteristic bands from 400 to 800 nm³⁶² (**Fig. 37**). They also differ from those of porphyrins reported in the previous chapter, since no Soret band at ~ 400 nm is distinguishable. These profiles are comparable to those of ommochromes reported in **Fig. 38**

where a large band from 400 to 600 nm and another band around 310 or 380 nm are observed depending on the pH and the ommochrome in question.

These data demonstrate that the colour of shell purple patterns of *C. gigas* cannot be solely related to uroporphyrin and derivatives. Moreover, the presence of melanins cannot be excluded since the pigments eluted before uroporphyrin have a relative weak absorbance all along the visible region until 700-750 nm.

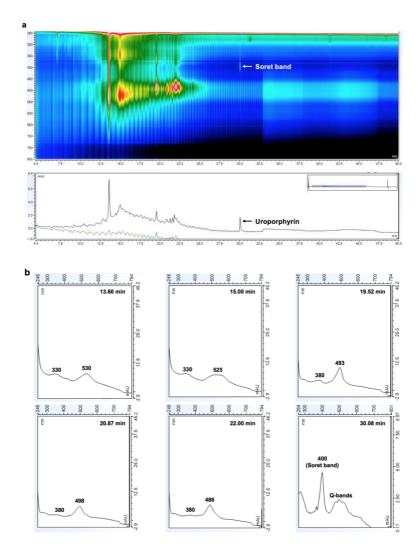


Fig. 36 Reverse phase liquid chromatographic separation of ASM^{POS}. (a) Chromatographic profile with UV-vis detection in 3D field acquisition from 200 to 800 nm with corresponding profile at 405 nm. (b) UV-vis absorption spectra of major pigments.

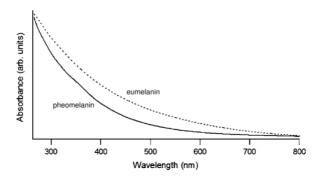


Fig. 37 UV-vis absorption spectra of eumelanin and pheomelanin polymers. Captured from Huijser *et al.* (2011)³⁶².

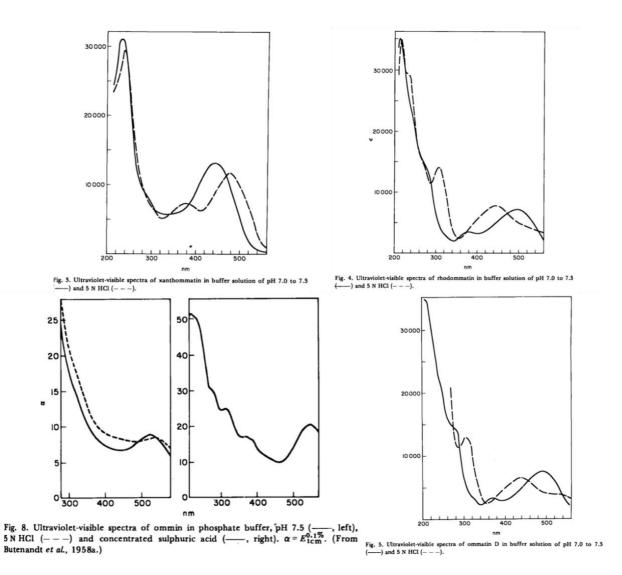


Fig. 38 Absorption spectra of some ommochromes. Captured from B. Linzen 1974³⁴⁵.

III.2.1.2. Determination of the exact mass of pigments

The ASM^{POS} analysed by RPLC-DAD-HRMS (ESI+) in Chapter II was further examined for the determination of the exact mass of the different pigments eluted from 7.5 to 11.5 min (**Fig. 19**). On this period, the corresponding total ion current chromatogram (TIC) obtained by mass spectrometry is noisy and the low intensity of signals does not allow to clearly identify the peaks corresponding to ionised pigments (**Fig. 39a**). A data treatment is proceeded on the TIC chromatogram by applying a digital filter with MassLynx software (version V4.1, Water Corporation). This treatment allows to reduce the noise and to display minor peaks on the basis of the most intense peak at 8.29 min (**Fig. 39b**). The resulting base peak ion chromatogram (BPI) allows to identify five peaks at 8.29, 8.51, 9.30, 9.63 and 10.61 min.

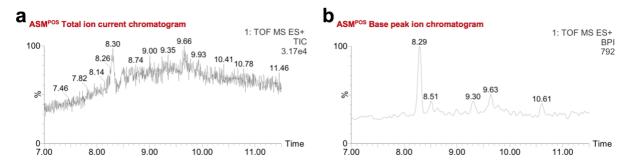


Fig. 39 RPLC-HRMS analysis of ASM^{POS}. (a) Total ion chromatogram (TIC). (b) Base peak ion chromatogram (BPI).

The examination of the mass spectrum of each peak gives access to the exact mass of the molecular ions of pigments. In mass spectrometry, a molecular ion is characterised by its isotopic distribution which is the signature of its isotopic composition. For a molecular ion containing only CHNO isotopes, the intensity of the monoisotopic peak is generally higher than the intensity of p+1 and p+2 peaks as shown with the example of uroporphyrin in **Fig. 21d**. In the particular cases of system containing abundant isotopes such as ³⁷Cl, ⁵⁶Fe, ⁸¹Br, ³⁴S, ⁶⁵Cu, the intensity of the p+2 is generally superior to the p+1. In addition, for a monocharged

molecular ion, the difference of mass between the monoisotopic peak and p+2 is lower than the mass corresponding to 2H (2.0156 Da) that is observed for monocharged molecular ions containing only CHNO isotopes (for example: 56 Fe- 54 Fe = 1.9953 Da, 37 Cl- 35 Cl = 1.9970 Da, 26 Mg- 24 Mg = 1.9975, 65 Cu- 63 Cu = 1.9982 Da, 30 Si- 28 Si = 1.9968 Da, 34 S- 32 S = 1.9958 Da, 41 K- 39 K = 1.9982 Da).

For the peak at 8.29 min, the mass spectrum is characterised by a series of five clusters of ions in the 700-800 m/z range, indicating at least five possible molecular ions for a given peak (**Fig. 40**). The major ions of each cluster are identified at m/z 701.1173 (cluster 1), 723.6810 (cluster 2), 739.6743 (cluster 3) and 763.6566 (cluster 4). The difference of $m/z \sim 0.5$ observed between each peak indicates that ions are di-charged (state of charge z = 2). Clusters of di-charged ions are also observed at 8.51 min (**Fig. 42**), 9.30, 9.63 and 10.61 min (**Table 9**). In few cases, ions with a z = 3 are observed (**Table 9**). Almost all clusters identified at 8.29 are also observed up to 10 min. The relative intensity of ions in clusters 2 and 3 suggests the presence of an abundant isotope or the presence of two different molecular ions.

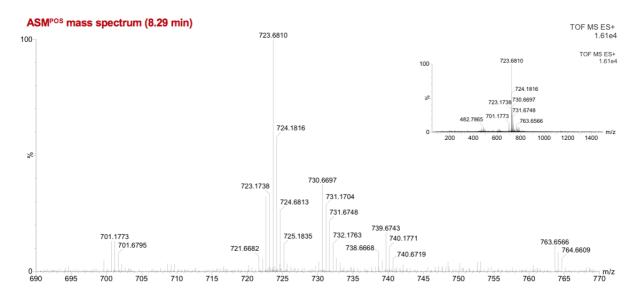


Fig. 40 Mass spectrum obtained at 8.29 min.

porphyrins, ommochromes?

For a given cluster, by applying the **Eq. 3** to each ion and its p+2 peak, it is possible to describe

the presence of an abundant isotope or the presence of two different molecular ions within the

same cluster. In the example of the cluster 2 at 8.29 min, the exact mass of ions at m/z 721.6688,

722.6702, 723.6810 and 724.6813 in **Fig. 41a**, are respectively 1441.3220, 1443.3248,

1445.3464 and 1447.3470 Da. Assuming that the monoisotopic ion is at m/z, 721.6688 and the

corresponding p+2 at m/z, 722.6702, the difference of mass is 2.0028 Da (1443.3248-

1441.3220). If another monoisotopic ion is at m/z 722.6702 and p+2 at 723.6810, the difference

of mass is 2.0216 Da. Similarly, if another monoisotopic ion is at m/z 723.6810 and p+2 at

724.6813, the difference of mass is 2.0006 Da. Given the accuracy of the spectrometer (\pm

0.0030 Da), the difference of mass between 721.6688 and 722.6702 does not correspond to 2H

(2.0156 Da). It is also the case between 723.6810 and 724.6813. A difference of 2H is only

possible between 722.6702 and 723.6810. Consequently, this cluster of ions can reflect the

presence of: i) multiple molecular ions containing abundant isotopes as those mentioned earlier,

ii) a molecular ion containing an element with at least 3 abundant isotopes such as Mg, Si, Cr,

Fe, Ni, Zn and eventually S and Ca and iii) a molecular ion containing only CHNO and multiple

molecular ions with abundant isotopes. This methodology applied to the four other clusters

leads to the same observations (**Fig. 41b-d**).

Eq. 3

 $[M+nH]^{nz} \rightarrow m/z = [M+nH]/nz \rightarrow M = (m/z \cdot nz) - nH$

M: exact mass (Da)

H: mass of a proton (1.0078 Da)

112

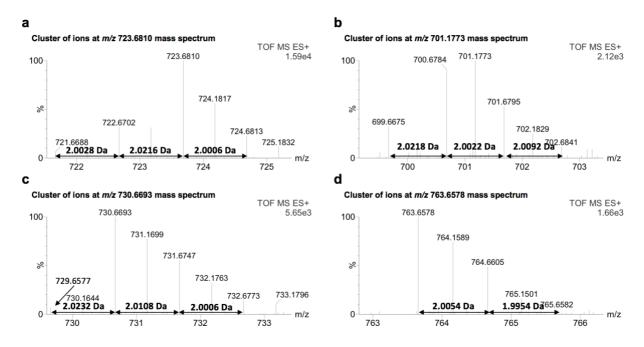


Fig. 41 Isotopic distribution of clusters of ions at 8.29 min. (a-d) clusters of ions at m/z 723.6810, 701.1773, 730.6693 and 763.6578, respectively.

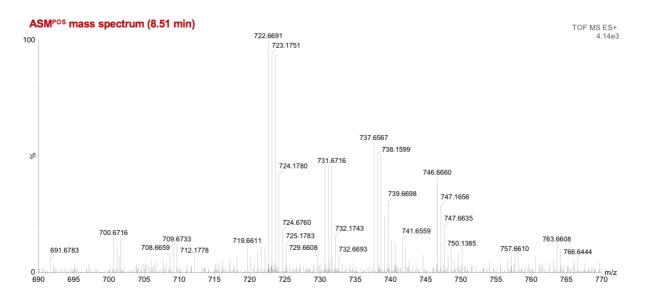


Fig. 42 Mass spectrum obtained at 8.51 min.

Table 9 Multi-charged ions detected in $\ensuremath{\mathrm{ASM^{POS}}}$ by RPLC-HRMS in ESI+.

Retention time (min)	Major ions m/z	State of charge	Exact mass (Da)
8.29	701.1773	2	1400.3390
	468.1248	3	1401.3510
	722.6702	2	1443.3248
	482.7865	3	1445.3361
	723.6810	2	1445.3464
	724.6816	2	1447.3476
	730.6697	2	1459.3238
	739.6743	2	1477.3330
	495.4376	3	1483.2894
	763.6566	2	1525.2976
	782.6364	2	1563.2572
	790.6260	2	1579.2364
8.51	482.1185	2	1443.3321
	722.6691	2	1443.3226
	731.6716	2	1461.3276
	737.6567	2	1473.2978
	746.6660	2	1491.3164
9.30	701.1816	2	1400.3476
	723.1717	2	1444.3278
	722.6732	2	1443.3308
	746.1599	2	1490.3042
9.63	519.6501	2	1038.2924
	722.6757	2	1443.3358
	738.6678	2	1475.3200
	761.2133	2	1520.4110
10.61	722.6698	2	1443.3240

The compilation of mass spectra between 8 and 10 min in **Fig. 43** is a representation of all ions detected in this range of retention time. This representation is important because it allows to provide information on the structural relation between the different ions (**Fig. 43**). For example, the ion at m/z 722.6717 corresponds to the ion at m/z 700.6760 with the addition of CO₂. The ion at m/z 746.6617 corresponds to the ion at m/z 723.6750 with the addition of HCO₂H. The ion at m/z 746.6617 corresponds to the ion at 730.6678 with the addition of O₂. These data show that pigments eluted between 8 and 10 min have a structural proximity with variations corresponding to carboxyl, hydroxyl and sulphate groups. This structural proximity explains partially their poor separation by reverse phase liquid chromatography.

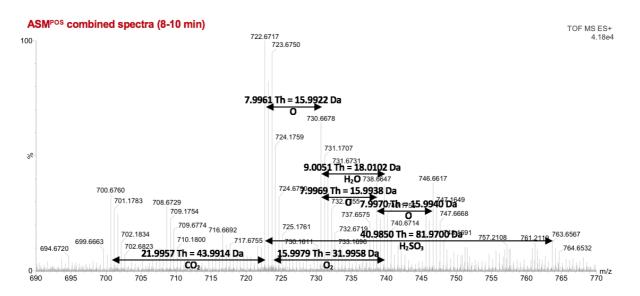


Fig. 43 Combined mass spectra obtained from 8 to 10 min (ESI+).

The analysis of ASM^{POS} was also conducted by RPLC-HRMS in ESI- to confirm the general behaviour and major functions observed in ESI+ as well as the mass of major clusters of ions. The compilation of mass spectra between 8 and 10 min shows a high density di-charged ions in the 600-1000 m/z range (**Fig. 44**). Majors ions are identified at m/z 610.6804, 632.6743, 654.6710, 676.6643, 695.6553, 717.6506, 739.6461 and 755.6404. The difference of mass

between each ion from m/z 610.6804 to 676.6643 correspond to CO₂ groups. Two additional CO₂ groups are identified between ions at m/z 695.6533, 717.6506 and 739.6561. Between m/z 755.6404 and 739.6461, a difference of mass corresponding to O₂ can be also observed. This general behaviour is in agreement with that observed in ESI+. Di-charged ions at m/z > 800 are also observed, suggesting that the mass of pigments can vary from ~ 1000 to at least ~ 2000 Da. At this stage, given the multiple clusters of di-charged ions identified all along the 700-800 m/z range in ESI-, the spectrum is too complex for a fine and precise interpretation.

Given the high molecular weights and the potential presence of elements with abundant isotopes, it is not possible to define a molecular formula for a given ion both in ESI+ and ESI-. Experiments by MS/MS fragmentation of di-charged ions were performed in order to get structural information but mass spectra were not exploitable due to the low intensity of signals of parent ions. We tried to isolate a compound eluted at 13.60 min in **Fig. 36** by semi-preparative chromatography (**Fig. 82** – **experimental part**), but in every case, the RPLC-HRMS analysis revealed a mixture of clusters of di-charged ions. We are presently trying to solve these issues.

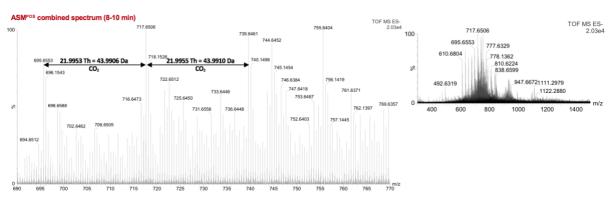


Fig. 44 Combined mass spectra obtained from 8 to 10 min (ESI-).

III.2.2. Screening of metabolic products and identification of xanthurenic acid

Facing the complex dataset obtained by mass spectrometry, we decided to examine signals eluted earlier in the BPI chromatogram of ASM^{POS}. A single signal is observed at 4.44 min, with a [M+H]⁺ at *m/z* 206.0454 (**Fig. 45a-b**), potentially corresponding to a compound with a molecular formula of C₁₀H₇NO₄ and an exact mass of 205.0376 Da (mass accuracy of ± 0.5 ppm). This is in agreement with xanthurenic acid (C₁₀H₇NO₄, 205.0375 Da), but also with a variety of other potential substances (1023 results in SciFinder). At this level, confirmation is possible by comparative analysis with a XA standard. Indeed, solutions of XA standard and ASM^{POS} analysed separately present the same exact mass and their fragmentation pattern by MS/MS are in total agreement (**Fig. 45b-e**). To definitively verify the presence of XA in ASM^{POS}, the diluted solution of XA standard is co-injected with ASM^{POS} (**Fig. 46**). The resulting extracted ion chromatograms show an increase of the XA signal in the sample containing ASM^{POS} + XA standard compared to ASM^{POS} alone.

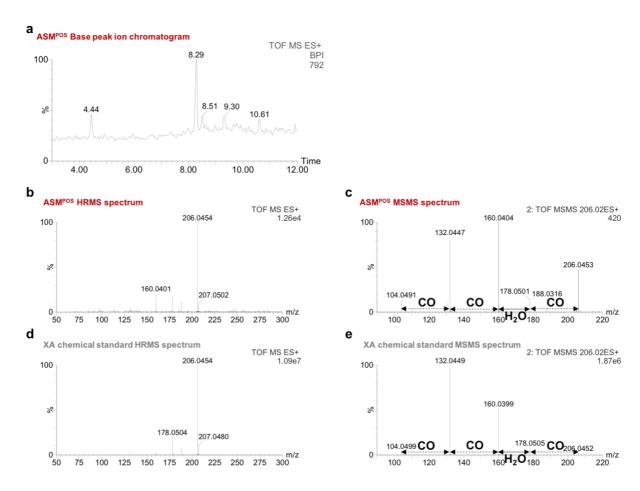


Fig. 45 Identification of xanthurenic acid in ASM^{POS}**.** (**a-b**) Mass spectrum and mass fragmentation spectrum of XA in ASM^{POS}. (**c-d**) Mass spectrum and mass fragmentation spectrum of XA standard.

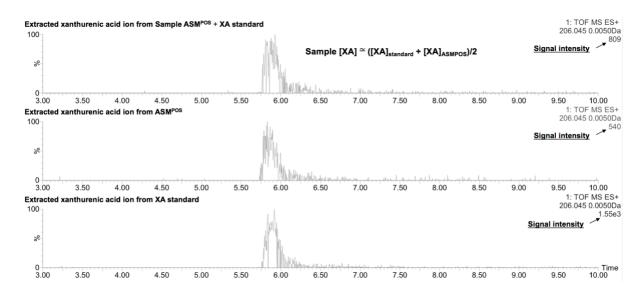


Fig. 46 Co-injection of XA standard and ASM^{POS}**.** Shift of retention time compared to the initial signal at 4.44 min is due to an analysis performed on a fresh ASM^{POS}.

Given the identification of XA in ASM^{POS}, we supposed that known metabolites of the ommochromes and melanins biosynthetic pathways could be identified. Thus, the m/z signals corresponding to the molecular ions of known precursors and side-products of the biosynthesis of ommatins (**Fig. 47**) were searched in the TIC chromatogram of ASM^{POS}, namely formylkynurenine (m/z calculated at 237.0875), kynurenine (m/z calculated at 209.0926), anthranilic acid (m/z calculated at 138.0555), 3-hydroxyanthranilic acid (m/z calculated at 154.0504), kynurenic acid (m/z calculated at 190.0504), 3-hydroxykynurenine (m/z calculated at 225.0875) and tryptophan (m/z calculated at 205.0977). None of these signals were identified.

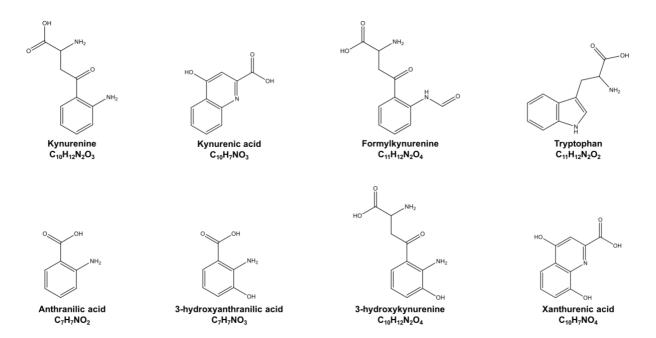


Fig. 47 Structure of known precursors and side-products of ommatins.

In addition, the m/z signals corresponding to the molecular ions of precursors of the melanins listed by Solano (2014) (**Fig. 48**)³ were also searched in the TIC chromatogram of ASM^{POS}. Again, none of these signals were identified. To complete this comparative study on melanins, a commercial sample of *Sepia officinalis* eumelanin was analysed by RPLC-DAD-HRMS (ESI+) according to the same method as ASM^{POS} (**Fig. 85-86** – **experimental part**). The

eumelanin black powder was insoluble in 1M HCl_(aq) and very slightly soluble in 1M NaOH_(aq). The analysis of the solubilised fraction shows a single signal at 9.13 min on the chromatogram obtained by UV-vis detection. The corresponding mass spectrum reveals indole-based ions related to eumelanin polymers constituted by indole carboxylic acid sub-molecular units (**Fig. 35**). The major molecular ions at m/z 118.0657 and 146.0609 corresponding respectively to C₈H₈N⁺ and C₉H₈NO⁺ were not detected in ASM^{POS}. In consequence, these results question the presence of eumelanin in ASM^{POS}.

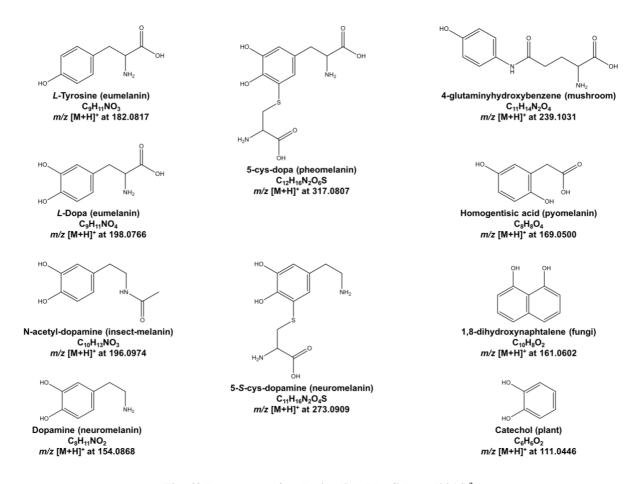


Fig. 48 Precursors of melanins listed by Solano (2014)³.

III.2.3. Preparation of a sample concentrated in pigments

The results reported above were obtained on ASMPOS, that is to say a sample with a CaCl₂ concentration around 55 g/L. As mentioned in the RPLC-DAD-HRMS analysis of ASM^{POS}, MS/MS experiments require to increase the signal corresponding to pigments. To achieved the preparation of a sample more concentrated in pigments than ASMPOS, removing the calcium salts through decalcification is necessary. The decalcification method employed in Chapter II by precipitation of CaF₂ with the addition of HF_(aq) is efficient since it allows to prepare a sample concentrated in organic species without the formation of calcium salts. However, this method does not allow to separate the different groups of pigments in ASM^{POS}. Therefore, decalcification was conducted using C18 grafted silica gel with a water/acetonitrile acidified gradient system by replication, on open column, of the RPLC separation. In addition to remove the calcium salt, this method allows the separation of fluorescent porphyrins from the nonfluorescent pigments eluted earlier (the details of this method are given in Chapter IV). This method first lead to the elution of calcium-salts (decalcification), then a purple fraction (PF), potentially concentrated in pigments, is separated from a yellow fraction (YF) potentially concentrated in porphyrins since this fraction emits a pink-red photoluminescence under λ_{ex} ~ 400. After freeze-drying and solubilisation in 1M HCl_(aq), the PF is not photoluminescent under UV excitation and its UV-vis absorption spectrum is similar to that of the initial ASM^{POS} (λ_{max} ~ 464, 596 and 552 nm, **Fig. 49**).

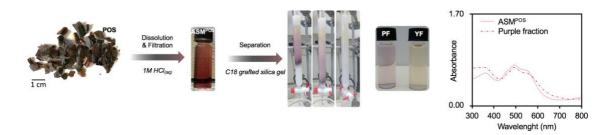


Fig. 49 Separation of ASM^{POS} on C18 grafted silica gel.

The PF is soluble in acid and alkali conditions. It differs from melanins, at least from eumelanin tested in the previous section, only slightly soluble in alkali, pheomelanin being described as slightly soluble in alkali and acid³²¹. These are additional results which hardly questions the presence of melanins, especially eumelanin.

Besides, PF is slightly soluble at 1 mg/mL in MeOH, but turns fully soluble in MeOH containing 0.1 or 1% of concentrated HCl_(aq). A typical property of ommochromes, different from melanins that are not soluble in organic solvent with or without acid³²¹.

Elemental determination by EDX analysis shows significant content of carbon, nitrogen and oxygen are observed, revealing the organic nature of PF (**Table 10**, the elemental composition is detailed in Chapter IV). The identification of nitrogen is in line with N-containing pigments such as melanins, tetrapyrroles, indigoids and ommochromes, but also with amino acids that could be associated with them. Besides, according to data obtained by mass spectrometry describing the presence of abundant isotopes, the identification of Mg, Si, S, Cl, K, Ca and Fe suggests their association with the pigments of PF. Analysis by X-ray photoelectron spectroscopy (XPS), presently in progress, will provides additional information on the chemical state for some of them. In addition, NMR spectra obtained from PF show the presence of carbonyl, aromatic and aliphatic groups but do not allow to assign a known group of N-containing pigments (**Fig. 87-91** – **experimental part**).

Table 10. Elemental composition of PF by EDX analysis.

Elements	at.% (triplicate)
Carbon	32.95 ± 2.21
Nitrogen	2.45 ± 0.56
Oxygen	14.65 ± 2.63
Magnesium	0.19 ± 0.02
Aluminium	0.26 ± 0.04
Silicon	0.26 ± 0.08
Phosphorus	0.48 ± 0.16
Sulfur	0.38 ± 0.14
Chloride	3.86 ± 1.18
Potassium	0.35 ± 1.18
Calcium	1.84 ± 0.32
Iron	0.50 ± 0.27
Lead	0.33*

^{*:} detected once.

The chromatographic profile of PF obtained at 405 nm compared to ASM^{POS} reveals a high density of absorbing species from 5 to 13 min (**Fig. 50a-b**). Xanthurenic acid is detected similarly to ASM^{POS}. Besides, the signal of uroporphyrin at 13.35 min in ASM^{POS} is not observed in PF, indicating that uroporphyrin and derivatives were fully separated, this is also confirmed by their absence when searching their corresponding m/z signal in the chromatogram obtained by mass spectrometry. The poor separation between 5 and 13 min is not a limit for MS/MS experiments, since the ions of interest can be specifically selected by the quadrupole of the mass spectrometer with a resolution of 2-3 m/z.

Compared to the analysis of ASM^{POS} in ESI+, the clusters of di-charged ions previously described are now eluted between 6.42 to 10.71 min instead of 8.29 to 10.61 min. This is the case for the ion at m/z 722.6700 identified in PF with a high ionic intensity from 7.5 to 8.5 min. (**Fig. 50c**). The decalcification/concentration also allows to observe monocharged and dicharged ions not detected in ASM^{POS}. For instance, a monocharged ion at m/z 457.0883, not detected in ASM^{POS}, is observed at three retention time (6.06, 6.84 and 8.89 min, **Fig. 50d**). The corresponding exact mass of 456.0805 Da is particularly interesting. Among the set of ommatins described by mass spectrometry (**Table 8**), it may correspond to the exact mass of a

 α -hydroxy-xanthommatin methyl ester derivative (438.0699 Da, $C_{21}H_{14}N_2O_9$, **Fig. 51**) with the addition of a water molecule ($C_{21}H_{16}N_2O_{10}$: 456.0805 Da). However, it may also correspond to a variety of compounds other than ommatins. Thus, the structure of this compound, named **compound #1**, is detailed in the next section.

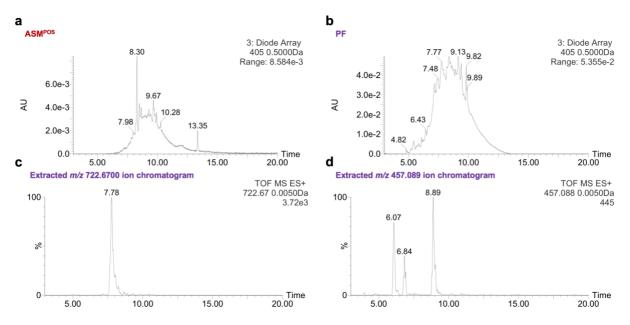


Fig. 50 Comparison of the chromatographic profiles of ASM^{POS} **and PF at 405 nm. (a)** Profile of ASM^{POS} at 405 nm. (b) Profile of PF at 405 nm. (c-d) Examples of extracted ions chromatograms.

Fig. 51 α-hydroxy-xanthommatin methyl ester

III.2.4. Structural investigation

III.2.4.1. Mass fragmentation of compound #1

As mentioned above, the **compound #1** with an exact mass of 456.0805 Da, can be potentially related to a xanthommatin derivative. In order to confirm or reject this hypothesis, MS/MS fragmentation was performed in both ESI+ and ESI- to define a fragmentation pattern and a molecular formula.

Starting from the fragmentation spectrum obtained in ESI-, an intense mono-charged product ion is observed at m/z 160.0396 (**Fig. 52**). The latter can be attributed to decarboxylated XA-(C₉H₆NO₂-). This is first supported by the fragmentation spectrum of xanthurenic acid reported in the mzCloudTM database in ESI- mode that shows an intense product ion at m/z 160.0404, and secondly, by the identification of this product ion by MS/MS fragmentation of the XA standard in ESI- (**Fig. 53**).

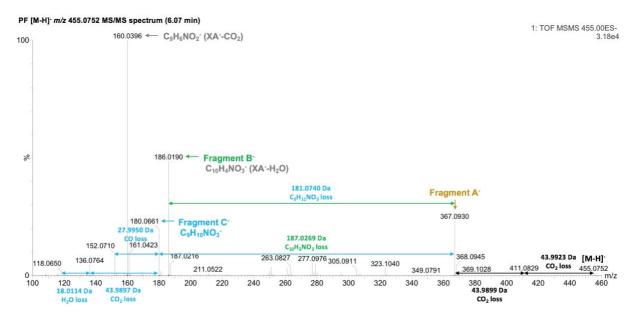


Fig. 52 MS/MS spectrum of compound #1 obtained in ESI-.

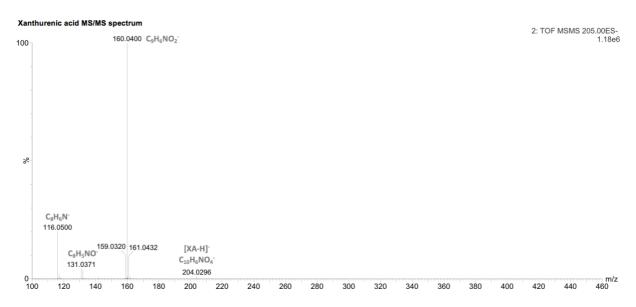


Fig. 53 MS/MS spectrum of the xanthurenic acid standard obtained in ESI-.

The product ion at m/z 186.0190 (**Fragment B**² in **Fig. 52**) is in agreement with a dehydrated XA² (**C**₁₀**H**₄**NO**₃). The **Fragment A**² is formed after the neutral loss of 2CO₂ from the molecular ion [**M**-**H**]² at m/z 455.0752, certainly corresponding to two carboxyl groups³²⁷. The neutral loss of 181.0740 Da between **Fragment A**² and **Fragment B**³ gives the ion at m/z 180.0661, named **Fragment C**³. The product ions at m/z 152.0710, 136.0764 and 118.0650 correspond respectively to neutral loss of CO, CO₂ and H₂O from **Fragment C**³. According to this general fragmentation pattern, a single molecular formula is possible for **compound #1**: C₂₁H₁₆N₂O₁₀ with a calculated exact mass of 456.0805 Da which is in total agreement with the exact mass of **compound #1** (456.0805 Da). According to this molecular formula, the degree of unsaturation (DBE) is 15 and the formula of **Fragment C**³ is **C**₂H₁₀NO₃³. At this stage, we can reasonably assume that **compound #1** is made of two sub-structural units which include a dehydrated XA unit and two additional carboxyl groups. However, a definitive and precise structure is not possible since the position of the two carboxyl groups as well as the structure of **Fragment C**³ are not precisely defined. Thus, a relation with a xanthommatin derivative cannot be proved.

The fragmentation of **compound #1** in ESI+ gives reliable information on the XA sub-structural unit (**Fig. 54**). Indeed, the product ions at m/z 186.0189 and 204.0290 correspond to XA+-2H-H₂O and XA+-2H, respectively. The ion at m/z 232.0255, XA+-2H+CO indicates the presence of a carbonyl group substituted to XA+-2H. This carbonyl group can be the result of a dehydrated carboxyl or a reorganisation of the XA unit subsequent to fragmentation. It suggests the presence of a XA-like unit, thus one of the carboxyl groups detected in ESI- certainly corresponds to the carboxyl group of a XA unit. In addition, the neutral loss of 179.0552 Da, corresponding to C₉H₉NO₃ is also observed. These data confirm that **compound #1** is made of two sub-structural units including a xanthurenic acid-like. The precise structure of the other sub-molecular unit cannot be proposed at this stage. The isolation of this compound as well as NMR and multistage mass spectrometry experiments are presently in progress to define a more precise structure.

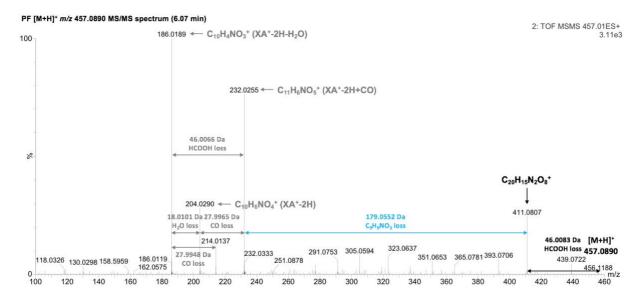


Fig. 54 MS/MS spectrum of compound #1 (C₂₁H₁₆N₂O₁₀) obtained in ESI+.

III.2.4.2. Mass fragmentation of other monocharged ions

MS/MS experiments were conducted in automatic mode (ESI+ and ESI-) in order to search for other compounds in PF related to the structure of **compound #1**. Briefly, along the RPLC-HRMS run, signals of monocharged molecular ions exhibiting a sufficient intensity were automatically fragmented by the mass spectrometer quadrupole. The resulting fragmentation spectra were examined by comparison with the spectrum of **compound #1**.

In ESI-, only few exploitable MS/MS spectra were obtained. However, a compound eluted at 4.70 min (compound #2, [M-H] m/z at 268.0461, Fig. 55) is of particular interest for the description of the general skeleton of **compound #1**. Indeed, in the fragmentation spectrum of compound #2 (Fig. 55) we can observe a product ion at m/z 180.0656 (C₉H₁₀NO₃), corresponding to Fragment C observed in the fragmentation spectrum of compound #1. Besides, fragmentation of **compound #2** also lead to a product ion at m/z 108.0445 resulting from the neutral loss of C₂H₄CO₂ from Fragment C. This product ion is in agreement with an aminophenol ion according to mzCloudTM. Indeed, compounds with a product ion at m/z108.0445 were searched in the ESI- database, among which 3-aminosalicylic acid and 3hydroxyanthranilic acid caught our attention (Fig. 56) since the former is proposed as an intermediate precursor of ommatins in the literature³⁴⁸. This product ion is also observable in the fragmentation spectrum of hydroxykynurenine, another precursor of ommatins. However, we cannot define the precise position of -OH, -NH₂ and -C₂H₄CO₂H substituted on the aromatic cycle. Besides, it is not excluded that Fragment C may be of different structural natural. Another point to mention is that the molecular ion of **compound #2** is accompanied, in the mass spectrum, by a $[M-H]^-$ at m/z 654.1232 (exact mass 655.1310 Da Fig. 55). It may indicate that **compound #2** is actually a fragment of the compound with an exact mass of 655.1310 Da formed during its ionisation.

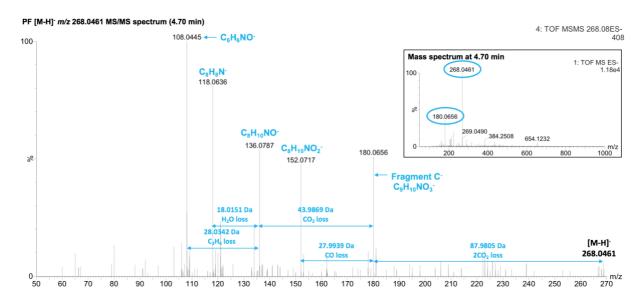


Fig. 55 MS/MS spectrum of compound #2 obtained in ESI- with the corresponding mass spectrum.

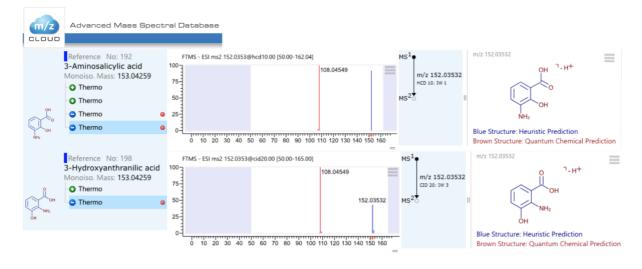


Fig. 56 MS/MS (ESI-) spectra of 3-aminosalicylic acid and 3-hydroxyanthranilic acid, captured from the mzCloudTM database.

According to the MS/MS fragmentation of **compound #2**, a schematic structure of **compound** #1 can be drafted (**Fig. 57**). As observed in its fragmentation spectrum in ESI-, two carboxyl groups were identified but cannot be positioned on one of the sub-molecular unit. In addition, the bond(s) between the two units cannot be defined at this stage. An amide function is possible. Given the DBE of **compound #1**, a xanthommatin derivative-like structure is possible, especially an uncyclised form as those mentioned in the introduction (**Fig. 32**). Once isolated, XPS experiments will provides additional information on the chemical state of nitrogen.

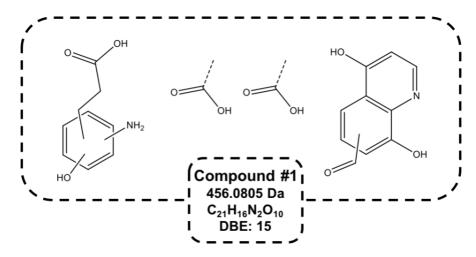


Fig. 57 Drafted schematic structure of compound #1.

Beside the MS/MS experiment in ESI- described above, the automatic MS/MS experiment performed in ESI+ has led to identify 8 ions at m/z 250.0354 (249.0273 Da), 232.0323 (232.0168 Da), 425.0644 (424.0543 Da), 443.0715 (442.0648 Da), 638.1235 (637.1180 Da), 656.1369 (655.1286 Da), 672.1334 (671.1235 Da) and 680.1383 (679.1286) with product ions common to **compound #1**.

The fragmentation spectrum of the ion at m/z 250.0354 (**compound #3** in **Table 11**) shows product ions at m/z 186.0189, 204.0290, 232.0255 corresponding to XA⁺-2H-H₂O, XA⁺-2H, XA⁺-2H+CO (**Fig. 58**), previously identified in the fragmentation of **compound #1**. **Compound #3** is certainly a carboxylated XA (**Fig. 59**). This compound was detected in the same range of retention time as di-charged ions, it may indicate that this compound is actually a labile fragment formed during ionisation.

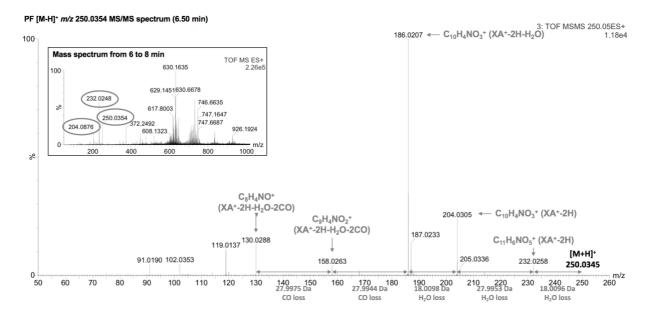


Fig. 58 MS/MS spectrum of compound #3 obtained in ESI+ with the corresponding mass spectrum.

Fig. 59 Drafted structure of compound #3.

The ion at m/z 232.0323 (**compound #4** in **Table 11**), was previously observed in the fragmentation spectrum of **compound #1** and **#3**. This compound is also observed in the same retention range as di-charged ion, suggesting a possible in-source fragment.

The fragmentation of ions at m/z 425.0644 and 443.0715 (**compound #5** and **#6** in **Table 11**), shows the product ions assigned to the XA sub-molecular unit, suggesting structures proximal to **compound #1**.

The fragmentation of the ion at m/z 638.1235 (**compound** #7 in **Table 11**) is particularly interesting. Indeed, a product ion is identified at m/z 457.0918, corresponding to the molecular ion of **compound** #1 in ESI+. It potentially shows that **compound** #1 is a fragment of a higher compound. Accordingly, 3 molecular formula are possible for **compound** #7 with a CHNOS composition: C₂₉H₂₃N₃O₁₄, C₂₄H₂₃N₅O₁₆ and C₂₆H₂₇N₃O₁₄S, among which the mass accuracy for C₂₉H₂₃N₃O₁₄ is ± 0.0 ppm. It strongly suggests that the molecular formula of **compound** #7 is C₂₉H₂₃N₃O₁₄ with a DBE of 20. **Compound** #8 corresponds to **compound** #7+H₂O. **Compound** #9 correspond to **compound** #8+O and **compound** #10 corresponds to **compound** #7+HCOOH. This structural relation is in agreement with the general structural relation of clusters of di-charged ions observed in ASM^{POS}. In addition, product ions at m/z 186.0189, 204.0290, 232.0255 are quasi-systematically identified in **Table 11**, supporting a common XA sub-molecular unit in their structure.

Table 11 Tandem mass fragmentation data of compounds with a structure similar to $C_{21}H_{16}N_2O_{10}$ (Fig. 83 – experimental part).

Compounds	Monocharged ions	RT	Monocharged MS/MS fragments
#1	(<i>m/z</i> , exact mass, formula) [M+H] ⁺ : 457.0895	(min) 6.08, 6.85, 8.93	(<i>m</i> / <i>z</i>) 411.0807
#1		0.08, 0.83, 8.93	
	456.0805 Da		393.0706 365.0781
	$C_{21}H_{16}N_2O_{10}$		365.0781 351.0652
	DBE: 15		351.0653
			323.0637
			305.0594
			291.0753
			232.0255
			204.0290
			186.0189
#3	[M+H]+: 250.0354	6.5 to 8.0	232.0258 (-H ₂ O)
	249.0273 Da		204.0290 (-HCO ₂ H)
	$C_{11}H_7NO_6$		186.0207 (-HCO ₂ H, -H ₂ O)
	DBE: 9		158.0263 (-2HCO ₂ H)
	DBE. 9		
			130.0288 (-2HCO ₂ H, -CO)
			119.0137 (-2HCO ₂ H, -2CO)
#4	[M+H] ⁺ : 232.0323	6.0 to 11.0	204.0305
	231.0168 Da		186.0207
	$C_{11}H_5NO_5$		160.0377
	DBE: 10		130.0288
			119.0137
			91.0190
#5	[M+H]+: 425.0644	6.40, 6.89	186.0177
	424.0543 Da		
	$C_{20}H_{12}N_2O_9$		
	DBE: 16		250.0540
#6	[M+H] ⁺ : 443.0715	6.37, 6.99	379.0560
	442.0648 Da		351.0621
	$C_{20}H_{14}N_2O_{10}$		335.0659
	DBE: 15		333.0532
			321.0497
			307.0763
			305.0580
			293.0547
			290.0477
			279.0759
			265.0580
			262.0500
			247.0517
			237.0684
			236.0703
			222.0576
			219.0594
			204.0305
#7	[M+H] ⁺ : 638.1235	4.73, 5.05, 6.45, 6.63	186.0207 620.1124
# /	637.1180 Da	4.73, 3.03, 0.43, 0.03	576.1246
	$C_{29}H_{23}N_3O_{14} (\pm 0.0 \text{ ppm})$		530.1188
	DBE: 20		514.0886
			512.1057
	Or:		488.1056
	$C_{24}H_{23}N_5O_{16} (+ 4.0 \text{ ppm})$		486.1329
	$C_{26}H_{27}N_3O_{14}S$ (- 3.4 ppm)		482.1044
	- 2327- ·3 - 14- (2 pp.m)		470.1049
			457.0918
			452.0930
			442.1090
			424.0920
			411.0785
			410.0768
			394.0864
			365.0772
			352.0699

Chapter III. Further investigation of shell purple patterns of Crassostrea gigas: beside porphyrins, ommochromes?

			301.0643	
			261.0677	
			233.0720	
			160.0370	
			150.0223	
#8	[M+H]+: 656.1369	5.03	365.0772	
	655.1286 Da		319.0718	
	$C_{29}H_{25}N_3O_{15} (\pm 0.0 \text{ ppm})$		301.0643	
	DBE: 19		275.0826	
			261.0642	
	Or:		247.0895	
	$C_{33}H_{25}N_3O_{10}S (+ 2.5 ppm)$		233.0753	
	$C_{24}H_{25}N_5O_{17} (+ 4.1 \text{ ppm})$			
#9	[M+H]+: 672.1334	5.07	232.0258	_
	671.1235 Da		214.0149	
	$C_{29}H_{25}N_3O_{16} (\pm 0.0 \text{ ppm})$		204.0305	
	DBE: 19		186.0207	
			168.0659	
	Or:		158.0235	
	$C_{33}H_{25}N_3O_{11}S$ (+ 3.7 ppm)		150.0169	
	$C_{24}H_{25}N_5O_{18} (+ 4.0 \text{ ppm})$		130.0313	
			119.0113	
#10	[M+H]+: 680.1383	7.67, 8.03, 9.54	232.0258	
	679.1286 Da		204.0305	
	$C_{31}H_{25}N_3O_{15} (\pm 0.0 \text{ ppm})$		186.0177	
	DBE: 21		180.0674	
			130.0288	
	Or:			
	$C_{35}H_{25}N_3O_{10}S (+ 3.7 ppm)$			
	$C_{26}H_{25}N_5O_{17}$ (+ 4.9 ppm)			

Supplemental monocharged ions were detected but not fragmented due to the low intensity of their signal (**Table 12**). However, their molecular formula can be potentially proposed by correlation with ions fragmented in **Table 11**. All together, these results show the structural proximity of monocharged ions in PF and ASM^{POS}.

Table 12 Compounds with structure potentially related to compound #1 $C_{21}H_{16}N_2O_{10}$.

Compounds	Monocharged ions (m/z)	RT (min)	Molecular ions (based on compound #1)	Molecular formula, exact mass	DBE
11	407.0561	6.4	[compound #1-HCO ₂ H-2H ₂] ⁺	$C_{20}H_{10}N_2O_8$ 406.0437 Da	17
12	411.0818	5.03, 6.10	[compound #1-HCO ₂ H-H ₂] ⁺	C ₂₀ H ₁₄ N ₂ O ₈ 410.0750 Da	15
13	415.1185	7.40	[compound #1-CO ₂ +H ₂] ⁺	C ₂₀ H ₁₈ N ₂ O ₈ 414.1063 Da	13
14	417.0929	4.00, 4.29	[compound #1-C ₂ O] ⁺	C ₁₉ H ₁₆ N ₂ O ₉ 416.0856 Da	13
15	429.0920	5.06, 7.48	[compound #1-CO] ⁺	C ₂₀ H ₁₆ N ₂ O ₉ 428.0856 Da	14
16	439.0794	6.06, 6.81	[compound #1-H ₂ O] ⁺	C ₂₁ H ₁₄ N ₂ O ₉ 438.0699 Da	16
17	445.0882	5.11	[compound #1-C] ⁺	C ₂₀ H ₁₆ N ₂ O ₁₀ 444.0805 Da	14
18	459.1028	6.31	[compound #1+H ₂] ⁺	C ₂₁ H ₁₈ N ₂ O ₁₀ 458.0916 Da	14
19	461.0815	5.35	[compound #1-C+O] ⁺	C ₂₀ H ₁₆ N ₂ O ₁₁ 460.0754 Da	14
20	473.0836	5.94, 6.45, 8.82	[compound #1+O] ⁺	$C_{21}H_{16}N_2O_{11}$ 472.0745 Da	15
21	481.1118	5.09	[compound #1-C+H ₂ O+H ₂] ⁺	$C_{20}H_{20}N_2O_{12}$ 480.1016 Da	12

III.2.4.3. Mass fragmentation of major di-charged ions

During the analysis of ASM^{POS} by RPLC-HRMS, we identified a high number of clusters of di-charged ions in the 700-800 m/z range, both in ESI+ and ESI- mode. In ESI+, the ion at m/z 722.6717 was detected all along the retention time of pigments but its ionic intensity was not sufficient to get reliable information on its structure by MS/MS fragmentation. In PF, its fragmentation is possible due to a sufficient ionic intensity at 7.78 min (**Fig. 60a**). For this parent ion detected at m/z 722.6733 at least six successive neutral loss of CO₂ are observed until the product ion at m/z 581.6984 (**Fig. 60b**). Between product ions at m/z 581.6984 and 299.1008, signal intensity is too low to attribute mass losses. Between m/z 172.0361 and 299.1008 a neutral loss of 125.0474 Da can be potentially assigned to C₆H₇NO₂. As well the ion at m/z 174.0534 may be potentially assigned to C₁₀H₈NO₂. However, on the basis of this fragmentation pattern alone, the number of possible molecular formula for this di-charged ion is too high for a reasonable proposition (> 1000), especially with the possible presence of abundant elements as observed by EDX analysis. We are presently trying to solve this issue by considering another method like multistage mass spectrometry.

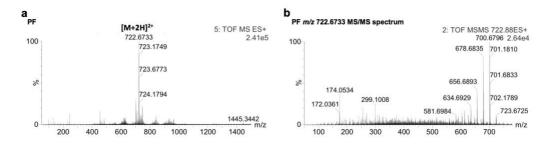


Fig. 60 MS/MS of the ion at m/z 722.6733 in ESI+. (a) Mass spectrum at 7.78 min. (b) MS/MS spectrum.

Another di-charged ion at m/z 763.6578 previously identified in ASM^{POS} was investigated by MS/MS fragmentation (**Fig. 61**). Three intense product ions at m/z 130.0294, 186.0199, 204.0280 and 232.0235 were observed in the fragmentation spectrum. All of them were

previously observed in the fragmentation of the monocharged ions and are related to the fragmentation of the XA-like sub-molecular unit. MS/MS (ESI+) experiments at variable collision energy are presently in progress to observe product ions at m/z > 232.

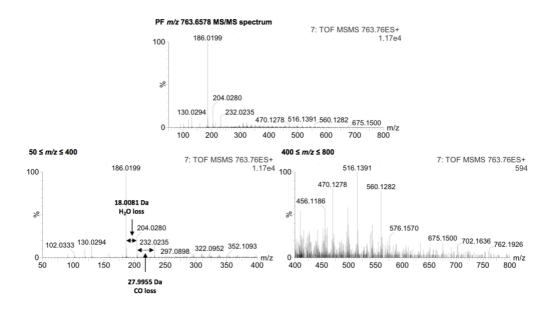


Fig. 61 MS/MS of the ion at m/z 763.6578 in ESI+.

To complete our study on di-charged ions, we are presently conducting MS/MS fragmentation experiments on PF in ESI-. To date, five di-charged ions at m/z 722.6521 (1447.3198 Da), 730.6509 (1463.3174 Da), 744.6485 (1491.3126 Da), 752.6451 (1507.3058 Da) and 763.6391 (1529.2938 Da) were investigated. Their MS/MS spectra are complex due to numerous product ions at m/z > 500 (**Fig. 62**). Multiple neutral loss of CO₂ can be distinguished, at least nine for the 722 cluster (**Fig. 62a**), six for the 730 cluster (**Fig. 62b**), eight for the 744 cluster (**Fig. 62c**), seven for the 752 cluster (**Fig. 62d**) and four for the 763 cluster (**Fig. 62e**). In each case, an intense mono-charged product ion is observed at m/z 160.0397 \pm 0.0001 corresponding to decarboxylated XA⁻ previously observed in the fragmentation of **compound #1**. It supports a common XA-like sub-structural unit between these compound.

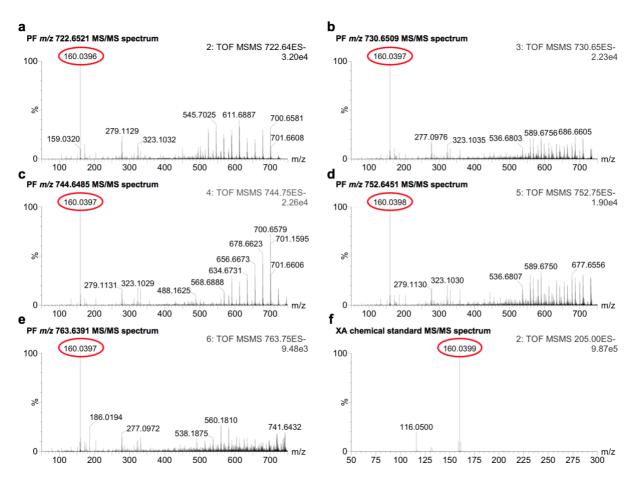


Fig. 62 MS/MS of di-charged ions in ESI-. (a-e) MS/MS spectra of clusters of ions at m/z 722.6521, 730.6509, 744.6485, 752.6451 and 763.6391, respectively. (f) MS/MS spectrum of the xanthurenic acid standard.

III.3. DISCUSSION

In this study, an entire family of pigments composed of a common sub-molecular xanthurenic acid-like unit, possibly decarboxylated, was identified. Besides, the identification of XA as a separated compound by reverse phase liquid chromatographic suggests a cross-related origin. In invertebrates, this compound is described as a metabolite exclusively related to the biosynthesis of ommochromes ^{321,345,349}, all deriving from the metabolism of tryptophan. Other metabolites are also well-known, but only XA was identified in our study. It suggests that XA is either a metabolite produced in excess or a degradation product of multiple possible origin (of pigments during extraction, during biosynthesis, during the life evolution of the shell, ...). The latter is compatible with the recent investigations and descriptions of the biosynthesis of ommochromes, more specifically ommatins where XA is proposed as a side product of the intramolecular cyclisation of 3-HK and/or as a physicochemical or physiological degradation product of xanthommatin and derivatives ^{347,349}. A similar process could occur in our study, the observed XA can actually derive from the degradation of XA-like-containing pigments.

These pigments have comparable properties to those described for ommatins and ommins mentioned in the introduction. Indeed, their solubility in organic solvents is made possible by the addition of acids. In solution, they are not photoluminescent and prone to adsorption on cellulosic dialysis membrane (**Fig. 92** – **experimental part**). In addition, their UV-vis absorption profile are comparable to those of ommochromes where a large band from 400 to 600 nm and another band around 310 or 380 nm are observed depending on the pH and the ommochrome in question.

The structures of ommochromes described in the literature by mass spectrometry are scarce, reported for only few of ommatins (Table 8). Their fragmentation patterns differ from the observed fragmentation of the pigments reported here. Such difference can be attributed to different reasons, first the different intermediate precursors can lead to structural differences as observed by Panettieri et al. (2018) with XA, 3-HK and 3HA as precursors. Secondly, MS/MS fragmentation in ESI+ reported in the literature does not allow to produce a XA-like fragment as the one observed in this study^{348,349}. These MS/MS experiments were conducted on phenoxazone-base ommatins where the energy of fragmentation is certainly not sufficiently high to break the phenoxazone skeleton. A third reason could be the presence of an uncyclised form as those mentioned in Fig. 32, more specifically the reduced form which could lead more easily to fragments of XA. Unfortunately, MS/MS study of such compound has never been performed so far. These forms could be more compatible with **compound #1** (C₂₁H₁₆N₂O₁₀, DBE of 15). Uncyclised forms in Fig. 32 are described as the result of hydrolysis in acidic conditions³⁴⁷. Knowing that ASM^{POS} and therefore PF are obtained by dissolution in 1M HCl_(aq), a hydrolysis may occur during this operation, leading to uncyclised structures. This questions the stability of the pigments over time, pH, temperature and light exposition. Indeed, in a simple experimental test performed to evaluate the stability of ASM^{JOS}, we observed a marked decolouration, especially for samples exposed to sunlight (Fig. 84 – experimental part).

If this general hypothesis around ommatins is attractive, it does not explain the high molecular weight of di-charged ions and the numerous carboxyl groups identified by mass spectrometry. Although they might be present, it is also necessary to consider the presence of other members of ommochromes, namely ommins or ommidins. Their molecular weight, higher than those of

ommatins, and the numerous carboxyl group of their structure, as exemplified by ommin A (**Fig. 34**), are coherent with the collected data all along this study. However, there is neither unambiguous characterisation of such class of ommochromes in the literature nor available commercial standards. A mixture of ommins, ommidins and ommatins is not to exclude, especially considering the UV-vis absorption profile with bands at 464 and 496 nm close to the one of ommatins and ommins at 552 nm in **Fig. 49**. In addition, this also matches with different experimental observations explaining: *i*) the numerous carboxyl groups if di-charged ions are actually aggregates or small oligomers of **compounds #7 to #10** and *ii*) the formation of fragments during ionisation.

Whatever the definitive structure of these compounds, it presents a high number of carboxylic functions that remind the presence of several carboxylic groups of porphyrins, seen in Chapter II, and melanins, especially pheomelanin. Their occurrence in the pigmentation can lead to the binding of pigments to the calcite part of the shell via an ionic pigment-Ca²⁺ bond. It remains to elucidate if this was selected by nature, in order to ensure the binding of pigments designed for a specific function, or if pigments are a carboxylic-rich by-product of the physiology of the animal which "operation" results in their coinciding accumulation in the surface of the shell.

In the present state of the study the presence of ommochromes is supported by several experimental facts, although it does not completely rule out the presence of melanins and an unambiguous structure cannot be proposed yet.

III.4. CONCLUSION AND PERSPECTIVES

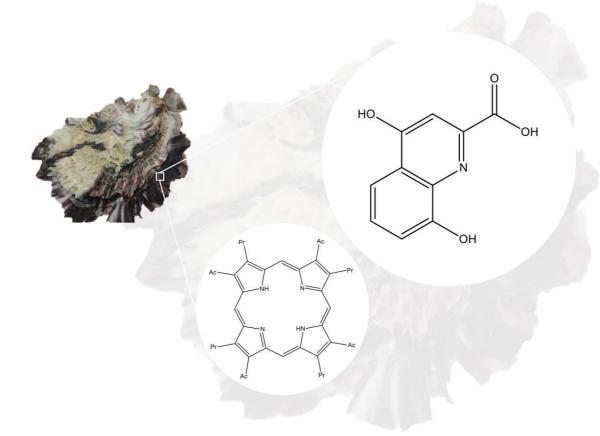
In Chapter II, we concluded to the presence of several porphyrins associated to others pigments forming altogether the purple colour of the oyster shell. Thanks to a decalcification/separation methods, a group of non-fluorescent compounds was separated from porphyrins. Their structure is characterised by a xanthurenic acid-like sub-molecular unit and probably substituted by numerous carboxyl groups, xanthurenic acid itself being unambiguously identified. This compound is described in the literature as a key metabolite of the biosynthesis of ommochromes^{347–349,355}. The solubility, UV-visible and mass spectroscopy data point toward the presence of ommochrome-based pigments and rule out the generally postulated presence of melanins alone.

A partial elucidation of the structure of these ommochromes has been achieved but pieces of the puzzle are still missing, especially in terms of isomerism and cyclisation of the compounds. A definitive structural identification might not be achievable since it must not be forgotten that ommochromes are oligomeric compounds that can also present variable structures. Meanwhile, a better structural definition is probably achievable by mass spectrometry with ionisation techniques leading to mono-charged ions such as those employing matrix assisted laser desorption ionisation. Multistage mass spectrometry (MSⁿ) should also be employed to follow the fragmentation of a given product ion. A comparison with standard substance has to be considered once available naturally or by synthesis. Experiments on the mantle edge epithelium by a non- or soft-destructive process could give reliable information on the structure of those pigments and could allow to rely a potential function in living conditions. To date, if their strong absorption in the visible region suggest a potential protection from light, other properties could emerge, eventually related with an oxidation process as observed in the production of uroporphyrin and derivatives.

IV. ACID-SOLUBLE PIGMENTS OF SHELLS OF

Crassostrea gigas: EVALUATION OF EXTRACTION

METHODS



One of the main challenges encountered during the description of the shell purple patterns of *C. gigas* was the low content of pigments and thus their selective extraction from calcite. During the first experiments, we observed that modifications of any parameters at any steps of the extraction process have significant effects on the quantity and the composition of pigments. Consequently, we thought pertinent to develop a brief study on the extraction methods in relation to the chemical nature and composition of the extracted pigments.

Three extraction methods were established in order to prepare samples concentrated in pigments and with a reduced content of calcium salts. Based on accumulated data, we propose in this chapter an evaluation of these extraction methods. Their impact on extraction yields, composition of pigments and their potential scalability at a larger scale are discussed.

IV.1. INTRODUCTION

In Nature, pigments generally represent only a negligible fraction of the whole mass of a living organism. In the particular case of molluscan shells, the extraction is limited by the calcareous phase, where pigments represent less than 1 % of the whole mass. For example, the extraction of 2.7 mg of a pure polyenic pigment from blue abalone shells was achieved by the dissolution of 30 kg of shells in aqueous acetic acid (150 L of AcOH at 5% V/V)³⁶³. The pigment is obtained after filtration, to remove the insoluble organic matrix, and precipitation by basification with NaOH_(aq) of the initial acidic solution until pH 10 "accompanied by a white flocculent precipitate", certainly Ca(OH)₂ for an initial [Ca²⁺] of \sim 5 mol. On the resulting solid mixture of Ca(OH)₂ and pigment, the latter is dissolved in AcOH_(aq) (10% V/V) and selectively extracted with ethyl acetate. This can be successfully achieved due the solubility of the pigment in ethyl acetate in contrast to calcium salts. A final purification stage is conducted by semi-preparative RPLC monitored by UV-vis spectroscopy at 254 nm for structural description of the pigment.

As illustrated above, the selective extraction of pigments is totally driven by the solubility and reactivity of all shell constituents. While the physicochemical properties of calcium carbonate are well established, those of the organic matrix and pigments are much more variable. In addition, it is no possible to anticipate the nature and the physicochemical properties of pigments. Besides, the solubility of pigments in water is counter-intuitive if we consider that the pigments of organism living in the sea are soluble in aqueous solutions but at higher pH are embedded in the calcareous structure of the shell that prevents their solubilisation. Then, in the simplest cases, assuming that pigments are soluble and stable in water, whatever the pH, and if the organic matrix is insoluble and stable, the dissolution of the shell allows to breakdown the calcium carbonate structure, releasing the pigments and the organic matrix, the latter can be

removed by filtration. In cases where pigments are insoluble at any pH, their selective extraction from the insoluble organic matrix can be achieved by specific treatment, such as extraction with organic solvent for carotenoids.

According to **Eq. 4**, dissolution of the calcareous shell is an acid-base reaction corresponding to the protonation of carbonate with formation of carbonic acid immediately followed by its decomposition into carbonic dioxide and water, the latter being displaced toward the elimination of CO₂ according to the Henry's law.

Eq. 4
$$CaCO_3/MO/Pigments_{(s)} + 2H^+_{(aq)} + 2X^-_{(aq)} + Ca^{2+}_{(aq)} + 2X^-_{(aq)} + Pigments_{(aq)} + Pigments_{(s)} + MO_{(aq)} + MO_{(s)} + H_2CO_{3(aq)} + H_2O_{(aq)} + CO_{2(aq)} + CO_{2(g)}$$

$$X = Cl, CH_3CO_2, ...$$

Any acid stronger than H₂CO₃ (pK_a 6,37) is able to produce such reaction. However, the nature of the corresponding anion, the conjugated base X⁻, can have different impacts. From data reported in the literature (**Table 13**), oxoacid with notable oxidising character like nitric and sulfuric acid are avoided. From this point of view, HCl or AcOH with no strong oxidising or reducing properties are generally used. However, they cannot be considered similar. First, the resulting calcium salts have different solubility. For example, using AcOH leads to calcium acetate with solubility of 347 g/L at 20 °C in water (2,2 mol/L)³⁷¹, slightly soluble in methanol but insoluble in acetone and ethanol. Differently, using HCl leads to calcium chloride much more soluble in water (811 g/L at 25 °C, 7,3 mol/L)³⁷¹, soluble in ethanol and methanol. These differences of solubility can lead to different processing. Besides, if pigments have amino groups, X⁻ will be the counter anion, a situation that can also result in different solubility. Finally, this counter anion may participate in the chemical transformations of pigments that

may occur subsequently or concomitantly to those produce by the very acidic medium, especially if they are easily hydrolysable or if they are complexed to a metal that can be demetallised by protonation. Besides the role of the conjugated base X⁻, the pH of resulting solution is a very important parameter and have to be considered according the chemical nature of the pigments to extract, especially when acidic or basic groups are suspected.

An original approach for the dissolution of the calcareous shell uses EDTA, a very well-known calcium chelating agent. In this case, the dissolution of CaCO₃ is based on the coordination of Ca^{2+} by the tetra-anionic specie of EDTA, generally called Y^{4-} , whose complexation constant is very high even at neutral pH (**Eq. 5**), a situation not accessible by other means. The resulting by product, in that case, is rich of the counter ion of Y^{4-} .

Eq. 5
$$Y^{4-} + Ca^{2+} \leq CaY^{2-}$$
 $K_1 = 10^{10.7} = 5.01.10^{10}$

This method was employed for the identification of protoporphyrin in molluscan shells. After repetitive dissolution at pH 7.2, the insoluble residue concentrated in protoporphyrin is partially dissolved in ACN/AcOH (4:1 V/V) and analysed by RPLC-HRMS. This method is convenient for the extraction of insoluble pigments such as carotenoids but requires extended dialysis for the elimination of CaY^{2-} and the counter ion of Y^{4-} if pigments are soluble.

In line with the previous chapters on the identification of acid-soluble pigments from shells purple patterns of *C. gigas*, we propose here to evaluate three extraction methods, namely salting out, CaF₂ precipitation and separative elution (**Fig. 63**). Salting out is based on the difference of solubility between pigments and calcium salts upon basification. Conversely, CaF₂ precipitation is based on the formation of insoluble salts at acidic pH while pigments are soluble. The separative elution is based on reverse phase chromatographic separation. Other

extraction methods were also tested during preliminary experiments but were not further developed. The method described by A. Comfort (separation of acid-soluble pigments by talc chromatography with HCl_(aq), **Table 13**) was not efficient to separate acid-soluble pigments from calcium salts (co-elution). Separation on silica gel led to the same effect. Extraction with supercritical CO₂ ranging from 9 to 55 MPa at 40°C was also tested. In addition, the method described by Cai *et al.* (2011) was reproduced but acid-soluble pigments were not extracted with ethyl acetate or dichloromethane.

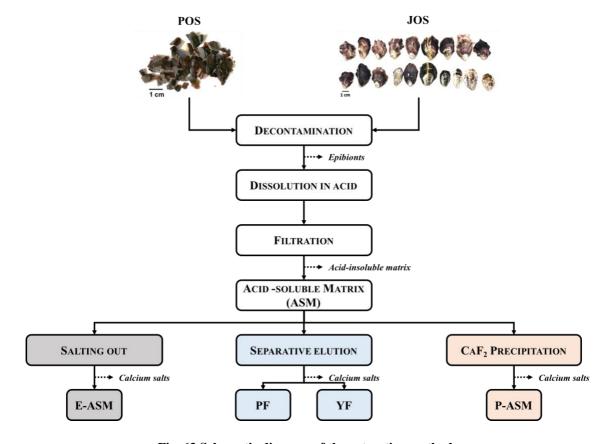


Fig. 63 Schematic diagram of the extraction methods.

Table 13 Significant studies on the extraction of molluscan shell pigments for structural identification.

Shell specimens	Pigments	Extraction methods	Identification methods	Ref.	
Conus australis Conus chaldeus Conus virgo Conus tinianus Coralliophilia neritiodea Drupa morum Donax serra Janthina janthina Pecten raveneli	s chaldeus (EDTA-insoluble) Addition of aqueous solution of Na ₂ EDTA Filtration and analysis of the residue stinianus liophilia neritiodea a morum x serra ina janthina		Raman spectroscopy	364	
Haliotis cracherodii	Indigotin or pyrrole (HCl _(aq) -soluble)	Dissolution in 5M HCl _(aq) Talc chromatography with acetone-HCl or 0.5M NaOH _(aq)	Gmelin's reaction UV-vis absorption spectroscopy	365,366	
3,000 species of molluscan shells including gastropods, bivalves scaphopods	Porphyrins (acid-soluble)	Dissolution in conc. HCl _(aq) or 33% H ₃ PO _{4(aq)} Filtration on cotton Dilution in 1M to 2.5M HCl _(aq) and talc chromatography with acetone in 3M HCl _(aq)	UV-vis absorption spectroscopy	367	
Malieus seapnopous Malleus regula Pinctada margaritifera Pinctada vulgaris Placuna sella Turbo marmoratus	Undefined (acid-soluble)	Dissolution in conc. $HCl_{(aq)}$ or 33% $H_3PO_{4(aq)}$ Filtration on cotton Dilution in 1M to 2.5M $HCl_{(aq)}$ and talc chromatography with acetone in 3M $HCl_{(aq)}$	UV-vis absorption spectroscopy	368	
Bulla sp. Bulla sp. Gibbula cineraria Malleus vulgaris Pinctada vulgaris Placuna sella Pteria radiata Trivia europoea Umbonium austral	Porphyrins (HCl _(aq) -soluble)	Dissolution in conc. $HCl_{(aq)}$ or 33% $H_3PO_{4(aq)}$ Filtration on cotton Dilution in 1M to 2.5M $HCl_{(aq)}$ and talc chromatography with acetone in 3M $HCl_{(aq)}$	Fluorescence Thin-layer chromatography	369	
Astraea tuber	Tetrapyrroles (HCl _(aq) -soluble)	Addition of HCl to shells immersed in distilled water Filtration on Whatman No. 1 Ion-exchange chromatography with HCl _(aq) and MeOH	UV-vis absorption spectroscopy Fluorescence	370	
Pinctada margaritifera Pinctada penguin	Porphyrins (EDTA-insoluble)	Milling and addition of 10% Na ₂ EDTA Dialysis against water Centrifugation Concentration of the supernatant by evaporation Chromatography on a Sephadex column with 0.05 mol/L phosphate buffer	Fluorescence spectroscopy at λ_{ex} 405 nm	297	
Pinctada margaritifera Porphyrins (HCl _(aq) -soluble) F 1 2 4 5 6 6 6 6 7 7 8 6 6 6 7 7 8 8 9 9 9 9 9 9 9 9 9 9 9		Repetitive dissolution in 2M HCl _(aq) Filtration on paper Talc chromatography with water followed by 1% sodium acetate and 10% aqueous ammonia Evaporation of aqueous ammonia and dissolution in sulfuric acid with methyl alcohol Extraction with chloroform and whashing	NPLC-Fluorescence at λ_{ex} 405 nm	298	
Haliotis discus	Polyene (Ethyl acetate ₎ -soluble)	Dissolution in 5% AcOH _(aq) Filtration Salting out by addition of NaOH _(aq) Dissolution in 10 AcOH _(aq) Extraction with ethyl acetate Preparative RPLC	Thin-layer chromatography UV-vis absorption spectroscopy Infrared spectroscopy ¹ HMR spectroscopy Mass spectrometry (ESI-) Solubility, stability Colour value	363	
Crassostrea gigas	Eumelanins (HCl _(aq) -insoluble residue)	Manual decontamination Selection of AMS Milling Dissolution in 6M HCl _(aq) Filtration Hydrolysis with 6M HCl _(aq)	UV absorption spectroscopy Infrared spectroscopy	30	

Chapter IV. Acid-soluble pigments of shells of Crassostrea gigas: evaluation of extraction methods

		Filtration		
		Extraction with diether at 42°C and distilled		
		water		
		Drying at 80°C		
Conus ebraeus	Protoporphyrin	Milling	Mass spectrometry	311
Conus purpurascens	(EDTA-insoluble)	Addition of Na ₂ EDTA pH 7.2	(ESI+)	
Hastula hectica		Centrifugation		
Argopecten sp.		Solubilisation in acetonitrile-acetic acid		
Clanculus margaritarius	Porphyrins	Dissolution of shell fragments in 37% HCl _(aq)	RPLC-Fluorescence	319
Clanculus pharaonius	(HCl _(aq) -soluble)	Dilution with deionised water	at λ_{ex} 405 nm	
Calliostoma zizyphinum				
•	Eumelanin	Dissolution in 1M HCl _(aq)	RPLC-UV	
	(HCl _(aq) -insoluble residue)	Evaporation to dryness		
		Oxidation with 30% H ₂ O _{2(aq)}		

IV.2. RESULTS

IV.2.1. Sample preparation

IV.2.1.1. Decontamination

In order to limit the extraction of pigments originating from epibionts, a decontamination treatment is applied by immersion of POS in a 1% NaOCl_(aq) followed by immersion in deionised water (2h in each case). Sonification is employed to accelerate the treatment without the use of mechanical stirring. After decontamination, samples are not decolourised, the NaOCl_(aq) solution is yellowish with the presence of flocculent residues (apparently of organic nature). The deionised water is colourless, a thin shell powder is collected on the bottom flask, probably as a result of the sonication. In these conditions, the prismatic structure of POS, observable by SEM, was cleaned of its epibionts and apparently not degraded (**Fig. 64**). This decontamination treatment was evaluated efficient enough for a use in routine on batches varying from few grams to couples of kilograms.

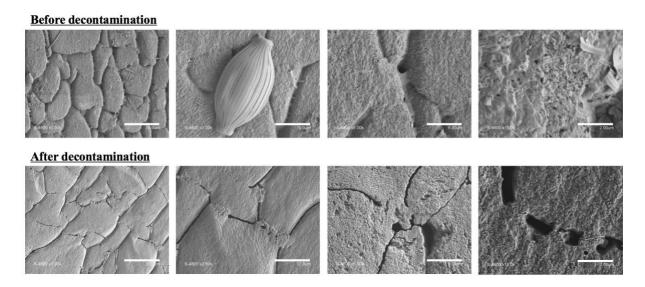


Fig. 64 SEM images of surface of POS before and after decontamination with 1% $NaOCl_{(aq)}$ and deionised water, with the assistance of sonification.

IV.2.1.2. Dissolution in acid

Both HCl and AcOH were first tested to dissolve the shell at 25° C. The complete dissolution of POS is achieved after 30 minutes using 1M HCl_(aq) (pH ~ 0.1), whereas 120 minutes are required with 1M AcOH_(aq) (pH ~ 2.4). The dissolution is spontaneous and the colouration of the solution is an obvious evidence of the solubilisation of pigments at this pH (**Fig. 65**). This suggests that they were intimately trapped, associated or bonded inside the carbonate-based microstructure. In this coloured solution, a precipitate is still present, long after the end of CO₂ evolution. It corresponds to the insoluble organic matrix that is eliminated by filtration and recovered as a colourless solid.

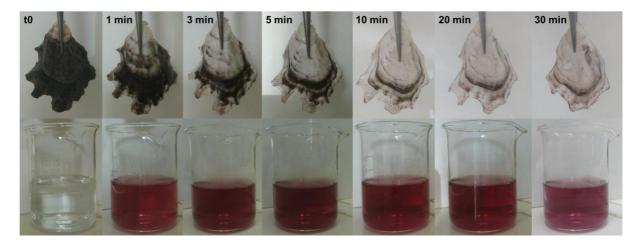


Fig. 65 Dissolution of JOS in 1M HCl_(aq).

According to this process, a stock solution of ASM^{POS} (pH 0.74) is prepared by dissolution of POS in 1M HCl_(aq). The latter was selected because, upon drying, excess of HCl can be easily eliminated at room temperature by evaporation. This ASM^{POS} is filtered to remove the insoluble organic matrix and stored in the dark at low temperature (-21°C). The RPLC-DAD-HRMS analysis of this solution shows xanthurenic acid eluted at 4.97 min and pigments hypothesised as ommochromes between 7 to 10 min (**Fig. 66a-d**). The molecular ion of uroporphyrin is also

detected but is more clearly identified at 13.23 min after sample concentration by evaporation (**Fig. 66e-f**).

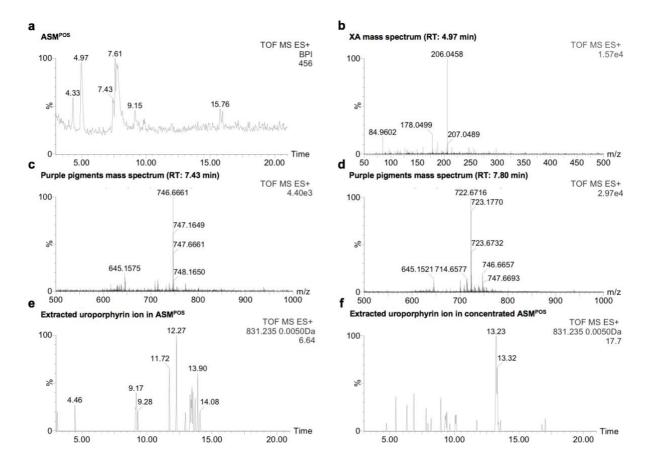


Fig. 66 RPLC-HRMS analysis of ASM^{POS}. (a) BPI chromatogram of ASM^{POS}. (b) Mass spectrum of xanthurenic acid. (**c-d**) Mass spectra of pigments hypothesised as ommochromes. (**e-f**) Chromatograms of extracted uroporphyrin ion from ASM^{POS} and concentrated ASM^{POS}, respectively.

IV.2.2. Comparison of the methods of extraction of pigments

The three methods of extraction are compared in terms of extraction yield, solubility and composition. These methods were repeated on ASM prepared from shells of juvenile oysters (ASM^{JOS}).

IV.2.2.1. Salting out

The postulate behind the salting out method is that the solubility of some of the pigments is pH dependent and can be low enough to recover them until the beginning of the precipitation of Ca(OH)₂ that starts when the concentration of OH⁻ is high enough. Obviously, this method does not allow to recover pigments precipitating at very high pH since they would be mixed with Ca(OH)₂.

Starting from an ASM^{POS} solution at pH 0.74, the addition of NaOH_(aq) first results in its neutralisation until pigments start to precipitate according to:

$$Ca^{2^{+}}_{(aq)} + 2Cl^{-}_{(aq)} + Pigments^{+}_{(aq)} + 2H^{+}_{(aq)} + 2Cl^{-}_{(aq)}$$

$$Na^{+}_{(aq)} + 2OH^{-}_{(aq)}$$

$$Ca^{2^{+}}_{(aq)} + 2Cl^{-}_{(aq)} + Pigments^{+}_{(aq)} + H_{2}O_{(aq)} + 2Cl^{-}_{(aq)} + 2Na^{+}_{(aq)}$$

$$Na^{+}_{(aq)} + 2OH^{-}_{(aq)}$$

$$Na^{+}_{(aq)} + 2OH^{-}_{(aq)}$$

$$Ca(OH)_{2(s)} + 2Na^{+} + 2Cl^{-}_{(aq)} + Pigments_{(s)}$$
Precipitation of Ca(OH)₂ and eventually pigments

The solubility of Ca(OH)₂ is pH dependent (solubility of Ca(OH)₂ ≈1,73 g·L⁻¹ at 20 °C, product of solubility Ks = 5,02 × 10⁻⁶ à 25 °C). From a solution of ASM^{POS} containing 0.499 mol/L of Ca²⁺ (POS considered as 100 wt.% of CaCO₃), the initial Ca(OH)₂ precipitation pH can be predicted according to: Ks = [Ca²⁺] x [OH⁻]² \rightarrow [OH⁻] = $\sqrt{\text{Ks/[Ca^{2+}]}}$ = 3.172 10⁻³ mol/L

$$\rightarrow$$
 pH = -log (Ke/[OH⁻]) \approx 11.51

A first test was performed with a solution of commercial $CaCO_3$ dissolved in 1M $HCl_{(aq)}$ (0.500 mol/L of Ca^{2+}). The beginning of $Ca(OH)_2$ precipitation by the addition of 1M $NaOH_{(aq)}$ starts at $pH \approx 11.0$.

Experimentally, the basification of ASM^{POS} from pH 0.7 to 5.0 leads to important variation of

its colour, from red-purple to green-violet, besides, no formation of a persistent precipitate is observed (**Fig. 67**). The colour of ASM^{POS} is clearly depending on its pH, reflecting the halochromism of the compounds reported in Chapter II. At pH 5.4, a discolouration is initiated, accompanied by the formation of a coloured precipitate until pH 10.3. This indicates that pigments have been precipitated. The loss of their coloured property in solution is not excluded. At pH > 10.0, the solution is definitively colourless and a white solid starts to precipitate. Therefore, to recover what is assumed as pigments, the addition of NaOH_(aq) is stopped at pH 10, and the precipitate is separated by centrifugation and freeze-dried. Freeze-drying is employed to remove the residual water by limiting a potential oxidative or thermal degradation. The resulting powder is a mixture of pigments and NaCl resulting from the neutralisation of the ASM^{POS}. Therefore, the powder is washed with ultrapure water (pH \approx 5-6) in order to remove NaCl adsorbed on the precipitated pigments. The washing solution is colourless suggesting that pigments are not solubilised. This is surprising since the ASM^{POS} was still coloured at pH 6,

indicating that some pigments were certainly soluble in this condition, but not after freezedrying and washing. After washing, the solid residue, named E-ASM, is finally freeze-dried.



Fig. 67 Extraction of E-ASM^{POS}.

At larger scale, working on ~ 1.8 L of ASM^{POS} (~ 90 g of POS), the precipitation of pigments starts at pH ~ 5 but an orange colouration of the supernatant is observed at pH > 10 suggesting that a fraction of pigments is soluble. This extraction method was repeated on batches of ASM^{JOS} of ~ 600 mL by keeping the final precipitation pH at 10 for comparative evaluation (**Table 14**). The extraction yields depend mainly on the sample used for extraction, varying from 0.22 wt.% for POS to approximately 0.05 wt.% for JOS. This is consistent with the general colour of samples; while POS were specifically selected for their fully purple coloured aspect, JOS were partially white (specially the inner surface).

Table 14 Extraction yields of E-ASM extracted from POS and JOS.

Samples	Mass (g)	Extraction yield (wt.%)
Juvenile oyster shells (JOS)	30.1	0.051
Juvenile oyster shells (JOS)	29.9	0.037
Juvenile oyster shells (JOS)	29.9	0.061
Purple oyster shell fragments (POS)	2.0	0.240
Purple oyster shell fragments (POS)	9.9	0.210

Table 15 Qualitative estimation of the solubility of E-ASM^{POS}.

Solvents	Solubility
Acetic acid (1M, aqueous)	+++
Acetonitrile	-
Cyclohexane	-
Dichloromethane	-
Diethyl ether	-
Ethanol	-
Ethyl acetate	-
Hexane	-
Hydrochloric acid (1M, aqueous)	+++
Methanol	-
Sodium hydroxide (1M, aqueous)	+++
Ultrapure water	-

The solubility of E-ASM^{POS} was tested in different medium with the idea to possibly fractionate and isolate different compounds. So far, E-ASM^{POS} is only soluble in NaOH_(aq) and aqueous acids (qualitative determination by centrifugation after 60 min magnetic stirring at 1 mg/mL, **Table 15**).

The E-ASM^{POS} was analysed for elemental determination by EDX (**Table 16**). Approximately 5.5 at.% of Ca is detected, showing the relative efficiency of the method. The sample is rich in carbon, oxygen and nitrogen, at least due to pigments identified in the previous chapters. A significant amount of chloride is observed (11.78 at.%), certainly due to ionic interactions with organic compounds or cations during the dissolution in 1M HCl_(aq). The phosphorus content is high (2.19 at.%), suggesting the presence of phosphate. Sodium probably results from residual NaCl generated by basification with NaOH. Sulfur could indicate the presence of soluble methionine and cysteine moieties, or the presence of sulfate groups. The identification of other elements such as Al, Si, Cr, Mg, Fe and Mn has to be considered with the low solubility of their corresponding hydroxide that can precipitate. The presence of these metal cations could be the result of bioaccumulation in the shell from the aquatic environment as mentioned in Chapter I.

Table 16 Elemental composition of E-ASMPOS.

Elements	at.% (triplicate)
Carbon	25.61 ± 3.16
Nitrogen	2.57 ± 1.02
Oxygen	21.47 ± 1.24
Sodium	0.51 ± 0.14
Magnesium	0.52 ± 0.12
Aluminium	0.15*
Silicon	0.46 ± 0.08
Phosphorus	2.19 ± 0.22
Sulfur	0.14 ± 0.04
Chloride	11.78 ± 2.16
Potassium	0.05 ± 0.02
Calcium	5.53 ± 1.06
Chrome	0.18 ± 0.02
Manganese	0.33 ± 0.20
Iron	0.73 ± 0.63
Brome	0.12 ± 0.02

^{*:} detected once.

The RPLC-DAD-HRMS analysis of E-ASM^{POS} presents a low intensity signal at 13.46 min corresponding to uroporphyrin (**Fig. 68a**). Pigments hypothesised as ommochromes are eluted from 6 to 12 min as shown in chromatogram obtained at 405 nm in **Fig. 68b**. Additionally, xanthurenic acid is eluted at 4.95 min (**Fig. 68c**) and numerous other peaks are observed from 3 to 10 minutes (blue stars in the BPI chromatogram in **Fig. 68d**). The examination of their mass spectra is characterised by a successive increment of an exact mass of 44.026 Da (**Fig. 68e-f**) corresponding to a C₂H₄O pattern, a typical signature of ethylene glycol-based polymers. Their origin is detailed in the discussion section. The structure of the compound eluted at 10.48 min was analysed by MS/MS (**Fig. 68g-h**). Its molecular formula C₁₁H₆O₃ and fragmentation pattern in ESI+ are in agreement with psoralen or its isomers by comparison with the mzCloudTM database. The confirmation of its structure is presently in progress by co-injection with a psoralen standard. Other compounds eluted at retention time higher than 12.0 min were not investigated yet. It would be interesting to carry out a dosage of the different species with another technique than RPLC-HRMS, given some compounds can be easily ionisable, others not at all.

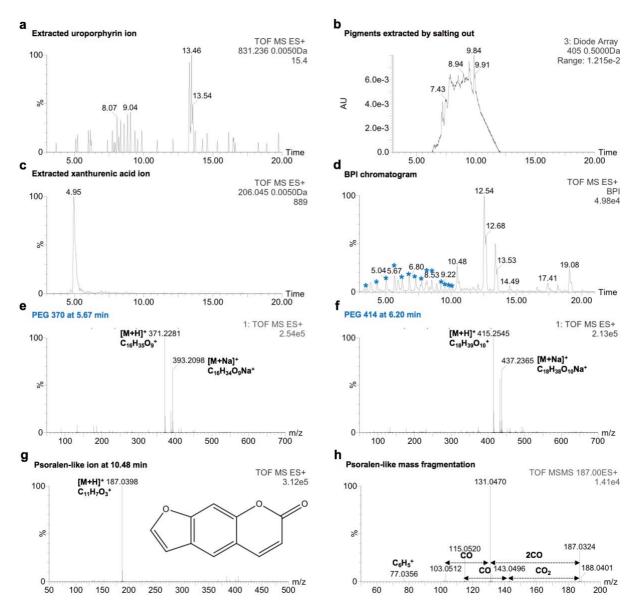


Fig. 68 RPLC-DAD-HRMS analysis of E-ASM^{POS}. (a) Extracted uroporphyrin ion chromatogram. (b) Chromatogram at 405 nm. (c) Extracted xanthurenic acid ion chromatogram. (d) BPI chromatogram showing the peaks corresponding to ethylene glycol-like polymers. (e-f) Mass spectra at 5.67 min and 6.20 min, respectively. (g-h) Mass spectrum of the compound attributed to a psoralen-like structure eluted at 10.48 min and corresponding MS/MS spectrum, respectively.

IV.2.2.2. Separative elution

This method, based on reverse phase chromatographic separation, is very efficient for the preparation of samples concentrated in pigments as mentioned in Chapter III. The ASM^{POS} is separated on an opened column filled with a C18 grafted silica stationary phase (~ 24 wt.% of C). The pH of the stationary phase is fixed with 1M HCl_(aq). From the initial deposition of ASM^{POS}, calcium salts elute rapidly as a large whitish band since no strong interactions can occur with the non-polar stationary phase. This is performed by elution with 1M HCl_(aq) followed by 0.1% TFA_(aq) (pH ~ 2). At this stage, pigments are not eluted as predicted by the RPLC of ASM^{POS}. After elution of the Ca²⁺-containing salts, a first set of pigments elutes as a large purple band with water/acetonitrile (80:20 V/V) acidified with 0.1% TFA. The resulting fraction does not exhibit photoluminescence. A yellow band still fixed on the top of the stationary phase is eluted with acetonitrile with 0.1% TFA and its pink photoluminescence under 405 nm indicates the presence of uroporphyrin identified in the ASM^{POS} stock solution. The purple (PF) and yellow (YF) fractions are finally freeze-dried to recover solid samples ready for further analysis.

This method was repeated on different volumes of ASM^{POS} and ASM^{JOS} by keeping the same m_{stationary phase}/V_{ASM} ratio. The decalcification of 2 L of ASM^{JOS} (**Fig. 69b-d**) is comparable to ASM^{POS}. However, the separative elution is visually different. While the large purple band is first eluted with water/acetonitrile (80:20 V/V + 0.1% TFA), an orange and a pink band (**Fig. 69f**) are eluted with acetonitrile with 0.1% TFA. The resulting fraction is photoluminescent under 405 nm. These bands are certainly concentrated in porphyrins. In addition, after complete elution, the resulting stationary phase is slightly coloured, indicating that a minor fraction of pigments is not eluted (**Fig. 69f**).

The extraction yields vary from 0.38 wt.% for POS to approximately 0.04 % for JOS, these are higher than those obtained by salting out method, although they are similarly sample dependent (**Table 17**). The extraction yields obtained from the photoluminescent fraction (including YF^{POS}) are very low, therefore, we preferred to solely conduct the analysis of composition by RPLC-DAD-HRMS.

After freeze-drying, the purple fraction is soluble in $NaOH_{(aq)}$, aqueous acids and slightly soluble in EtOH, MeOH and ultrapure water (**Table 18**).



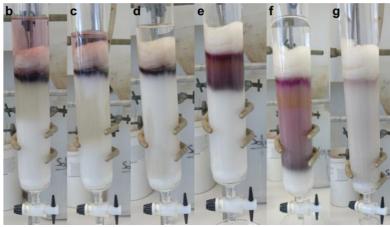


Fig. 69 Separative elution of pigments from ASM^{JOS}. (a) General experimental set-up. (b-c) Deposition of ASM^{JOS}. (d) Elution of calcium salts. (e) Elution of the purple fraction PF^{JOS}. (f) Orange and pink bands corresponding to the photoluminescent fraction. (g) Stationary phase after elution.

Table 17 Extraction yields of fractions obtained from POS and JOS.

Samples	Mass (g)	Purple fraction extraction yield (wt.%)	Photoluminescent fraction extraction yield (wt.%, mg)	Global extraction yield (wt.%)
Purple oyster shell fragments (POS)	2.0	0.381	n.d.	0.381
Purple oyster shell fragment (POS)	10.1	0.362	n.d.	0.362
Juvenile oyster shells (JOS)	100.0	0.034	0.004 (4.3)	0.038
Juvenile oyster shells (JOS)	100.0	0.044	0.004 (4.7)	0.049

Table 18 Qualitative estimation of the solubility of PFPOS.

Solvents	Solubility of the purple fraction
Acetic acid (1M, aqueous)	+++
Acetone	-
Cyclohexane	-
Chloroform	-
Dichloromethane	-
Diethyl ether	-
Ethanol	+
Ethyl acetate	-
Isopropyl alcohol	-
Hexane	-
Hydrochloric acid (1M, aqueous)	+++
Methanol	+
Methanol containing 1% of 12M HCl _(aq)	+++
Methanol containing 0.1% of 12M HCl _(aq)	+++
Sodium hydroxide (1M, aqueous)	+++
Ultrapure water	+

This method leads to a low content of calcium in the purple fraction, approximately 1.84 at.% by EDX analysis (**Table 19**), lower than the 5.5 at.% obtained by salting out. Chloride is also significantly reduced compared to the salting out method (3.86 wt.% and 11.78 wt.%, respectively). Besides, almost all the elemental concentrations are different. The sulfur content is more than double while the phosphorous content is divided by almost 6. Like E-ASM, other elements are present such as Al, Si, Mg, Fe, K but other are also present here like Br and especially Pb, but their concentrations are notably different. A possible explanation may be found in the presence of impurities from solvents and C18 leading to their concentration in the sample, for example, the supplemental use of $HCl_{(aq)}$ during decalcification (impurities are reported as: Pb ~ 1 ppm, Br \leq 5 ppm, NH4 \leq 1 ppm, PO4 \leq 0.5 ppm, SO3 \leq 1 ppm, SO4 \leq 1 ppm, Al \sim 0.1 ppm, As \leq 0.01 ppm).

Table 19 Elemental composition of PFPOS.

Elements	at.% (triplicate)
Carbon	32.95 ± 2.21
Nitrogen	2.45 ± 0.56
Oxygen	14.65 ± 2.63
Magnesium	0.19 ± 0.02
Aluminium	0.26 ± 0.04
Silicon	0.26 ± 0.08
Phosphorus	0.48 ± 0.16
Sulfur	0.38 ± 0.14
Chloride	3.86 ± 1.18
Potassium	0.35 ± 1.18
Calcium	1.84 ± 0.32
Iron	0.50 ± 0.27
Lead	0.33*

^{*:} detected once.

RPLC-DAD-HRMS analysis is performed on the yellow and purple fractions. Pigments hypothesised as ommochromes are eluted between 6 and 12 min (**Fig. 70a**) in the purple fraction, as well as xanthurenic acid (eluted at 4.89 min, **Fig. 70b**) and ethylene glycol-based polymers (from 3 to 10 min, **Fig. 70c-e**).

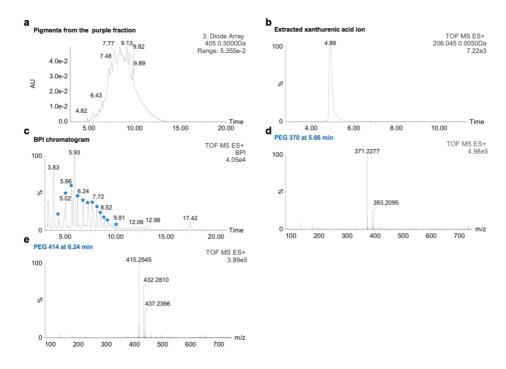


Fig. 70 RPLC-DAD-HRMS analysis of PF^{POS}. (a) Chromatogram at 405 nm. (b) Extracted xanthurenic acid ion chromatogram. (c) BPI chromatogram showing the peaks corresponding to ethylene glycol-like polymers (blue stars). (d-e) Mass spectra at 5.66 min and 6.24 min, respectively.

Uroporphyrin and heptacarboxylic acid porphyrin are concentrated in the yellow fraction (retention time 13.27 and 14.21 min, respectively, **Fig 71b-c**). The peak eluted at 9.38 min with clusters of di-charged ions at m/z 519.6488, 528.6563 and 536.6508 previously identified in Chapter III, are also identified in the yellow fraction (**Fig. 71d**). The psoralen-like compound (eluted at 10.46 min, **Fig. 71e**) and the PEG-like polymer (between 10.5 to 14.0 min) are also identified while are absent in the purple fraction (green stars in **Fig. 71a and 71f**). Numerous other compounds, including that eluted at 4.05 min, were not investigated yet.

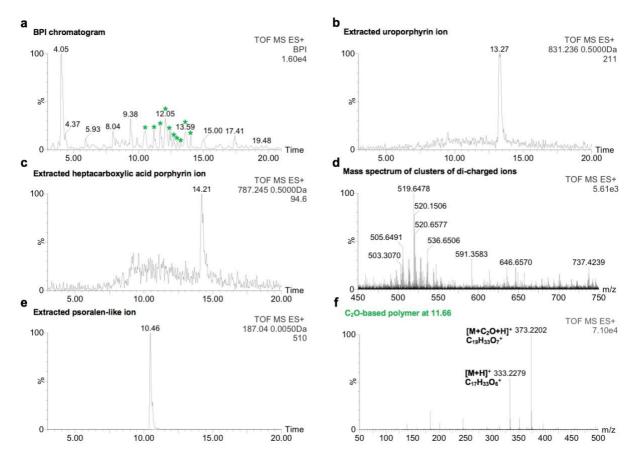


Fig. 71 RPLC-HRMS analysis of YF^{POS}. (a) BPI chromatogram showing the peaks corresponding to C₂O-based polymers (green stars). (b) Extracted uroporphyrin ion chromatogram. (c) Extracted heptacarboxylic acid ion chromatogram (d) Mass spectrum of clusters of di-charged ion eluted at 9.38 min. (e) Extracted psoralen-like ion chromatogram. (f) Mass spectrum of C₂O-based polymers eluted at 11.66 min.

IV.2.2.3. CaF_2 precipitation

The CaF₂ precipitation method, introduced for the first time in Chapter II, is based on the very low solubility of CaF₂ ($K_s = 3.9.10^{-11}$)³⁷¹. Hydrofluoric acid is soluble in water (up to 27.6 M). It is a low boiling point (19.5 °C for a 27.6M HF_(aq)) weak acid with pK_a of 3.2 ($K_a = [H^+][F^-]/[HF] > 0$ due to the high dissolution enthalpy of HF and the strength of the H-F bond³⁷²). When added in stoichiometric amount to solution of Ca²⁺, it allows an almost total elimination of Ca²⁺ as a CaF₂ precipitate according to **Eq. 6**. If a slight excess of HF is used to preserve an acidic pH, it can be eliminated by slow evaporation along with HCl and by-products of the process. Differently from the other methods, it allows to directly recover the acidic solution of pigments (pH bellow 2) and lead to solid residue upon evaporation.

Eq. 6
$$Ca^{2+}_{(aq)} + 2Cl^{-}_{(aq)} + Pigments_{(aq)} + 2H^{+}_{(aq)} + 2F^{-}_{(aq)} \leftrightarrows CaF_{2(s)} + 2H^{+}_{(aq)} + 2Cl^{-}_{(aq)} + Pigments_{(aq)}$$

This extraction method involved a 27.6M aqueous solution of HF, which is easy to handle with usual lab propylene wares but must be manipulated with caution in a dedicated area. In order to reduce the amount of HF as much as possible, the ASM^{POS} is first concentrated under vacuum at 25°C until the beginning of calcium salts precipitation. HF_(aq) is then added dropwise to ASM^{POS} until no more precipitate is formed. After rapid centrifugation, total precipitation of the white CaF₂ precipitate is verified by the absence of any precipitation upon the addition a drop of HF to the coloured supernatant. After centrifugation, evaporation and washing, a solid residue named P-ASM is obtained after freeze-drying.

As with others methods, extractions yields are sample dependent, yielding approximately 0.22 % for POS and 0.04 % for JOS (**Table 20**). P-ASM^{POS} is soluble in acidic and alkali solutions (pH < 2.5 and > 12, respectively) but insoluble in ultrapure water at pH \approx 5-6, ethyl acetate, EtOH and dichloromethane.

Table 20 Extraction yields of P-ASM extracted from POS and JOS.

Samples	Mass (g)	Extraction yield (%)
Juvenile oyster shells (JOS)	29.9	0.039
Purple oyster shell fragments (POS)	10.7	0.190
Purple oyster shell fragments (POS)	2.0	0.240

This method is particularly efficient to obtain sample with a very low calcium content ~ 0.15 at.% as detected by EDX analysis (**Table 21**). The carbon, oxygen and nitrogen contents are in line with previous extracts. Compared to E-ASM^{POS} and PF, Al, Si, Fe, K, Cr and Br are not detected. These elements are perhaps co-precipitated with Ca or eliminated by the washing step with water. Besides, this method requires much less solvent compared to other methods, thus the level of impurities should be less concentrated. Conversely, soluble cations like Na²⁺, Cl⁻, K⁺ can be concentrated during the last evaporation step.

Table 21 Elemental composition P-ASMPOS.

Elements	at.% (triplicate)
Carbon	32.00 ± 0.33
Nitrogen	3.45 ± 0.98
Oxygen	23.31 ± 3.43
Sodium	2.38 ± 0.04
Magnesium	0.16 ± 0.02
Phosphorus	2.44 ± 0.12
Sulfur	0.83 ± 0.02
Chloride	3.35 ± 0.20
Potassium	0.60 ± 0.04
Calcium	0.13*
Manganese	0.23 ± 0.08

^{*:} same value for the three determination.

All the major pigments described in previous chapters are identified by RPLC-DAD-HRMS analysis of P-ASM^{POS}. Pigments hypothesised as ommochromes are eluted from 5 to 15 min

(**Fig. 72a**) and major porphyrins (uroporphyrin, heptacarboxylic acid porphyrin and turacin) are co-eluted with ommochromes at 13.22, 14.17 and 14.80 min, respectively (**Fig. 72a-d**). Besides, xanthurenic acid (**Fig. 72e**), the psoralen-like compound (**Fig. 72g**) and polymers previously identified in purple and yellow fraction are also identified (blue and green stars in **Fig. 72f**).

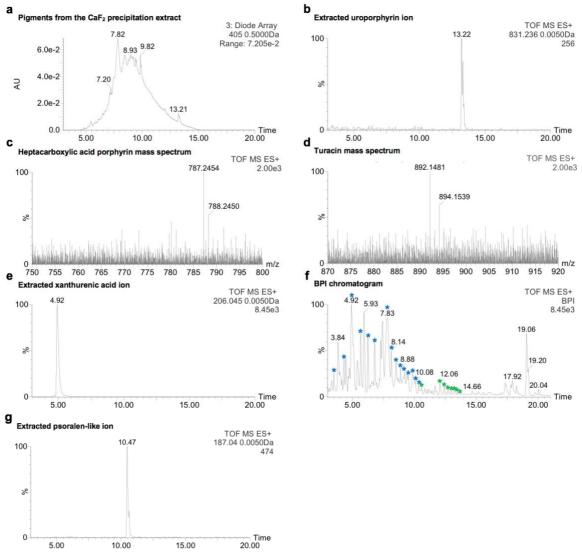


Fig. 72 RPLC-DAD-HRMS analysis of P-ASM^{POS}. (a) Chromatogram at 405 nm. (b) Extracted uroporphyrin ion chromatogram. (**c-d**) Mass spectra of heptacarboxylic acid porphyrin and turacin, respectively. (**e**) Extracted xanthurenic acid ion chromatogram. (**f**) BPI chromatogram showing the peaks corresponding to ethylene glycol-based and C₂O-based polymers. (**f**) Extracted psoralen ion chromatogram.

IV.3. DISCUSSION

IV.3.1. Impact of extraction methods on extraction yield and scalability

The three methods investigated in this study enabled to extract acid-soluble compounds with comparable extraction yields (**Table 22**), variation depending much more on the shell sample than the extraction method (POS leads to much higher yield than JOS). In this regard, sample collection has to be designed according to the level of the required resource, knowing that POS collection is conducted by hand and JOS can be directly supplied by oyster breeders.

Table 22 Extraction yields of acid-soluble compounds extracted from ASM^{POS} and ASM^{JOS} by the three methods.

Samples	Salting out (wt.%)	Separative elution (wt.%)	CaF ₂ precipitation (wt.%)
Purple oyster shell fragments (POS)	0.22	0.37	0.21
Juvenile oyster shells (JOS)	0.05	0.04	0.04

In terms of scalability, the separative elution method seems interesting, suitable for the extraction of pigment from volumes of ASM varying from few mL to 2L. This method allows to prepare water- and EtOH-soluble fractions of pigments, which is an advantage for a use at liquid state. In addition, this method allows to separate two groups of pigments, may be three, in a single operation within few hours in a quasi-continuous process, starting from dissolution to sample ready for freeze-drying. This process requires the use of a high cost C18 grafted silica (277€/100g to obtain approximately 40 mg from JOS), but it can be easily regenerated.

The CaF₂ method is advantageous by its simplicity and the use of minimal volumes of solvents. If well designed at larger scale, this method seems more economic than the separative elution, requiring only plastic wares, tools and standard filters. In its present state, the major limitation is the solubility of the resulting extract. Further developments are required for a use at liquid state at neutral pH (if needed). Besides, considering the safety issues, this method should be

preferred for analytical purposes. The salting out method is also economic, especially if basification is conducted with ammoniac that can be easily evaporated in contrast to the water formed by the addition of $NaOH_{(aq)}$. However, the weak solubility of the resulting extract, is a serious limit for the development of applications based on liquid state pigments.

In a more general way, freeze-drying employed in this study is convenient at analytical scale for the preparation of dry extract at 25°C, but its use at higher scale has to be seriously questioned. This operation is slow and such equipment requires high resources and investment. Besides, a potential contribution on the relative insolubility of extracts is not excluded. Indeed, while P-ASM and E-ASM, not soluble in ultrapure water and MeOH, are obtained after suspension in a minimum volume of water and freeze-drying, PF, visually more soluble, is obtained after freeze-drying of pigments solubilised in a large volume of eluent. In this condition, after freeze-drying, PF looks more "porous" than P-ASM and E-ASM, that may result in easier solubilisation. Drying at 30°C, atmospheric condition, should be evaluated.

IV.3.2. Impact of extraction methods on composition

The three extraction methods allow to prepare samples concentrated in acid-soluble compounds and with a reduced content of calcium; by decreasing order: salting out ~ 5.5 at.%, separative elution ~ 1.84 at.% and CaF₂ precipitation ~ 0.15 at.%. In addition, the methods have also an impact on the concentration of non-metal element like S and P and also on metal like Fe, Cr, Si, Al, etc. Although their concentrations are generally below 3-5.5 at.% their presence raise many questions on their origin (exogenous versus endogenous, bioaccumulation, contamination), role and precise determination, all being without clear answer at present.

Table 23 Composition of extracted pigments obtained by the three methods (i: identified, n.i.: not identified).

Compounds	ASMPOS			e elution	P-ASM ^{POS}	
-			PF^{POS}	YFPOS		
Ommochromes	i.	i.	i.	i.	i.	
Uroporphyrin	i.	i.	n.i.	i.	i.	
Heptacarboxylic acid porphyrin	n.i.	n.i.	n.i.	i.	i.	
Turacin	n.i.	n.i.	n.i.	n.i.	i.	
Xanthurenic acid	i.	i.	i.	n.i.	i.	
Psoralen-related structure	n.i.	i.	n.i.	i.	i.	
PEG	n.i.	i.	i.	n.i.	i.	
C ₂ O-based polymers	n.i.	n.i.	n.i.	i.	i.	

Among the major porphyrins described in Chapter II, uroporphyrin was identified whatever is the method of extraction (**Table 23**), variation is only observed on its relative content (**Fig. 73**). Indeed, samples of E-ASM^{POS}, PF^{POS} and P-ASM^{POS} were prepared at the same concentration (5 mg/mL). The extracted uroporphyrin ion chromatograms are normalised at an intensity of 300. In this representation, the peak of uroporphyrin in P-ASM^{POS} is the most intense (~ 85%, **Fig. 73b**), suggesting the highest relative concentration. The intensity in YF (~ 30%, **Fig. 73d**) has to be multiplied by a factor 3 for comparison since this sample was diluted by a factor 3 compared to P-ASM^{POS}, E-ASM^{POS} and PF^{POS}. Heptacarboxylic acid porphyrin was identified only in P-ASM^{POS} and in the yellow fraction whereas turacin was only identified in P-ASM^{POS}. More generally, the CaF₂ precipitation method appears as the most adapted for the extraction of porphyrins. Knowing that the pH is kept < 2 all along this process, porphyrins are kept soluble, certainly by protonation of NH-pyrroles.

The salting out method seems "selective" for the extraction of ommochromes. Compared to P-ASM^{POS} analysed at the same concentration, only uroporphyrin was identified in E-ASM^{POS}, the salting out method leads to low porphyrins-content. The intensity of the molecular uroporphyrin ion is much less intense in the extracted chromatogram compared to other methods, suggesting a lower concentration (**Fig. 73a**). A fraction of porphyrins is certainly

soluble at pH > 10 due to the possible deprotonation of carboxyl groups and NH-free of pyrroles.

The separative elution method allows a partial separation of porphyrins from the set of ommochromes. Furthermore, turacin is not identified, certainly due to a demetallation process occurring during decalcification with $HCl_{(aq)}$ by protonation of N-pyrroles coordinated to Cu(II). Another possibility would be that turacin was not eluted in these conditions.

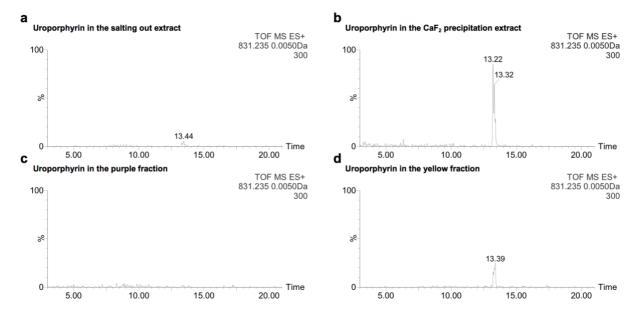


Fig. 73 Chromatograms of extracted uroporphyrin ion normalised at an intensity of 300. (a) Extracted uroporphyrin ion in E-ASM^{POS}. (b) Extracted uroporphyrin ion in P-ASM^{POS}. (c-d) Extracted uroporphyrin ion in the PF^{POS} and YF^{POS}, respectively.

Besides ommochromes and porphyrins, others compounds were extracted. Xanthurenic acid is particularly concentrated in P-ASM^{POS} and the purple fraction (**Fig. 74**). Related to ommochrome in terms of biosynthetic pathway, the occurrence of this compound can be questioned: is it really present as such in the pigments or is it the result of the degradation of ommochromes during the extraction process in acidic medium?

Beside these compounds abundantly described in this manuscript, another compound, attributed to an analogue of psoralen, was particularly concentrated in E-ASM^{POS} (**Fig. 75**). The presence of this compound is very surprising. Usually naturally found in terrestrial plants, psoralen is used in UVA treatments as a photosensitizer and is extremely toxic to fish. This compound was used in solar creams until 1996³⁷³. A possible bioaccumulation in the shell from the aquatic environment or from oyster farmers has to be considered. Since its presence is completely unexpected, an unambiguous identification of this compound is presently under investigation by comparative RPLC-HRMS analysis using a psoralen commercial standard.

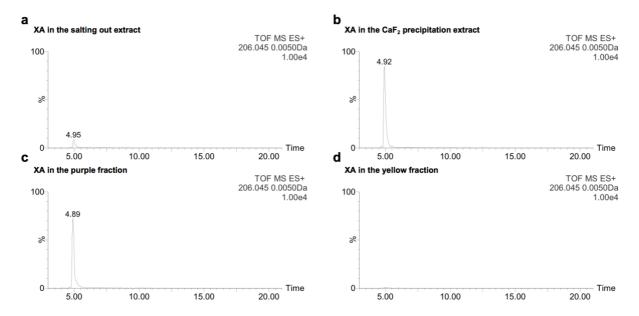


Fig. 74 Chromatograms of extracted xanthurenic acid ion normalised at an intensity of 10000. (a) Extracted xanthurenic acid ion in E-ASM^{POS}. (b) Extracted xanthurenic acid ion in P-ASM^{POS}. (c-d) Extracted xanthurenic acid ion in PF^{POS} and YF^{POS}, respectively.

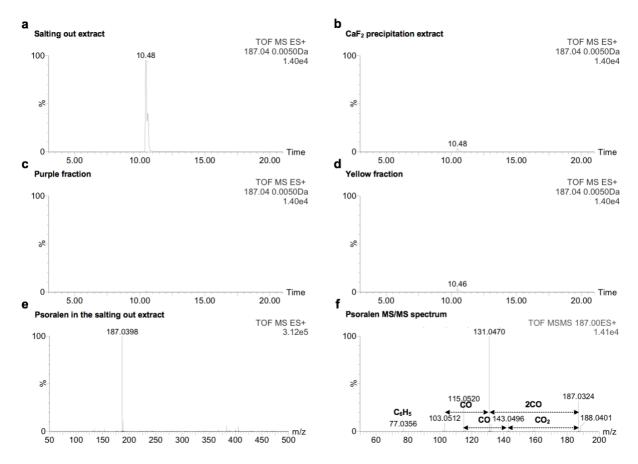


Fig. 75 Identification of psoralen-like compounds in the extracts obtained from the stock solution of **ASM**^{POS}. (a-d) Chromatograms of extracted psoralen-like ions normalised at an intensity of 14000. (e-f) Psoralen-like mass spectrum identified in E-ASM^{POS} with the corresponding MS/MS spectrum, respectively.

IV.3.2.1. Origin of ethylene glycol-based polymers

Ethylene glycol-based polymers are identified in samples obtained by the three methods, which is also completely unexpected. The successive increment of C₂H₄O units corresponds to the typical signature of a PEG standard in mass spectrometry. The [M+H]⁺ at m/z 327.2019 hypothesised as the molecular ion of PEG 326 in PF has a comparable fragmentation pattern by MS/MS (**Fig. 76a-b**) to that of a commercial PEG 400 (**Fig. 76c-d**).

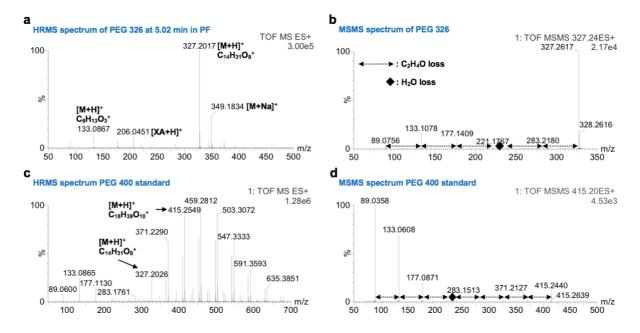


Fig. 76 Identification of ethylene glycol-based polymers. (**a-b**) PEG 326 identified in PF^{POS} and its fragmentation by MS/MS. The shift observed between the m/z of the molecular ion from PF and the fragmented parent ion (327.2017 and 327.2617, respectively) is due to a default of calibration. (**c-d**) PEG 400 standard analysed by MS (direct injection) and MS/MS.

The presence of a PEG-based polymer, besides any endogenous or exogenous origin, was first considered as a possible contamination during extraction. Indeed, when the separative elution was performed with commercial CaCO₃ (Sigma-Aldrich, European pharmacopeia quality, 98.5-100.5%) instead of oyster shells, the RPLC-HRMS analysis reveals the presence of these PEG-based polymers, confirming their origin. The occurrence of this polymer was further observed in all samples whatever the extraction method. All of them have in common the use of 1M HCl in water, therefore we first suspect it to be at the origin of the contamination (VWR Chemicals, 35-39%). After an examination of the BPI chromatogram of 1M HCl_(aq), PEG-based polymers were identified by extracted ion chromatograms (**Fig. 77**). The origin of this contamination will be further investigated with the use of HCl_(aq) from a different supplier or by substitution with AcOH.

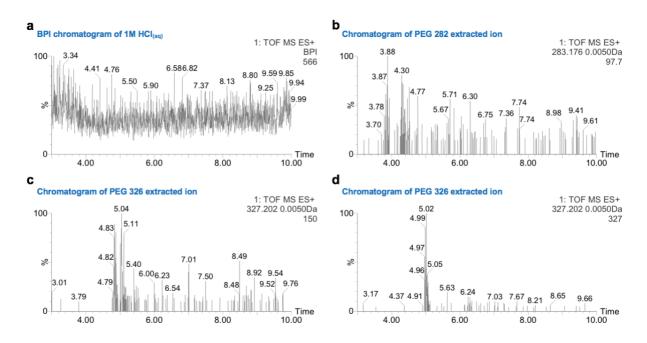


Fig. 77 Identification of PEGs in 1M HCl(aq). (a) BPI chromatogram. (b-c) Extracted chromatograms of PEG 282 and PEG 326 ions. (d) Extracted chromatogram of PEG 326 ions in ASM^{POS} concentrated under vacuum.

IV.4. CONCLUSION AND PERSPECTIVES

In this study, we question the effect of extraction methods on the recovered pigments. Starting with an initial sample of dissolved POS and JOS, three extraction methods were evaluated. Each lead to differences in composition and yields of pigments, although these differences are not tremendous, they can be significant to a certain point. Indeed, the salting-out method allows the extraction of ommochromes, whereas most of porphyrins are not extracted. The separative elution allows the extraction and separation of these two groups of pigments and the CaF₂ precipitation allows the extraction of both groups in a single operation.

Such methods are based on the physicochemical nature of all shell constituents, especially their solubility at different pH. Considering that it is not possible to predict the nature of the pigments trapped in the calcareous phase at solid state, we show how crucial it is to test different methods, especially in terms of pH, in order to collect and analyse all the types of pigments.

In addition, this study questions another central point: the chemical modification of pigments during the extraction process. So far, most of the studies never question it, assuming that the extracted, recovered and analysed mixture of pigments is the "true" one. Since no precise identification of the pigments is possible directly on the shell, no one can assume that the extraction process has no impact on the structure of pigments. Indeed, the conditions of extraction can lead to the degradation of labile compounds, for example by hydrolysis or demetallation. However, once a precise structure has been elucidated, the question of its stability in aqueous media, especially acidic or basic, must be asked. In a more general way, it shows how the identification of pigments can be conditioned by the extraction method.

Finally, we point out the effect of contamination by reagents used in the extractions process. This is generally well understood and considered by chemists and this type of bias can be easily detected. However, when working with natural substances where atomic percentages of some elements are below 1-2 wt.%, the identification of a contamination can be tricky. An alternative for the identification of pigment would be the analysis directly on the collected material and at solid state. For example, being quasi non-destructive, *in situ* laser desorption combined with mass spectrometry is a promising solution but requires in-depth development on solid shell samples.

CONCLUSION

The shell of the edible oyster *Crassostrea gigas* is a calcareous biomaterial suitable for a wide range of applications in health, depollution and materials synthesis. The processes for converting this material into a source of functional ingredients involve more or less complex operations, depending on the targeted application and the required level of performances. Indeed, simple operations such as grinding and sieving allow the preparation of a homogenous powder rich in calcium, while multiple advanced operations such as dissolution, decalcification and purification are required to access isolated compounds or families of compounds.

Based on the potential of oyster shells as a natural source of raw materials, this doctoral project was articulated around two strategies: i) the identification, characterisation and description of pigments contributing to the purple colour of the shell and ii) the development of selective extraction processes from the calcareous phase. Especially, methods to access to various collection of acid-soluble pigments from shells of juvenile oysters were detailed, identified to require less resources than fragments of shells of adult oysters, however with lower yields. A first group of tetrapyrrole pigments (uroporphyrin and derivatives) has been identified in the purple patterns of the shell and the mantle, probably deriving from the metabolism of haem, the respiratory pigment of many organisms. This work opens the way to many fundamental questions, such as their role in the mineralisation process, their association with the calcareous phase and their distribution and across species, as well as their conservation. The second group, attributed to ommochromes, constitutes the first instance of their occurrence in bivalves. On the basis of the identification of xanthurenic acid, the sketch of their structure has been proposed. A study allowing the identification of melanins in natural samples³⁰⁹ was reproduced on the acid-soluble pigments of the purple patterns of the shell of C. gigas. The absence of melanins oxidation products in the set of acid-soluble pigments provides additional elements

Conclusion

on the presence of ommochromes in purple patterns. This work is presently in the publication process.

An immediate and obvious perspective to this project would lie in the precise characterisation of the structure of the ommochromes described in Chapter III. It may also be relevant to evaluate the performance of the natural porphyrins described in Chapter II for targeted applications or by random screening. These perspectives could be accessible and feasible through upstream preparation. The reasonable production of a 10 gram batch of pigments would require the extraction of 25 kg of juvenile oyster shells, including a purification step by preparative chromatography.

EXPERIMENTAL PART

Experimental part

GENERAL EQUIPMENT

Centrifugation: Eppendorf centrifuge 5702.

Energy dispersive X-ray microanalysis: Sample was deposited on a support without

metallisation and the coloured surface was analysed with a field emission gun detector (Oxford

Instruments X-Max® SDD) coupled with a scanning electron microscope Zeiss EVO HD15

equipped with a secondary and backscattered electrons detector (resolution of 1.9 nm at 30 kV

under ultra-high vacuum).

Fluorescence spectroscopy: Excitation and emission spectra were recorded on a fluorescence

spectrometer (FS920, Edinburgh Instruments) equipped with a 450 W continuous xenon arc

lamp as the excitation source for steady-state photoluminescence measurements using quartz

cells with 10 mm excitation path length. Excitation spectra were recorded at an emission

wavelength of 656 nm (from 348 to 626 nm with a step of 0.1 nm, 26.7°C). Emission spectra

were recorded at an excitation wavelength of 405 nm (from 425 to 790 nm with a step of 0.1

nm, 26.8°C).

Freeze-drier: Labconco FreeZone 4,5 Plus.

Oven: Memmert 500.

pH meter: Crison PH 25.

RPLC-DAD-HRMS: separations were carried out using a 150 x 2.1 mm Kinetex 2.6 μm EVO

C18 100 Å reverse stationary phase, operating at 30°C with a constant flow rate of 0.5 mL/min

using ultrapure water (0.055 µS/cm) and acetonitrile HPLC grade as eluents both containing

0.1% formic acid. Analysis were conducted on a Waters Alliances UPLC Synapt G2-S system

equipped with an electrospray ionisation source. UV-vis spectra were recorded with a UPLC

LG 500 nm DAD detector from 200 to 500 nm with a resolution of 1.2 nm and a sampling rate

of 20 points/sec. Mass spectra were recorded in the m/z range of 50 to 3,000 with a ZQ

182

Experimental part

spectrometer fitted with Micromass Q-Tof spectrometer operating at capillary voltage of 3 kV

and cone voltage of 30 V, using phosphoric acid as an internal standard. MassLynx software

(version V4.1) was used for instrument control and data processing. Samples were kept at 10°C

in the autosampler. Appropriate blank analysis was performed before each sample (V_{ini}: 10 µL).

Blank TIC chromatogram was systematically subtracted to the corresponding sample TIC

chromatogram before data processing. Analysis were performed by the "Laboratoire de

Mesures Physiques" of Montpellier University.

Scales: Mettler Toledo XP504DR (scale range up to 520 g, resolution 0.1 mg, repeatability

0.04 to 0.1 mg). OHAUS AX423 (scale range up to 420 g, resolution 1 mg). Kern PLS (scale

range up to 1200 g, resolution 10 mg).

Scanning electron microscopy: Samples were deposited on supports and metallised with Pt

by Ar plasma-enhanced chemical vapour deposition (Quorum Technologies). Images were

recorded with a field emission scanning electron microscope HITACHI S4800 equipped with

a secondary and a backscattered electrons detector (accelerating voltage from 0.1 to 15 kV,

resolution of 1 nm at 15 kV, maximum magnification 800,000x).

Solid-state fluorescence: Samples were exposed, in the dark, to a UV LED monochromatic

light of 395-400 nm (10W, model CHX-FL-A-10W), and UV monochromatic lights of 254 and

366 nm (Minuvis DESAGA Heidelberg).

Sonification: Ney 300 Ultrasonik.

UV-vis absorption spectroscopy: Absorption spectra were recorded from 200 to 800 nm using

UV-1800 Shimadzu spectrophotometer (10 mm optical path length). Appropriate auto zero on

solvent blank was performed before each measurement.

Vortex stirrer: Heidolph Top Mix 94323 Bioblock Scientific

183

X-ray diffraction: Diffractograms were recorded on powdered shell samples ($< 40 \mu m$, 3 replicates from 3 different shells of adult *C. gigas*). The powder was placed on a glass slide and analysed in Q-Q-Bragg-Brentano geometry with Cu-K α radiation (Philips X'PERT-PRO, start position 10.017°2Th., end position 99.975°2Th., step size 0.033°2Th, scan speed 80.01 s, scan type continuous, generator setting 30 mA, 40 kV).

SOLVENTS AND REAGENTS

Sigma-Aldrich (USA).

Acetic acid glacial was purchased from Carlo Erba Reagents (France).

Acetonitrile HPLC gradient grade (≥ 99.9%) was purchased from Fisher Scientific (Belgium).

C18 grafted silica for flash high throughput purification was purchased from Supelco (USA, batch SP98226 and SP10816).

Calcium carbonate European pharmacopeia quality (98.5-100.5%) was purchased from

Fontainebleau sand was purchased from VWR Chemicals (Belgium).

Formic acid ULC/MS grade (99%) was purchased from Biosolve (Netherlands).

Hydrochloric acid 37% was purchased from VWR Chemicals (France).

Hydrofluoric acid 38-40% (27.6 M, was purchased from VWR Chemicals (France).

Polyethylene glycol 400 (level quality 200) was purchased from Sigma-Aldrich (USA).

Sodium hydroxide 98% was purchased from VWR Chemicals (Belgium).

Sodium hypochlorite 9.6% was purchased from Notilia.

Sepia officinalis eumelanin black powder was purchased from Sigma-Aldrich (USA, batch #103H1023) and stored at -21°C before use.

Trifluoroacetic acid HPLC grade was purchased from Fisher Scientific (United Kingdom).

Ultrapure water (0.055 μS/cm) were obtained by pre-filtration and reverse osmosis system (LaboStar® PRO TWF, Evoqua Water Technologies).

Uroporphyrin I dihydrochloride was purchased from Santa Cruz Biotechnology (USA, batch H1219) and stored at -21°C before use.

Xanthurenic acid was purchased from Interchim (France, batch V0226P002).

SHELL SAMPLES

Shell fragments: Approximately 1 kg of shell fragments were collected by hand on living adult oysters in August 2017 (Thau lagoon, Marseillan, France, GPS coordinates: 43.382127, 3.555193). Shell fragments were rinsed with tap water at the farm and transported to the laboratory. Shell fragments were extensively rinsed with tap water suspended in 0.0155M NaOCl_(aq) with sonification and regular manual stirring (1:10 wt./V, 120 min). Shell fragments were rinsed several times and suspended in demineralised water with sonification and regular manual stirring (1:10 wt./V, 120 min). Shell fragments were rinsed several times with demineralised water and dried in oven (overnight, 40°C). Shell fragments were sorted in three classes according to their colour, namely white (WOS), intermediate (ROS) and fully purple (POS). Samples were stored in the dark at 25°C before use.

Adductor muscle scar: Thirteen waste valves of adult *C. gigas* with dark AMS were supplied by Tarbouriech-Médithau. Valves were decontaminated. After decontamination, adductor muscle scars were prepared with cutting pliers and the outer shell layers were removed using a Dremel 3,000 polisher.

Shells of juvenile oysters: JOS were supplied by Tarbouriech-Médithau. JOS were immersed in water bath at 70°C to remove the organic materials. Water was regenerated each 2h during 8h before decontamination.

CHAPTER II

Preparation of ASM^{POS}: Approximately 10 g of POS were dissolved in 1M HCl_(aq) under magnetic stirring (1:20 wt./V, 30 min, 700 RPM). The ASM^{POS} was obtained after filtration on a glass sintered filter (POR 4) filled with Fontainebleau sand. The ASM^{POS} was kept in the dark at -21°C. Dissolution of 500 mg of POS, milled in a mortar, was reproduced with in 1M AcOH_(aq) (1:20 wt./V, 120 min, 700 RPM).

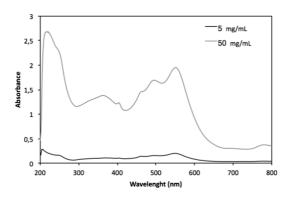


Fig. 78 Absorption spectra of ASM^{POS}.

Preparation of ASM^{WOS}: Approximately 30 g of WOS were dissolved in 1M HCl_(aq) under magnetic stirring (1:20 wt./V, 30 min, 700 RPM). The ASM^{WOS} was obtained after filtration on a glass sintered filter (POR 4) filled with Fontainebleau sand. The ASM^{WOS} was kept in the dark at -21°C.

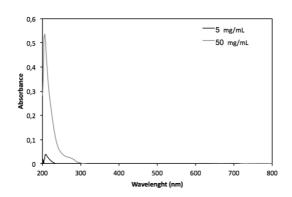


Fig. 79 Absorption spectra of ASM^{WOS}.

Preparation of ASM^{AMS}: Approximately 97 g of AMS were dissolved in 1M HCl_(aq) under magnetic stirring (1:20 wt./V, 30 min, 500 RPM). The ASM^{AMS} was obtained after filtration on a glass sintered filter (POR 4) filled with Fontainebleau sand. The ASM^{AMS} was kept in the dark at -21°C.

Fluorescence spectroscopy: Analysis were conducted after dilution by a factor 10 of 1 mL of ASM^{POS} in 1M HCl_(aq).

UV-vis absorption spectroscopy: Analysis were conducted after dilution by a factor 10 of 1 mL of ASM^{POS} in 1M HCl_(aq). ASM^{WOS} and ASM^{AMS} were analysed without dilution.

Composition profile by RPLC-DAD-HRMS: The ASM^{POS} (2 mL) was filtered on a polyethersulfone syringe filter (0.22 μ m) and analysed on the RPLC-DAD-HRMS system (ESI+) described in the equipment section with V_{inj}: 10 μ L. Separation was performed with a gradient system acidified with 0.1% formic acid: 0 to 50% acetonitrile in 20 min, followed by 50 to 100% acetonitrile in 5 min, followed by 100% acetonitrile in 1 min, followed by 100% ultrapure water in 0.1 min and finally 4.9 min with 100% ultrapure water (**method #1**).

Identification of uroporphyrin in ASM^{POS}. The previous filtered ASM^{POS}, ASM^{WOS} (2 mL filtered on a polyethersulfone syringe filter 0.22 μm) and 0.5 mg of uroporphyrin chemical standard dissolved in 500 μl were analysed on the RPLC-DAD-HRMS system (ESI+) described in the equipment section with V_{inj}: 10 μL. Separation were performed with a gradient system acidified with 0.1% formic acid: 0 to 20% acetonitrile in 3 min followed by an isocratic elution with 20% acetonitrile for 17 min, followed by 20 to 50% acetonitrile in 12 min, followed by 50 to 100% ultrapure water in 0.1 min, followed by 100% ultrapure water in 4.9 min (method #2). Identification of uroporphyrin in dark AMS. Approximately 200 mL of ASM^{AMS} was evaporated to reduce the volume to approximately 125 mL (16 mbar, 35°C). A slight excess volume of 27.6M HF_(aq) was added. After 30 min under gentle stirring, the sample was

centrifuged (20 min, 4,400 RPM). The supernatant was then concentrated to dryness (atmospheric pressure for 7 days at 25°C in the dark followed by vacuum evaporation at 35°C). The solid residue was suspended in ultrapure water (40 mL, 0.055 μ S/cm), stirred with a vortex stirrer and centrifuged (20 min, 4,400 RPM). The solid material resulting from centrifugation was washed a second time with ultrapure water (15 mL, 0.055 μ S/cm) and freeze-dried (0.4 mg, extraction yield of 0.004 %). The solid powder was dissolved in 40 μ L of 1M HCl_(aq) and analysed by RPLC-UV-vis-HRMS (ESI+) according to **method #2**.

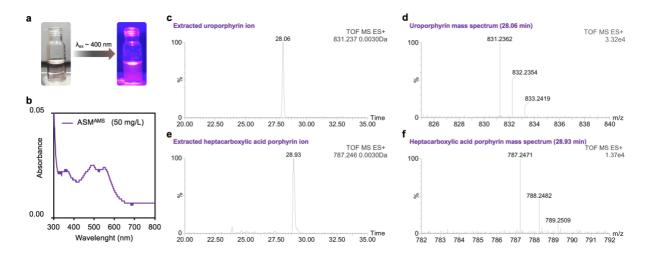


Fig. 80 Identification of porphyrins in ASM^{AMS}. (a) Photoluminescence of ASM^{AMS} at $\lambda_{ex} \sim 400$ nm. (b) UV-vis absorption spectrum of ASM^{AMS}. (c-f) Identification of porphyrins by RPLC-HRMS.

Chemical confirmation of uroporphyrin and derivatives in ASM^{POS}. Decalcification of approximately 190 mL of ASM^{POS} was conducted by the formation of CaF₂ with the addition of 27.6M HF_(aq) (same method as dark AMS). The solid powder (19 mg, extraction yield of 0.19 %) was dissolved in 1900 μL of 1M HCl_(aq) and analysed by RPLC-DAD-HRMS (ESI+) according to **method #2**. MS/MS experiments were performed in collision-induced dissociation mode with a trap collision energy ramp from 40 to 100 eV and using auto transfer collision energy of 2 eV. Argon was used as the collision gas.

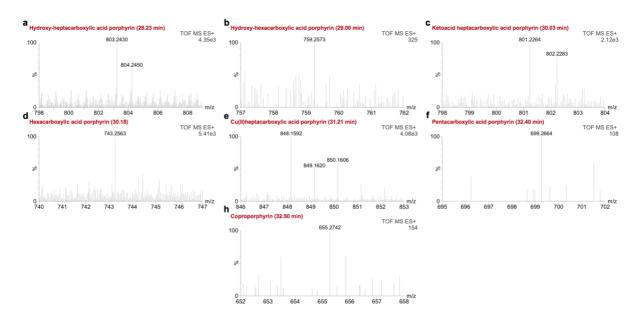


Fig. 81 Mass spectra of the set of minor porphyrins identified in concentrated ASMPOS.

NMR experiments. Approximately 100 g of JOS were dissolved in 1M HCl_(aq) under magnetic stirring (1:20 wt./V, 30 min, 500 RPM). The ASM^{JOS} was obtained after filtration on a glass sintered filter (POR 4) filled with Fontainebleau sand. Immediately after filtration, ASM^{JOS} was deposited on a C18 grafted silica gel previously equilibrated with 1M HCl_(aq). After deposition, decalcification was performed with 200 mL of 1M HCl_(aq) followed by 200 mL of 0.1% TFA. Separative elution was performed with multiple eluents acidified with 0.1% TFA:

- F1: ultrapure water/acetonitrile (95:5 V/V) 400 mL
- F2: ultrapure water/acetonitrile (90:10 V/V) 250 mL
- F3: ultrapure water/acetonitrile (85:15 V/V) 250 mL
- F4: ultrapure water/acetonitrile (80:20 V/V) 150 mL
- F5: acetonitrile 350 mL

Fractions were collected and freeze-dried. This process was repeated once. The fluorescent fraction (F5, \sim 9 mg) was solubilised in \sim 30 mL of 1M HCl_(aq). Separation and isolation of porphyrins was carried out on a semi-preparative UHPLC-DAD system in the UV-vis range of

200-800 nm (Thermo Scientific Dionex Ultimate 3000). Separation was performed using a 250 x 10 mm Kinetex 5 μm EVO C18 100 Å reverse stationary phase, operating at 25°C with a constant flow rate of 2.0 mL/min. Isolation was performed using four gradients, followed by an isocratic elution and a final gradient system of ultrapure water (0.055 μS/cm) and acetonitrile containing 0.1% formic acid (0 to 27% acetonitrile in 3.5 min followed by 27 to 35% acetonitrile in 14.5 min, followed by 35 to 50% acetonitrile in 1 min, followed by 50 to 80% acetonitrile in 2 min; isocratic elution was conducted with 80% acetonitrile in 1 min, followed by 80 to 100% acetonitrile in 5 min, followed by 100% ultrapure water in 1 min and 100% ultrapure water for 27 min). Peaks at 19.15, 23.32 and 24.72 were collected. 57 runs were required with V_{inj} : 500 μL. Sample was kept at 20°C in the autosampler. Fractions containing uroporphyrin were pooled together and freeze-dried. The isolated uroporphyrin was dissolved in 600 μL of DMSO-d6 and d H spectrum was recorded from -5 to +13 ppm (64 scans, Bruker Avance III HD 400 MHz). The 1H spectrum of uroporphyrin standard (2 mg in 600 μL DMSO-d6) was recorded in the same conditions.

Identification of uroporphyrin in the shell forming tissue. Mantle tissues (MEE) were collected from ten 10 adult *C. gigas* resulting from the daily determination of flesh content, performed by Tarbouriech-Médithau, in accordance with the inter-branch agreements on oyster packaging. Tissues were placed in glass bottles and kept in the dark at -18°C and transported to the laboratory. Samples were carefully rinsed with deionised water, freeze-dried and stored in the dark at -21°C before investigation. MEE were freeze-dried, crushed in a mortar and suspended in 1M HCl_(aq) under magnetic stirring (1 g, 1:20 wt./V, 60 min, 700 RPM). The ASM^{MEE} was obtained after filtration on a glass sintered filter (POR 4) filled with Fontainebleau sand. The identification of uroporphyrin was achieved using the RPLC-DAD-HRMS **method** #2.

Identification of chlorophyll catabolites in viscera. Viscera were collected from the previous *C. gigas* sample. After freeze-drying, viscera were crushed in a mortar and suspended in 1M $HCl_{(aq)}$ under magnetic stirring (1 g, 1:20 wt./V, 60 min, 700 RPM). The ASM^{VOT} was obtained after filtration on a glass sintered filter (POR 4) filled with Fontainebleau sand. The identification of uroporphyrin was achieved using the RPLC-DAD-HRMS **method #2**.

CHAPTER III

Separation monitored by UV-vis absorption. The ASM^{POS} previously prepared in Chapter II was separated with the UHPLC-DAD system employed for the purification of uroporphyrin in Chapter II. Separation was performed using a 100 x 4.6 mm Kinetex 5 μ m EVO C18 100 Å reverse stationary phase, operating at 30°C with a constant flow rate of 1.0 mL/min. Separation was performed using two gradients system of ultrapure water (0.055 μ S/cm) and acetonitrile containing 0.1% formic acid (0 to 50% acetonitrile in 53 min followed by 50 to 100% acetonitrile in 12 min, followed 100% acetonitrile in 2 min, followed by 100% ultrapure water in 0.5 min; followed by 100% water in 9.5 min). V_{inj} : 80 μ L. Sample was kept at 20°C in the autosampler.

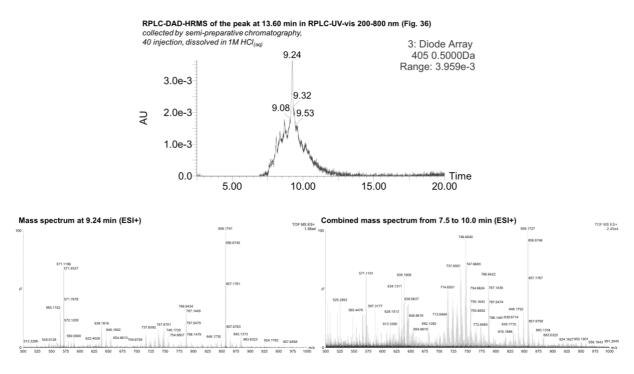


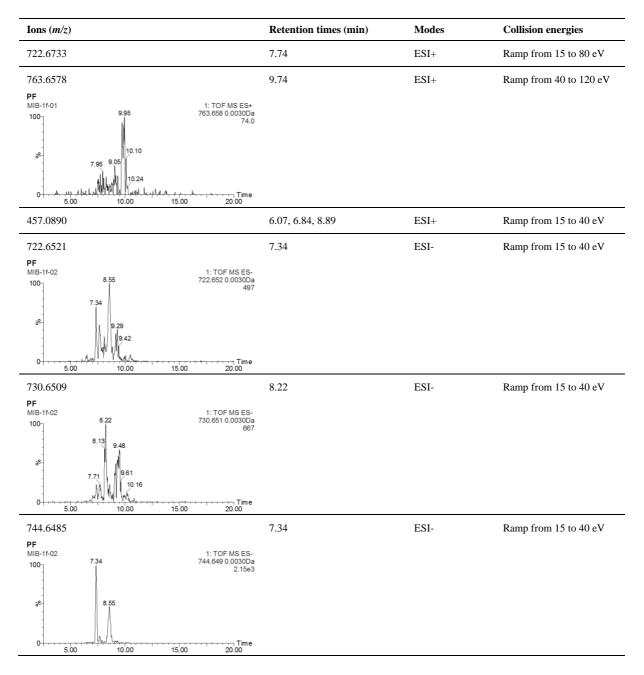
Fig. 82 RPLC-DAD-HRMS analysis of the compound eluted at 13.60 min in Fig. 36

Screening of metabolic products and identification of xanthurenic acid. A solution of 10 mg/mL of xanthurenic acid was prepared by solubilisation in 1 mL of 1M HCl_(aq) under magnetic stirring (60 min, 700 RPM), followed by filtration on polyethersulfone syringe filter (0.22 μm), XA being slightly soluble in water. The resulting solution was analysed by RPLC-DAD-HRMS according to **method #1** employed in Chapter II. A stock solution of ASM^{POS} was prepared by dissolution of approximately 1 g of POS in 1M HCl_(aq) under magnetic stirring (1:20 wt./V, 30 min, 700 RPM) and filtration on a glass sintered filter (POR 4) filled with Fontainebleau sand. The ASM^{POS} stock solution was kept in the dark at -21°C until RPLC-DAD-HRMS (ESI+) according to **method #1**. MS/MS experiments were performed in collision-induced dissociation mode with a trap collision energy ramp from 15 to 40 eV and using auto transfer collision energy of 2 eV. Argon was used as the collision gas.

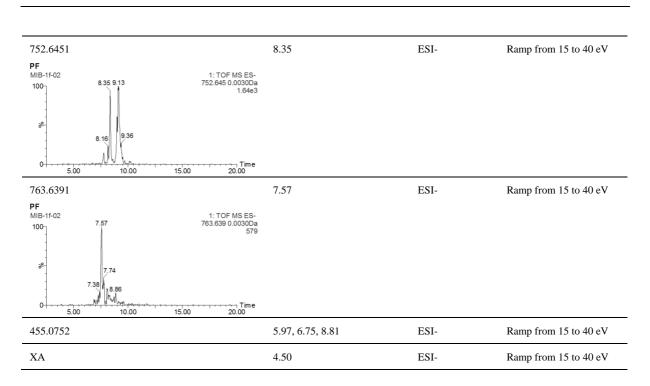
A solution of ASM^{POS} + XA standard (50:50 V/V) was prepared after dilution of the XA solution by a factor 865 in 1M HCl(aq) (11.56 μ L of the initial solution in 9.9884 mL of 1M HCl(aq)). The diluted XA solution, ASM^{POS} and ASM^{POS} + XA standard were analysed by RPLC-DAD-HRMS according to **method #1**.

Preparation of a sample concentrated in pigments. The ASM^{POS} stock solution (40 mL) was deposited on a C18 grafted silica gel (approximately 40 g) previously equilibrated with 1M HCl_(aq). After deposition, decalcification was performed with 80 mL 1M HCl_(aq) followed by 80 mL 0.1% TFA. Separative elution was performed with 420 mL of ultrapure water/acetonitrile (80:20 V/V + 0.1% TFA). The resulting purple fraction was freeze-dried. Separation was followed with 140 mL acetonitrile + 0.1% TFA. The resulting photoluminescent fraction (yellow fraction) was freeze-dried. The purple fraction (1 mg) was solubilised in 200 μ L of 1M HCl_(aq) and analysed by RPLC-DAD-HRMS according to **method #1**.

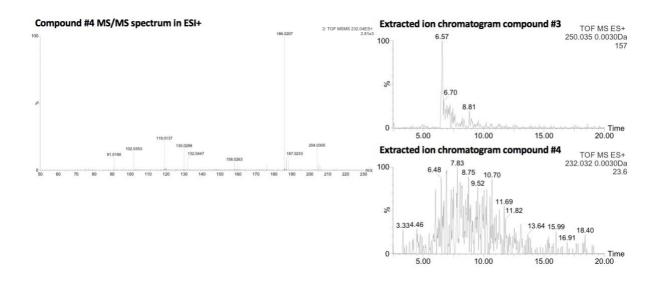
Tandem mass spectrometry. MS/MS experiments were conducted using auto transfer collision energy of 2 eV. Argon was used as the collision gas. Collision-induced dissociation mode was performed according to:

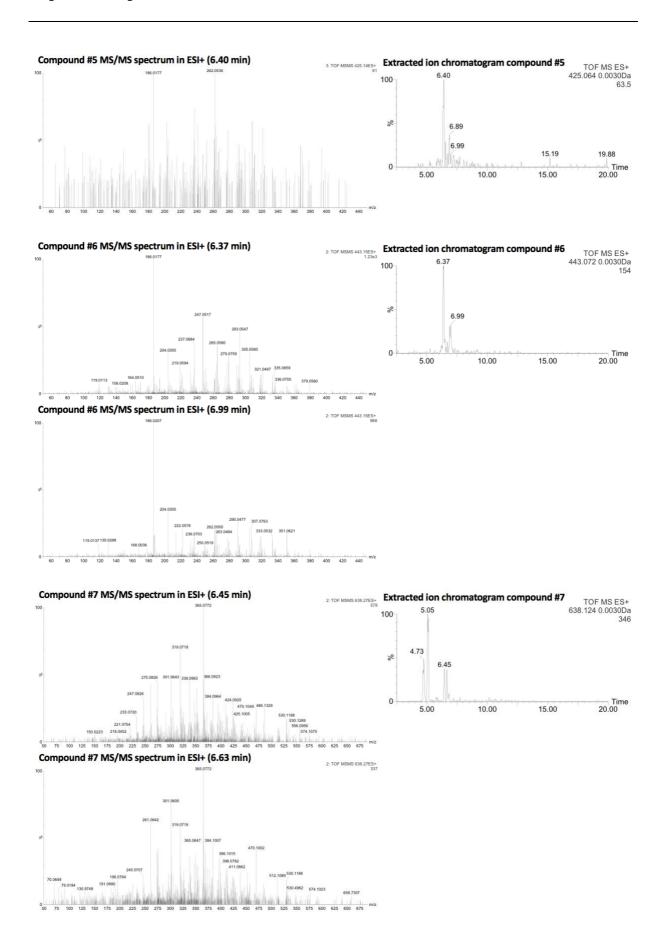


Experimental part



Automatic MS/MS experiments. MS/MS start 50 Da end 1500 Da, number of compound 3x4, MS/MS switch after 2 sec, MS/MS scan time 0.1 sec. Peak detection: used intensity based peak detection, peak detection window, charge state tolerance: 0.2 Trap MS/MS collision energy ramp from 30 to 50 eV. Cone voltage 40V. Collision energy ramp low mass 50 Da, high mass 1500 Da, ramp low mass 10-20 eV ramp high mass 80-140 eV.





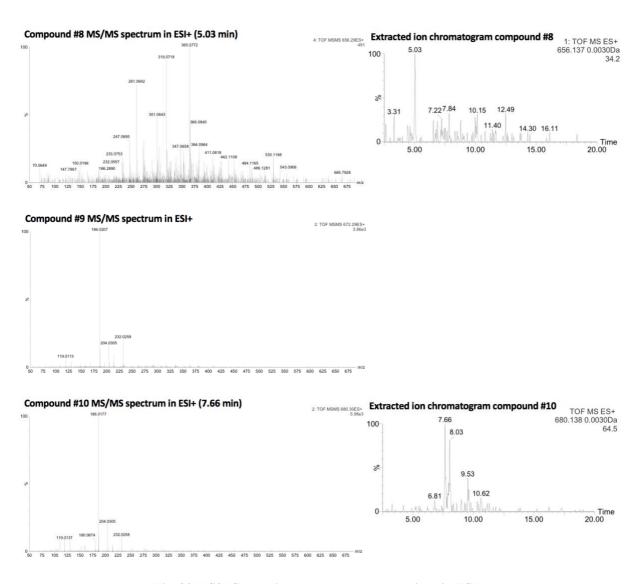


Fig. 83 MS/MS experiments on monocharged ions in ESI+.

Photo-catalysed degradation. A stock solution of ASM^{JOS} was prepared with approximately 10 g of JOS dissolved in 1M HCl_(aq) under magnetic stirring (1:20 wt./V, 30 min, 500 RPM). The ASM^{JOS} was obtained after filtration on a glass sintered filter (POR 4) filled with Fontainebleau sand. The ASM^{JOS} was kept in the dark at -21°C. Three samples of ASM^{JOS} (3 mL each) were exposed to sunlight, three supplemental samples (3 mL each) were kept in the dark at -18°C and three supplemental samples (3 mL each) were kept in the dark at 25°C. After 62 days of sunlight exposition, the ASM^{JOS} was visually discoloured. This degradation was confirmed by the progressive decrease of the characteristic absorption bands at 491 and 548 nm

that completely disappeared after 300 days of exposure (**Fig. 84c**). On the other hand, the ASM^{JOS} kept in the dark at 25°C was rather coloured after 367 days with only half the absorbance in the 430-600 nm range. The ASM^{JOS} kept in the dark at -18°C was visually not discoloured but a low decrease of absorption bands at 491 and 548 was observed, a degradation upon analysis is a possibility, as-well-as a degradation not catalysed by light exposition. At day 367, samples were compared by RPLC-HRMS. The signals of clusters of di-charged ions from 8 to 10 min, were quasi disappeared from the sample exposed to sunlight, whereas they were identified in the samples kept in the dark at 25°C and -18°C (the ionic intensity being higher in the sample kept at -18°C, **Fig. 84a-b**).

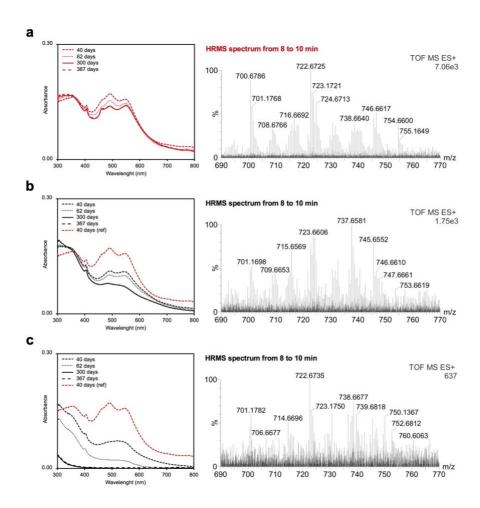


Fig. 84 Photo-catalysed degradation of ASM^{JOS} monitored by UV-vis spectroscopy and RPLC-HRMS. (a)

Reference sample kept at -18°C. (b) Sample kept at 25°C in the dark. (c) Sample exposed to sunlight.

Sepia officinalis eumelanin. 1.2 mg of eumelanin was suspended in 120 μ L of 1M NaOH(aq) stirred for 10 min, sonification for 20 min and centrifuged for 20 min at 4400 RPM. In these conditions, eumelanin was very slightly soluble. The yellow-brownish supernatant was collected in analysed by the RPLC-DAD-HRMS (ESI+) method #1 (V_{inj} : 10 μ L).

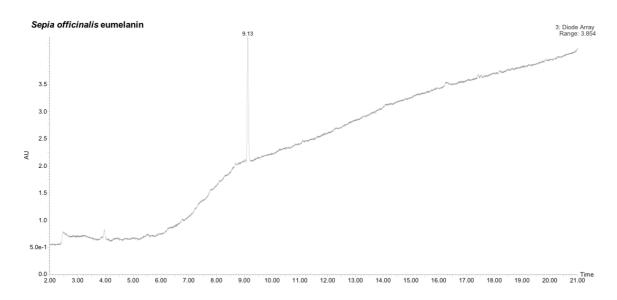


Fig. 85 UV-vis chromatogram of Sepia officinalis eumelanin.

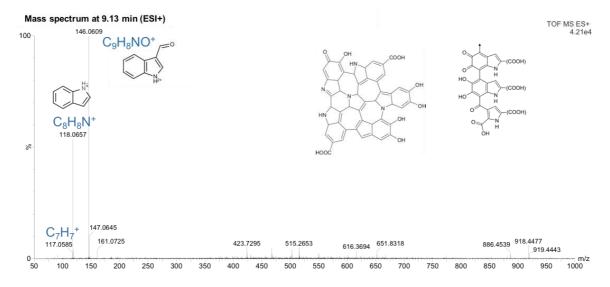


Fig. 86 Mass spectrum at 9.13 min.

NMR experiments. The fractions F1 to F4 obtained in Chapter II were pooled together and freeze-dried. The resulting powder (~ 80 mg) was suspended in EtOH_{abs} (~ 100 mL) with a vortex stirrer for 10 min and centrifuged for 20 min at 4400 RPM. This operation was repeated once on the solid residue after centrifugation. The solid residue was collected and suspended in a minimum volume of ultrapure water and freeze-dried. The resulting powder (~ 70 mg) was suspended in 10 mL ultrapure water with a vortex stirrer for 10 min, and centrifuged for 20 min at 4400 RPM. The supernatant was finally freeze dried. After freeze drying, the powder (~ 60 mg) was stored in the dark at -21°C until NMR experiments (solid ¹³CNMR was conducted on a Varian VNMRS 400MHz spectrometer with approximately 31 mg, and liquid experiments were conducted on a Bruker Avance III 600 MHz spectrometer with 2.2 mg in 600 μ L of DMSO-d6).

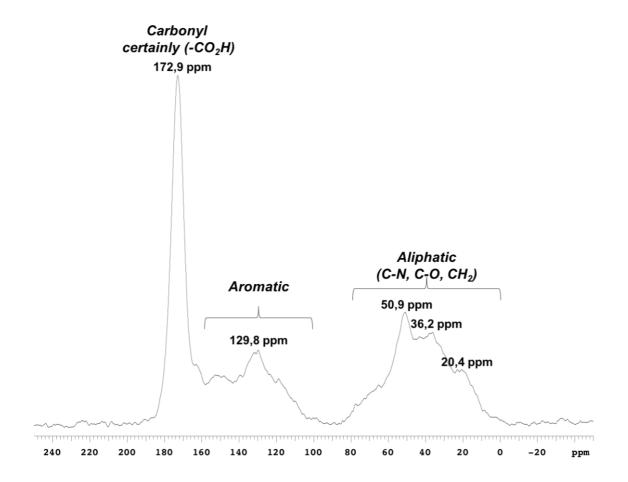


Fig. 87 ¹³**CNMR obtained in pulse sequence mode.** Rotor: zirconium oxide, rotation: 12000 Hz, mode cross polarisation. Spectrometer: Varian VNMRS 400MHz.

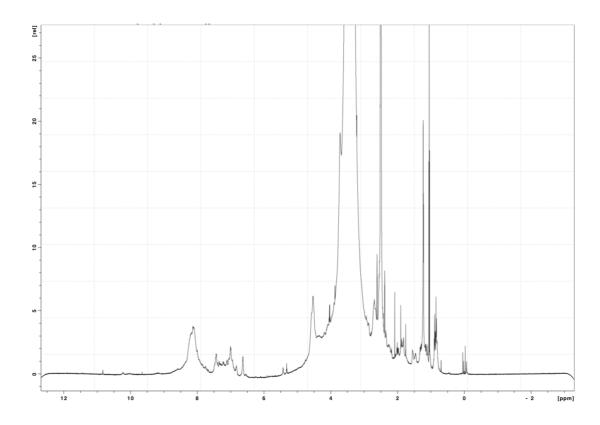


Fig. 88 ¹HNMR (64 scans, TD 2048x256).

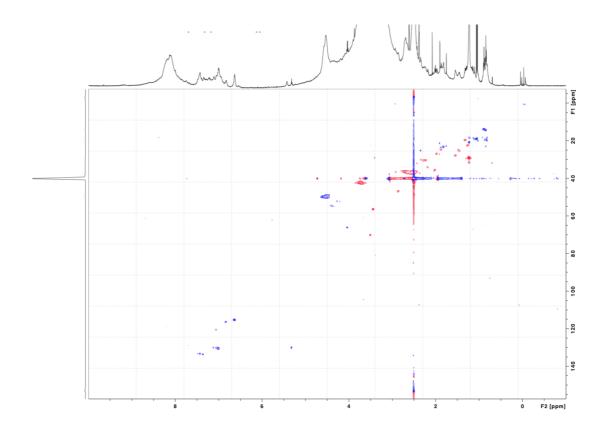


Fig. 89 HSQC 13 C- 1 H (32 scans, TD 2048x256, SW(13 C): 24900 Hz, SW(1 H): 6600 Hz.

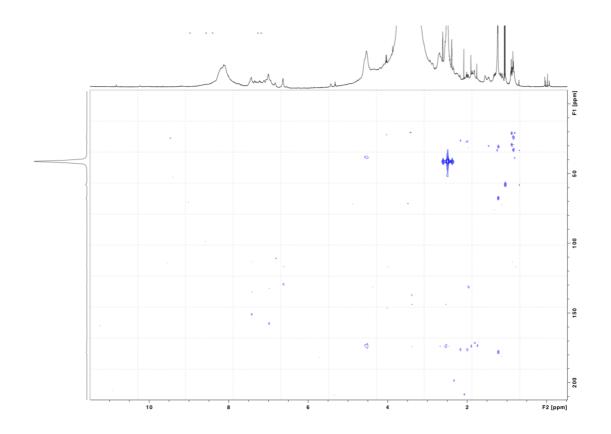


Fig. 90 HMQC 13 C- 1 H (92 scans, TD 2048x256, SW(13 C): 33525 Hz, SW(1 H): 7200 Hz.

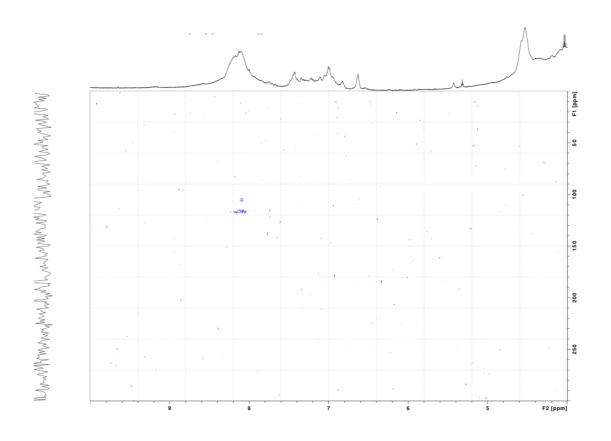


Fig. 91 HSQC ¹⁵N-¹H (64 scans, TD 2048x256, SW(¹⁵N): 18250 Hz, SW(¹H): 3600 Hz.

Dialysis of ASM^{POS}. The dialysis of PF (0.1mg/mL in 1M HCl_(aq)) was performed at three molecular weight cut-offs (0.5, 2 and 8 kDa MWCO) againt ultrapure water, but in this conditions, no evident transfer of colour to the dialysis solution was observed. After dialysis, the cellulose ester membrane was fully purple-coloured, suggesting the adsorption of pigments (**Fig. 92**).

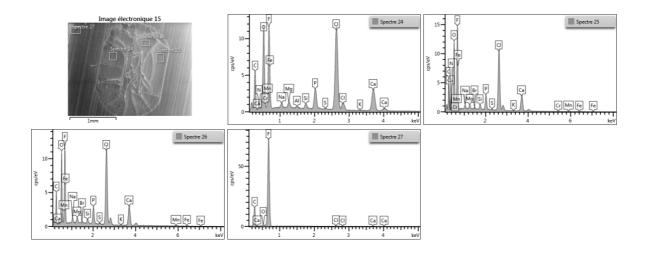


Fig. 92 Dialysis of PF at 8kDa molecular weight cut-off.

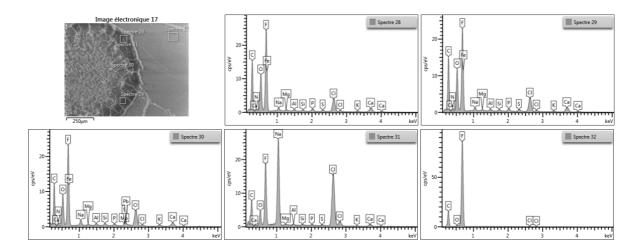
CHAPTER IV

Preparation of the ASM^{POS} **stock solution.** The ASM^{POS} stock solution was prepared by dissolution of 7 g of POS in 140 mL of 1M HCl_(aq) (1:20 wt./V, 30 min, 700 RPM). The ASM^{POS} stock solution was obtained after filtration on a glass sintered filter (POR 4) filled with Fontainebleau sand. The ASM^{POS} stock solution was kept in the dark at -21°C. 5 mL of the ASM^{POS} stock solution was concentrated under vacuum at 30°C until precipitation of calcium salt. Sample was filtered on cotton wool and analysed. RPLC-DAD-HRMS (ESI+) analysis was conducted according to **method #1**.

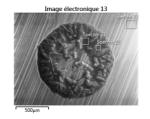
Salting out. 40 mL of ASM^{POS} stock solution was basified until pH 10.36 by repeated addition of 100 μ L of 1M NaOH(aq) until pH 5.40 and 10 μ L until pH 10.36. Centrifugation was conducted for 20 min at 4400 RPM. The solid residue was suspended in ultrapure water and freeze-dried. The solid powder was suspended in 8 mL of ultrapure water, stirred, centrifuged and the resulting solid residue was freeze-dried (E-ASM^{POS}). 1.0 mg of E-ASM^{POS} was dissolved in 200 μ L of 1M HCl_(aq) and analysed by RPLC-DAD-HRMS (ESI+) using **method** #1. E-ASM^{POS} was also analysed by EDX by deposition of 10 μ L on Teflon. In this condition the accuracy of the measure is \pm 10 % of the at.% value. The CF₄ blank content of Teflon was removed during post treatment data.

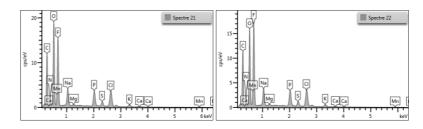


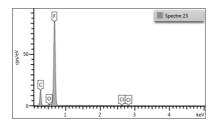
Separative elution. This method was conducted in Chapter III: preparation of a sample concentrated in pigments. The PF was also analysed by EDX by deposition of $10\mu L$ on Teflon. In this condition the accuracy of the measure is \pm 10 % of the at.% value. The CF₄ blank content of Teflon was removed during post treatment data.



CaF₂ precipitation. 40 mL of ASM^{POS} stock solution was concentrated under vacuum, kept at 25°C , until the precipitation of calcium salts. After filtration on cotton wool, 27.6M HF(aq) was added dropwise in slight excess. Centrifugation was conducted for 3 min. at 4400 RPM. The supernatant was collected and evaporated at 30°C. The solid residue was suspended in 10 mL of ultrapure water. After centrifugation, the solid residue was freeze-dried (P-ASM^{POS}). 1.0 mg of P-ASM^{POS} was dissolved in 200 μL of 1M HCl_(aq) and analysed by RPLC-DAD-HRMS (ESI+) using **method #1**. P-ASM^{POS} was also analysed by EDX by deposition of 10 μL on Teflon. In this condition the accuracy of the measure is \pm 10 % of the at.% value. The CF₄ blank content of Teflon was removed during post treatment data.







REFERENCES

- Tarbouriech, F. & Thibaut, J.-J. Procédé d'ostréiculture amélioré, FR3019967, WO205159025A1 (2015).
- 2. Williams, S. T. Molluscan shell colour. *Biol. Rev.* **92**, 1039–1058 (2017).
- 3. Solano, F. Melanins: skin pigments and much more types, structural models, biological functions, and formation routes. *New J. Sci.* **2014**, 1–28 (2014).
- 4. Yao, Z., Xia, M., Li, H., Chen, T., Ye, Y. & Zheng, H. Bivalve shell: not an abundant useless waste but a functional and versatile biomaterial. *Crit. Rev. Environ. Sci. Technol.*44, 2502–2530 (2014).
- 5. Morris, J. P., Backeljau, T. & Chapelle, G. Shells from aquaculture: a valuable biomaterial, not a nuisance waste product. *Rev. Aquac.* **11**, 42–57 (2019).
- 6. Chellam, A., Victor, A. C. C., Dharmaraj, S., Velayudhan, T. S. & Rao, K. S. Pearl oyster farming and pearl culture. *FAO Corp. Doc. Repos.* (1991).
- 7. Nagai, K. A history of the cultured pearl industry. *Zoolog. Sci.* **30**, 783–793 (2013).
- 8. Campbell, M. D. & Hall, S. G. Hydrodynamic effects on oyster aquaculture systems: a review. *Rev. Aquac.* (2018).
- 9. Márquez-Aliaga, A., Jiménez-Jiménez, A. P., Checa, A. G. & Hagdorn, H. Early oysters and their supposed Permian ancestors. *Palaeogeogr. Palaeoclimatol. Palaeoecol.* **229**, 127–136 (2005).
- Checa, A. G., Jiménez-Jiménez, A. P., Márquez-Aliaga, A. & Hagdorn, H. Further comments on the origin of oysters. *Palaeogeogr. Palaeoclimatol. Palaeoecol.* 240, 672–674 (2006).
- 11. Hautmann, M. Shell morphology and phylogenetic origin of oysters. *Palaeogeogr. Palaeoclimatol. Palaeoecol.* **240**, 668–671 (2006).

- 12. Wrenn, E. The 100-million-year-old oyster, ten times normal size, which will undergo MRI scan to see if it contains the world's biggest pearl. *MailOnline* (2012).
- Mouchi, V., Lartaud, F., Guichard, N., Immel, F., Rafélis, M. de, Broussard, C., Crowley,
 Q. G. & Marin, F. Chalky versus foliated: a discriminant immunogold labelling of shell
 microstructures in the edible oyster *Crassostrea gigas*. *Mar. Biol.* 163, 256 (2016).
- 14. Walter, R. C., Buffler, R. T., Bruggemann, J. H., Guillaume, M. M. M., Berhe, S. M., Negassi, B., Libsekal, Y., Cheng, H., Edwards, R. L., von Cosel, R., Néraudeau, D. & Gagnon, M. Early human occupation of the Red Sea coast of Eritrea during the last interglacial. *Nature* 405, 65–69 (2000).
- 15. Salvi, D. & Mariottini, P. Molecular taxonomy in 2D: a novel ITS2 rRNA sequence-structure approach guides the description of the oysters' subfamily Saccostreinae and the genus *Magallana* (Bivalvia: Ostreidae). *Zool. J. Linn. Soc.* **179**, 263–276 (2017).
- 16. Cochennec-Laureau, N. Espèces d'huîtres perlières : *Pinctada margaritifera*, *P. maxima* et *P. fucata. Futura* (2017).
- 17. Nazar, A. K. A., Dharani, G., Rao, D. V., Santhanakumar, J. & Saravanane, N. New record of pearl fish *Onuxodon margaritiferae* (Rendahl, 1921) from Andaman Islands. *Indian J. Fish.* **58**, 141–143 (2011).
- 18. Lee, Y.-J., Kang, H. Y., Lee, W. C. & Kang, C.-K. Hydrodynamic effects on growth performance of the Pacific oyster *Crassostrea gigas* cultured in suspension in a temperate bay on the coast of Korea. *Estuaries Coasts* **40**, 1551–1565 (2017).
- 19. Botta, R., Asche, F., Borsum, J. S. & Camp, E. V. A review of global oyster aquaculture production and consumption. *Mar. Policy* **117**, 103952 (2020).

- 20. Wei, Y.-L., Kuo, P.-J., Yin, Y.-Z., Huang, Y.-T., Chung, T.-H. & Xie, X.-Q. Co-sintering oyster shell with hazardous steel fly ash and harbor sediment into construction materials. *Constr. Build. Mater.* **172**, 224–232 (2018).
- 21. Mohamed, M., Yusup, S. & Maitra, S. Decomposition study of calcium carbonate in cockle shell. *J. Eng. Sci. Technol.* **7**, 1–10 (2012).
- 22. Carter, J. G. et al. Illustrated glossary of the Bivalvia. Treatise Online 48, 1–209 (2012).
- 23. Ubukata, T. A theoretical morphologic analysis of bivalve ligaments. *Paleobiology* **29**, 369–380 (2003).
- Checa, A. G. & Jiménez-Jiménez, A. P. Rib fabrication in Ostreoidea and Plicatuloidea (Bivalvia, Pteriomorphia) and its evolutionary significance. *Zoomorphology* 122, 145–159 (2003).
- 25. Galtsoff, P. S. The American oyster *Crassostrea virginica* Gmelin. vol. 64 (United States Government Printing Office, 1964).
- 26. Wada, K. T. & Tëmkin, I. Taxonomy and phylogeny. in *The pearl oyster* (eds. Southgate, P. C. & Lucas, J. S.) 37–75 (Elsevier, 2008).
- 27. Carriker, M. R. & Palmer, R. E. A new mineralized layer in the hinge of the oyster. *Science* **206**, 691–693 (1979).
- 28. Lee, S. W., Kim, Y. M., Choi, H. S., Yang, J. M. & Choi, C. S. Primary structure of myostracal prism soluble protein (MPSP) in oyster shell, *Crassostrea gigas*. *Protein J.* **25**, 288–294 (2006).
- 29. Lee, S.-W., Jang, Y.-N. & Kim, J.-C. Characteristics of the aragonitic layer in adult oyster shells, *Crassostrea gigas*: structural study of myostracum including the adductor muscle scar. *Evid. Based Complement. Alternat. Med.* **2011**, 1–10 (2011).

- 30. Hao, S., Hou, X., Wei, L., Li, J., Li, Z. & Wang, X. Extraction and identification of the pigment in the adductor muscle scar of Pacific oyster *Crassostrea gigas*. *PLoS One* **10**, e0142439 (2015).
- 31. Mann, S. *Biomineralization: principles and concepts in bioinorganic materials chemistry*. (Oxford University Press, 2001).
- 32. Addadi, L., Joester, D., Nudelman, F. & Weiner, S. Mollusk shell formation: a source of new concepts for understanding biomineralization processes. *Chem. Eur. J.* **12**, 980–987 (2006).
- 33. Furuhashi, T., Schwarzinger, C., Miksik, I., Smrz, M. & Beran, A. Molluscan shell evolution with review of shell calcification hypothesis. *Comp. Biochem. Physiol. B Biochem. Mol. Biol.* **154**, 351–371 (2009).
- 34. Marin, F., Le Roy, N. & Marie, B. The formation and mineralization of mollusk shell. Front. Biosci. Sch. Ed. 4, 1099–1125 (2012).
- 35. Cuéllar-Cruz, M. Synthesis of inorganic and organic crystals mediated by proteins in different biological organisms. A mechanism of biomineralization conserved throughout evolution in all living species. *Prog. Cryst. Growth Charact. Mater.* **63**, 94–103 (2017).
- 36. Marin, F. Mollusc shellomes: past, present and future. J. Struct. Biol. 212, 107583 (2020).
- 37. Chateigner, D., Hedegaard, C. & Wenk, H.-R. Mollusc shell microstructures and crystallographic textures. *J. Struct. Geol.* **22**, 1723–1735 (2000).
- 38. Kobayashi, I. & Samata, T. Bivalve shell structure and organic matrix. *Mater. Sci. Eng. C* **26**, 692–698 (2006).
- 39. Barthelat, F., Rim, J. E. & Espinosa, H. D. A review on the structure and mechanical properties of mollusk shells perspectives on synthetic biomimetic materials. in *Applied*

- scanning probe methods XIII (eds. Bhushan, B. & Fuchs, H.) 17–44 (Springer Berlin Heidelberg, 2009).
- 40. Popov, S. V. Formation of bivalve shells and their microstructure. *Paleontol. J.* **48**, 1519–1531 (2014).
- 41. Currey, J. D. & Taylor, J. D. The mechanical behaviour of some molluscan hard tissues. *J. Zool.* **173**, 395–406 (1974).
- 42. Currey, J. D. Further studies on the mechanical properties of mollusc shell material. *J. Zool.* **180**, 445–453 (1976).
- Checa, A. G., Esteban-Delgado, F. J., Ramírez-Rico, J. & Rodríguez-Navarro, A. B.
 Crystallographic reorganization of the calcitic prismatic layer of oysters. *J. Struct. Biol.* 167, 261–270 (2009).
- 44. Dauphin, Y., Ball, A. D., Castillo-Michel, H., Chevallard, C., Cuif, J.-P., Farre, B., Pouvreau, S. & Salomé, M. *In situ* distribution and characterization of the organic content of the oyster shell *Crassostrea gigas* (Mollusca, Bivalvia). *Micron* 44, 373–383 (2013).
- 45. MacDonald, J., Freer, A. & Cusack, M. Alignment of crystallographic c-axis throughout the four distinct microstructural layers of the oyster *Crassostrea gigas*. *Cryst. Growth Des*. **10**, 1243–1246 (2010).
- 46. Nudelman, F., Shimoni, E., Klein, E., Rousseau, M., Bourrat, X., Lopez, E., Addadi, L. & Weiner, S. Forming nacreous layer of the shells of the bivalves *Atrina rigida* and *Pinctada margaritifera*: an environmental- and cryo-scanning electron microscopy study. *J. Struct. Biol.* **162**, 290–300 (2008).
- 47. Checa, A. G., Esteban-Delgado, F. J. & Rodríguez-Navarro, A. B. Crystallographic structure of the foliated calcite of bivalves. *J. Struct. Biol.* **157**, 393–402 (2007).

- 48. Weiss, I. M., Tuross, N., Addadi, L. & Weiner, S. Mollusc larval shell formation: amorphous calcium carbonate is a precursor phase for aragonite. *J. Exp. Zool.* **293**, 478–491 (2002).
- 49. Lee, S. W., Hong, S. M. & Choi, C. S. Characteristics of calcification processes in embryos and larvae of the Pacific oyster, *Crassostrea gigas. Bull. Mar. Sci.* **78**, 309–317 (2006).
- 50. Miyazaki, Y., Nishida, T., Aoki, H. & Samata, T. Expression of genes responsible for biomineralization of *Pinctada fucata* during development. *Comp. Biochem. Physiol. B Biochem. Mol. Biol.* **155**, 241–248 (2010).
- 51. Lee, S.-W., Jang, Y.-N., Ryu, K.-W., Chae, S.-C., Lee, Y.-H. & Jeon, C.-W. Mechanical characteristics and morphological effect of complex crossed structure in biomaterials: fracture mechanics and microstructure of chalky layer in oyster shell. *Micron* **42**, 60–70 (2011).
- 52. Huang, J., Liu, C., Xie, L. & Zhang, R. Amorphous calcium carbonate: a precursor phase for aragonite in shell disease of the pearl oyster. *Biochem. Biophys. Res. Commun.* **497**, 102–107 (2018).
- 53. Kudo, M., Kameda, J., Saruwatari, K., Ozaki, N., Okano, K., Nagasawa, H. & Kogure, T. Microtexture of larval shell of oyster, *Crassostrea nippona*: a FIB-TEM study. *J. Struct. Biol.* **169**, 1–5 (2010).
- 54. Yokoo, N., Suzuki, M., Saruwatari, K., Aoki, H., Watanabe, K., Nagasawa, H. & Kogure, T. Microstructures of the larval shell of a pearl oyster, *Pinctada fucata*, investigated by FIB-TEM technique. *Am. Mineral.* **96**, 1020–1027 (2011).

- 55. Ramesh, K., Melzner, F., Griffith, A. W., Gobler, C. J., Rouger, C., Tasdemir, D. & Nehrke, G. *In vivo* characterization of bivalve larval shells: a confocal Raman microscopy study. *J. R. Soc. Interface* **15**, 20170723 (2018).
- 56. Feng, D., Li, Q., Yu, H., Kong, L. & Du, S. Identification of conserved proteins from diverse shell matrix proteome in *Crassostrea gigas*: characterization of genetic bases regulating shell formation. *Sci. Rep.* **7**, 45754 (2017).
- 57. Ivanina, A. V., Falfushynska, H. I., Beniash, E., Piontkivska, H. & Sokolova, I. M. Biomineralization-related specialization of hemocytes and mantle tissues of the Pacific oyster *Crassostrea gigas*. *J. Exp. Biol.* **220**, 3209–3221 (2017).
- 58. Jayasankar, V., Vasudevan, S. R., Poulose, S. C. & Divipala, I. Nacre formation by epithelial cell cultures from mantle of the black-lip pearl oyster, *Pinctada margaritifera*. *Vitro Cell. Dev. Biol. Anim.* **54**, 477–485 (2018).
- 59. Lee, S. W., Kim, Y. M., Kim, R. H. & Choi, C. S. Nano-structured biogenic calcite: a thermal and chemical approach to folia in oyster shell. *Micron* **39**, 380–386 (2008).
- 60. Cuif, J.-P., Dauphin, Y., Luquet, G., Medjoubi, K., Somogyi, A. & Perez-Huerta, A. Revisiting the organic template model through the microstructural study of shell development in *Pinctada margaritifera*, the Polynesian pearl oyster. *Minerals* **8**, 370 (2018).
- 61. Wang, X., Li, L., Zhu, Y., Du, Y., Song, X., Chen, Y., Huang, R., Que, H., Fang, X. & Zhang, G. Oyster shell proteins originate from multiple organs and their probable transport pathway to the shell formation front. *PLoS ONE* **8**, e66522 (2013).
- 62. Zhang, R., Xie, L. & Yan, Z. Biomineralization mechanism of the pearl oyster, Pinctada fucata. (Springer Singapore, 2019).

- 63. Almeida, M. J., Moura, G., Pinheiro, T., Machado, J. & Coimbra, J. Modifications in *Crassostrea gigas* shell composition exposed to high concentrations of lead. *Aquat. Toxicol.* **40**, 323–334 (1998).
- 64. Huanxin, W., Lejun, Z. & Presley, B. J. Bioaccumulation of heavy metals in oyster (*Crassostrea virginica*) tissue and shell. *Environ. Geol.* **39**, 1216–1226 (2000).
- 65. Fougerouse, A., Rousseau, M. & Lucas, J. S. Soft tissue anatomy, shell structure and biomineralization. in *The pearl oyster* (eds. Southgate, P. C. & Lucas, J. S.) 77–102 (Elsevier, 2008).
- 66. Nakayama, S., Suzuki, M., Endo, H., Iimura, K., Kinoshita, S., Watabe, S., Kogure, T. & Nagasawa, H. Identification and characterization of a matrix protein (PPP-10) in the periostracum of the pearl oyster, *Pinctada fucata*. *FEBS Open Bio* **3**, 421–427 (2013).
- 67. Carriker, M. R., Swann, C. P., Prezant, R. S. & Counts, C. L. Chemical elements in the aragonitic and calcitic microstructural groups of shell of the oyster *Crassostrea virginica*: a proton probe study. *Mar. Biol.* **109**, 287–297 (1991).
- 68. Carter, J. G. & Clark, G. R. Classification and phylogenetic significance of molluscan shell microstructure. *Notes Short Course Stud. Geol.* **13**, 50–71 (1985).
- 69. Morris, J. P., Wang, Y., Backeljau, T. & Chapelle, G. Biomimetic and bio-inspired uses of mollusc shells. *Mar. Genomics* **27**, 85–90 (2016).
- 70. Checa, A. G., Rodríguez-Navarro, A. B. & Esteban-Delgado, F. J. The nature and formation of calcitic columnar prismatic shell layers in pteriomorphian bivalves. *Biomaterials* **26**, 6404–6414 (2005).
- 71. Esteban-Delgado, F. J., Harper, E. M., Checa, A. G. & Rodríguez-Navarro, A. B. Origin and expansion of foliated microstructure in pteriomorph bivalves. *Biol. Bull.* **214**, 153–165 (2008).

- 72. Yamaguchi, K. Shell structure and behaviour related to cementation in oysters. *Mar. Biol.* **118**, 89–100 (1994).
- 73. Nakahara, H. & Bevelander, G. The formation and growth of the prismatic layer of *Pinctada radiata. Calcif. Tissue Res.* **7**, 31–45 (1971).
- 74. Dauphin, Y. Soluble organic matrices of the calcitic prismatic shell layers of two Pteriomorphid bivalves: *Pinna nobilis* and *Pinctada margaritifera*. *J. Biol. Chem.* **278**, 15168–15177 (2003).
- 75. Kobayashi, I. Scanning electron microscopic structure of the prismatic layer in the Bivalvia. *Front. Mater. Sci. China* **2**, 246–252 (2008).
- 76. Dauphin, Y., Ball, A. D., Cotte, M., Cuif, J.-P., Meibom, A., Salomé, M., Susini, J. & Williams, C. T. Structure and composition of the nacre–prisms transition in the shell of *Pinctada margaritifera* (Mollusca, Bivalvia). *Anal. Bioanal. Chem.* 390, 1659–1669 (2008).
- 77. Baronnet, A., Cuif, J.-P., Dauphin, Y., Farre, B. & Nouet, J. Crystallization of biogenic Ca-carbonate within organo-mineral micro-domains. Structure of the calcite prisms of the Pelecypod *Pinctada margaritifera* (Mollusca) at the submicron to nanometre ranges. *Mineral. Mag.* **72**, 617–626 (2008).
- 78. Okumura, T., Suzuki, M., Nagasawa, H. & Kogure, T. Characteristics of biogenic calcite in the prismatic layer of a pearl oyster, *Pinctada fucata*. *Micron* **41**, 821–826 (2010).
- 79. Gilbert, P. U. P. A., Young, A. & Coppersmith, S. N. Measurement of c-axis angular orientation in calcite (CaCO₃) nanocrystals using X-ray absorption spectroscopy. *Proc. Natl. Acad. Sci.* **108**, 11350–11355 (2011).

- 80. Mastropietro, F., Godard, P., Burghammer, M., Chevallard, C., Daillant, J., Duboisset, J., Allain, M., Guenoun, P., Nouet, J. & Chamard, V. Revealing crystalline domains in a mollusc shell single-crystalline prism. *Nat. Mater.* **16**, 946 (2017).
- 81. Kim, Y.-W., Kim, J.-J., Kim, Y. H. & Rho, J.-Y. Effects of organic matrix proteins on the interfacial structure at the bone–biocompatible nacre interface *in vitro*. *Biomaterials* 23, 2089–2096 (2002).
- 82. Oliveira, D. V., Silva, T. S., Cordeiro, O. D., Cavaco, S. I. & Simes, D. C. Identification of proteins with potential osteogenic activity present in the water-soluble matrix proteins from *Crassostrea gigas* nacre using a proteomic approach. *Sci. World J.* **2012**, 1–9 (2012).
- 83. Lu, J., Cong, X., Li, Y., Hao, Y. & Wang, C. Scalable recycling of oyster shells into high purity calcite powders by the mechanochemical and hydrothermal treatments. *J. Clean. Prod.* **172**, 1978–1985 (2018).
- 84. Rousseau, M. Nacre, a natural biomaterial. in *Biomaterials applications for nanomedicine* (ed. Pignatello, R.) 281–298 (InTech, 2011).
- 85. Zhang, G., Brion, A., Willemin, A.-S., Piet, M.-H., Moby, V., Bianchi, A., Mainard, D., Galois, L., Gillet, P. & Rousseau, M. Nacre, a natural, multi-use, and timely biomaterial for bone graft substitution. *J. Biomed. Mater. Res. A* **105**, 662–671 (2017).
- 86. Checa, A. G. & Rodríguez-Navarro, A. B. Self-organisation of nacre in the shells of Pterioida (Bivalvia: Mollusca). *Biomaterials* **26**, 1071–1079 (2005).
- 87. Lertvachirapaiboon, C., Pienpinijtham, P., Wongravee, K. & Ekgasit, S. Optical properties of individual aragonite plates from nacre. *ChemistrySelect* **3**, 11700–11704 (2018).
- 88. Lee, S.-W., Kim, G. H. & Choi, C. S. Characteristic crystal orientation of folia in oyster shell, *Crassostrea gigas. Mater. Sci. Eng. C* **28**, 258–263 (2008).

- 89. Meng, Y., Fitzer, S. C., Chung, P., Li, C., Thiyagarajan, V. & Cusack, M. Crystallographic interdigitation in oyster shell folia enhances material strength. *Cryst. Growth Des.* **18**, 3753–3761 (2018).
- 90. Lee, S. W. & Choi, C. S. The correlation between organic matrices and biominerals (myostracal prism and folia) of the adult oyster shell, *Crassostrea gigas*. *Micron* **38**, 58–64 (2007).
- 91. Marie, B., Zanella-Cléon, I., Guichard, N., Becchi, M. & Marin, F. Novel proteins from the calcifying shell matrix of the Pacific oyster *Crassostrea gigas*. *Mar. Biotechnol.* **13**, 1159–1168 (2011).
- 92. Sikes, C. S., Wheeler, A. P., Wierzbicki, A., Dillaman, R. M. & De Luca, L. Oyster shell protein and atomic force microscopy of oyster shell folia. *Biol. Bull.* **194**, 304–316 (1998).
- 93. Morton, B., Lam, K. & Slack-Smith, S. First report of the European flat oyster *Ostrea edulis*, identified genetically, from Oyster Harbour, Albany, south-western Western Australia. *Molluscan Res.* **23**, 199–208 (2003).
- 94. Checa, A. G., Harper, E. M. & González-Segura, A. Structure and crystallography of foliated and chalk shell microstructures of the oyster *Magallana*: the same materials grown under different conditions. *Sci. Rep.* **8**, (2018).
- 95. Margolis, S. V. & Carver, R. E. Microstructure of chalky deposits found in shells of the oyster *Crassostrea virginica*. *Nautilus* **88**, 62–65 (1974).
- 96. Tassanakajon, A., Vatanavicharn, T., Supungul, P., Tang, S., Amparyup, P., Somboonwiwat, K., Tharntada, S., Takahashi, J. & Toyohara, H. Biotechnology of marine invertebrates recent advances in shrimp and shellfish. in *Fisheries for global welfare and environment* (eds. Tsukamoto, K., Kawamura, T., Takeuchi, T., Beard, T. D. & Kaiser, M. J.) 221–239 (TERRAPUB, 2008).

- 97. Chinzei, K. Adaptation of oysters to life on soft substrates. *Hist. Biol.* **25**, 223–231 (2013).
- 98. Banker, R. M. W. & Sumner, D. Y. Structure and distribution of chalky deposits in the Pacific oyster using x-ray computed tomography (CT). *Sci. Rep.* **10**, 12118 (2020).
- 99. Taylor, J. D. & Layman, M. The mechanical properties of bivalve (Mollusca) shell structures. *Palaeontology* **15**, 73–87 (1972).
- 100. Dauphin, Y., Brunelle, A., Cotte, M., Cuif, J.-P., Farre, B., Laprévote, O., Meibom, A., Salomé, M. & Williams, C. T. A layered structure in the organic envelopes of the prismatic layer of the shell of the pearl oyster *Pinctada margaritifera* (Mollusca, Bivalvia). *Microsc. Microanal.* **16**, 91–98 (2010).
- 101. Almeida, M. J., Machado, J., Moura, G., Azevedo, M. & Coimbra, J. Temporal and local variations in biochemical composition of *Crassostrea gigas* shells. *J. Sea Res.* **40**, 233–249 (1998).
- 102. Higuera-Ruiz, R. & Elorza, J. Biometric, microstructural, and high-resolution trace element studies in *Crassostrea gigas* of Cantabria (Bay of Biscay, Spain): anthropogenic and seasonal influences. *Estuar. Coast. Shelf Sci.* **82**, 201–213 (2009).
- 103. Bourgoin, B. P., Boomer, D., Powell, M. J., Willie, S., Edgar, D. & Evans, D. Instrumental comparison for the determination of cadmium and lead in calcium supplements and other calcium-rich matrices. *Analyst* **117**, 19–22 (1992).
- 104. Ross, E. A., Szabo, N. J. & Tebbett, I. R. Lead content of calcium supplements. *JAMA*284, 1425–1429 (2000).
- 105. Tsai, W.-T. Microstructural characterization of calcite-based powder materials prepared by planetary ball milling. *Materials* **6**, 3361–3372 (2013).

- 106. Yang, X., Zhou, S.-L., Ma, A.-C., Xu, H.-T., Guan, H.-S. & Liu, H.-B. Chemical profiles and identification of key compound caffeine in marine-derived traditional Chinese medicine Ostreae concha. *Mar. Drugs* **10**, 1180–1191 (2012).
- 107. Li, Q., Zhao, D. & Bezard, E. Traditional Chinese medicine for Parkinson's disease: a review of Chinese literature. *Behav. Pharmacol.* **17**, 403–410 (2006).
- 108. Olson, K. Cosmetics in Roman antiquity: substance, remedy, poison. *Class. World* **102**, 291–310 (2009).
- 109. Cho, M. G., Bae, S. M. & Jeong, J. Y. Egg shell and oyster shell powder as alternatives for synthetic phosphate: effects on the quality of cooked ground pork products. *Korean J. Food Sci. Anim. Resour.* **37**, 571–578 (2017).
- 110. Cho, M. G. & Jeong, J. Y. Effects of calcium powder mixtures and binding ingredients as substitutes for synthetic phosphate on the quality properties of ground pork products. *Korean J. Food Sci. Anim. Resour.* **38**, 1179–1188 (2018).
- 111. Kim, Y. S., Choi, Y. M., Noh, D. O., Cho, S. Y. & Suh, H. J. The effect of oyster shell powder on the extension of the shelf life of tofu. *Food Chem.* **103**, 155–160 (2007).
- 112. Shono, M., Shimizu, I., Aoyagi, E., Taniguchi, T., Takenaka, H., Ishikawa, M., Urata, M., Sannomiya, K., Tamaki, K., Harada, N., Nakaya, Y. & Takayama, T. Reducing effect of feeding powdered nacre of *Pinctada maxima* on the visceral fat of rats. *Biosci. Biotechnol. Biochem.* **72**, 2761–2763 (2008).
- 113. Guinotte, F. & Nys, Y. Effects of particle size and origin of calcium sources on eggshell quality and bone mineralization in egg laying hens. *Poult. Sci.* **70**, 583–592 (1991).
- 114. Ahmad, H. A. & Balander, R. J. Alternative feeding regimen of calcium source and phosphorus level for better eggshell quality in commercial layers. *J. Appl. Poult. Res.* **12**, 509–514 (2003).

- 115. Wang, S., Chen, W., Zhang, H. X., Ruan, D. & Lin, Y. C. Influence of particle size and calcium source on production performance, egg quality, and bone parameters in laying ducks. *Poult. Sci.* **93**, 2560–2566 (2014).
- 116. Anwar, M. N., Ravindran, V., Morel, P. C. H., Ravindran, G. & Cowieson, A. J. Effect of calcium source and particle size on the true ileal digestibility and total tract retention of calcium in broiler chickens. *Anim. Feed Sci. Technol.* **224**, 39–45 (2017).
- 117. Ahmed, S. A., Gibriel, A. A. Y., Abdellatif, A. K. & Ebied, H. M. Evaluation of food products fortified with oyster shell for the prevention and treatment of osteoporosis. *J. Food Sci. Technol.* **52**, 6816–6820 (2015).
- 118. Lee, Y.-K., Jung, S. K., Chang, Y. H. & Kwak, H.-S. Highly bioavailable nanocalcium from oyster shell for preventing osteoporosis in rats. *Int. J. Food Sci. Nutr.* 1–10 (2017).
- 119. Palaniappan, M., Selvarajan, S., Srinivasamurthy, S. & Chandrasekaran, A. Oyster shell calcium induced parotid swelling. *J. Pharmacol. Pharmacother.* **5**, 256–257 (2014).
- 120. Chang, F., Li, G., Haws, M. & Niu, T. Element concentrations in shell of *Pinctada margaritifera* from French Polynesia and evaluation for using as a food supplement. *Food Chem.* **104**, 1171–1176 (2007).
- 121. Green, D., Lai, W.-F. & Jung, H.-S. Evolving marine biomimetics for regenerative dentistry. *Mar. Drugs* **12**, 2877–2912 (2014).
- 122. Atlan, G., Delattre, O., Berland, S., Le Faou, A., Nabias, G., Cot, D. & Lopez, E. Interface between bone and nacre implants in sheep. *Biomaterials* **20**, 1017–1022 (1999).
- 123. Westbroek, P. & Marin, F. A marriage of bone and nacre. *Nature* **392**, 861–862 (1998).
- 124. Flausse, A., Henrionnet, C., Dossot, M., Dumas, D., Hupont, S., Pinzano, A., Mainard, D., Galois, L., Magdalou, J., Lopez, E., Gillet, P. & Rousseau, M. Osteogenic

- differentiation of human bone marrow mesenchymal stem cells in hydrogel containing nacre powder. *J. Biomed. Mater. Res. A* **101**, 3211–3218 (2013).
- 125. Coringa, R., de Sousa, E. M., Botelho, J. N., Diniz, R. S., de Sá, J. C., da Cruz, M. C. F. N., Paschoal, M. A. B. & Gonçalves, L. M. Bone substitute made from a Brazilian oyster shell functions as a fast stimulator for bone-forming cells in an animal model. *PLoS ONE* 13, e0198697 (2018).
- 126. Brundavanam, R. K., Fawcett, D. & Poinern, G. E. J. Synthesis of a bone like composite material derived from waste pearl oyster shells for potential bone tissue bioengineering applications. *Int. J. Res. Med. Sci.* **5**, 2454 (2017).
- 127. Shen, Y., Yang, S., Liu, J., Xu, H., Shi, Z., Lin, Z., Ying, X., Guo, P., Lin, T., Yan, S., Huang, Q. & Peng, L. Engineering scaffolds integrated with calcium sulfate and oyster shell for enhanced bone tissue regeneration. *ACS Appl. Mater. Interfaces* **6**, 12177–12188 (2014).
- 128. Didekhani, R., Sohrabi, M. R., Seyedjafari, E., Soleimani, M. & Hanaee-Ahvaz, H. Electrospun composite PLLA/Oyster shell scaffold enhances proliferation and osteogenic differentiation of stem cells. *Biologicals* **54**, 33–38 (2018).
- 129. Didekhani, R., Sohrabi, M. R., Soleimani, M., Seyedjafari, E. & Hanaee-Ahvaz, H. Incorporating PCL nanofibers with oyster shell to improve osteogenic differentiation of mesenchymal stem cells. *Polym. Bull.* **77**, 701–715 (2020).
- 130. Luo, W., Zhang, S., Lan, Y., Huang, C., Wang, C., Lai, X., Chen, H. & Ao, N. 3D printed porous polycaprolactone/oyster shell powder (PCL/OSP) scaffolds for bone tissue engineering. *Mater. Res. Express* **5**, 045403 (2018).

- 131. Lopez, E., Le Faou, A., Borzeix, S. & Berland, S. Stimulation of rat cutaneous fibroblasts and their synthetic activity by implants of powdered nacre (mother of pearl). *Tissue Cell* **32**, 95–101 (2000).
- 132. Chen, Y., Jiang, Y., Liao, L., Zhu, X., Tang, S., Yang, Q., Sun, L., Li, Y., Gao, S. & Xie,
 Z. Inhibition of 4NQO-induced oral carcinogenesis by dietary oyster shell calcium. *Integr. Cancer Ther.* 15, 96–101 (2016).
- 133. Moon, D. H., Chang, Y.-Y., Ok, Y. S., Cheong, K. H., Koutsospyros, A. & Park, J.-H. Amelioration of acidic soil using various renewable waste resources. *Environ. Sci. Pollut. Res.* 21, 774–780 (2014).
- 134. Lee, K.-Y., Moon, D. H., Lee, S.-H., Kim, K.-W., Cheong, K.-H., Park, J.-H., Ok, Y. S. & Chang, Y.-Y. Simultaneous stabilization of arsenic, lead, and copper in contaminated soil using mixed waste resources. *Environ. Earth Sci.* 69, 1813–1820 (2013).
- 135. Du, Y., Lian, F. & Zhu, L. Biosorption of divalent Pb, Cd and Zn on aragonite and calcite mollusk shells. *Environ. Pollut.* **159**, 1763–1768 (2011).
- 136. Ok, Y. S., Lim, J. E. & Moon, D. H. Stabilization of Pb and Cd contaminated soils and soil quality improvements using waste oyster shells. *Environ. Geochem. Health* **33**, 83–91 (2011).
- 137. Lim, J. E., Ahmad, M., Lee, S. S., Shope, C. L., Hashimoto, Y., Kim, K.-R., Usman, A. R. A., Yang, J. E. & Ok, Y. S. Effects of lime-based waste materials on immobilization and phytoavailability of cadmium and lead in contaminated soil: lime-based waste materials on metal immobilization. *CLEAN Soil Air Water* **41**, 1235–1241 (2013).
- 138. Zhang, Z., Guo, G., Teng, Y., Wang, J., Rhee, J. S., Wang, S. & Li, F. Screening and assessment of solidification/stabilization amendments suitable for soils of lead-acid battery contaminated site. *J. Hazard. Mater.* **288**, 140–146 (2015).

- 139. Hong, C. O., Lee, D. K., Chung, D. Y. & Kim, P. J. Liming effects on cadmium stabilization in upland soil affected by gold mining activity. *Arch. Environ. Contam. Toxicol.* **52**, 496–502 (2007).
- 140. Chang, Y.-T., Hsi, H.-C., Hseu, Z.-Y. & Jheng, S.-L. Chemical stabilization of cadmium in acidic soil using alkaline agronomic and industrial by-products. *J. Environ. Sci. Health Part A* **48**, 1748–1756 (2013).
- 141. Chen, Y., Xu, J., Lv, Z., Xie, R., Huang, L. & Jiang, J. Impacts of biochar and oyster shells waste on the immobilization of arsenic in highly contaminated soils. *J. Environ. Manage*. **217**, 646–653 (2018).
- 142. Gao, Y.-J. Removal of cadmium and cobalt from heavy metal solution using oyster shells adsorbent. *Asian J. Chem.* **25**, 8537–8540 (2013).
- 143. Gao, Y.-J. Removal of heavy metals from synthetic landfill leachate using oyster shells adsorbent. *Asian J. Chem.* **25**, 8533–8536 (2013).
- 144. Lee, C. H., Lee, D. K., Ali, M. A. & Kim, P. J. Effects of oyster shell on soil chemical and biological properties and cabbage productivity as a liming materials. *Waste Manag.* **28**, 2702–2708 (2008).
- 145. Awad, Y. M., Lee, S. S., Kim, K.-H., Ok, Y. S. & Kuzyakov, Y. Carbon and nitrogen mineralization and enzyme activities in soil aggregate-size classes: effects of biochar, oyster shells, and polymers. *Chemosphere* **198**, 40–48 (2018).
- 146. Kwon, Y. T., Lee, C. W. & Yun, J. H. Development of vermicast from sludge and powdered oyster shell. *J. Clean. Prod.* **17**, 708–711 (2009).
- 147. Seo, D. C., Cho, J. S., Lee, H. J. & Heo, J. S. Phosphorus retention capacity of filter media for estimating the longevity of constructed wetland. *Water Res.* **39**, 2445–2457 (2005).

- 148. Park, W. H. & Polprasert, C. Phosphorus adsorption characteristics of oyster shells and alum sludge and their application for nutrient control in constructed wetland system. *J. Environ. Sci. Health Part A* **43**, 511–517 (2008).
- 149. Bricker, S. B. *et al.* Role of shellfish aquaculture in the reduction of eutrophication in an urban estuary. *Environ. Sci. Technol.* **52**, 173–183 (2018).
- 150. Jeon, J., Kannan, K., Lim, H. K., Moon, H. B., Ra, J. S. & Kim, S. D. Bioaccumulation of perfluorochemicals in Pacific oyster under different salinity gradients. *Environ. Sci. Technol.* 44, 2695–2701 (2010).
- 151. Liu, F. & Wang, W.-X. Facilitated bioaccumulation of cadmium and copper in the oyster *Crassostrea hongkongensis* solely exposed to zinc. *Environ. Sci. Technol.* **47**, 1670–1677 (2013).
- 152. Cole, M. & Galloway, T. S. Ingestion of nanoplastics and microplastics by Pacific oyster larvae. *Environ. Sci. Technol.* **49**, 14625–14632 (2015).
- 153. Tan, Q.-G., Zhou, W. & Wang, W.-X. Modeling the toxicokinetics of multiple metals in the oyster *Crassostrea hongkongensis* in a dynamic estuarine environment. *Environ. Sci. Technol.* **52**, 484–492 (2018).
- 154. Tamjidi, S. & Ameri, A. A review of the application of sea material shells as low cost and effective bio-adsorbent for removal of heavy metals from wastewater. *Environ. Sci. Pollut. Res.* 27, 31105–31119 (2020).
- 155. Huang, X., Zheng, J., Liu, C., Liu, L., Liu, Y. & Fan, H. Removal of antibiotics and resistance genes from swine wastewater using vertical flow constructed wetlands: effect of hydraulic flow direction and substrate type. *Chem. Eng. J.* **308**, 692–699 (2017).

- 156. Melegari, S. P. & Matias, W. G. Preliminary assessment of the performance of oyster shells and chitin materials as adsorbents in the removal of saxitoxin in aqueous solutions. *Chem. Cent. J.* **6**, 86 (2012).
- 157. Shih, P.-K. & Chang, W.-L. The effect of water purification by oyster shell contact bed. *Ecol. Eng.* **77**, 382–390 (2015).
- 158. Lee, C. W., Kwon, H. B., Jeon, H. P. & Koopman, B. A new recycling material for removing phosphorus from water. *J. Clean. Prod.* **17**, 683–687 (2009).
- 159. Yu, Y., Wu, R. & Clark, M. Phosphate removal by hydrothermally modified fumed silica and pulverized oyster shell. *J. Colloid Interface Sci.* **350**, 538–543 (2010).
- 160. Chen, W.-T., Lin, C.-W., Shih, P.-K. & Chang, W.-L. Adsorption of phosphate into waste oyster shell: thermodynamic parameters and reaction kinetics. *Desalination Water Treat*. **47**, 86–95 (2012).
- 161. Chen, J., Cai, Y., Clark, M. & Yu, Y. Equilibrium and kinetic studies of phosphate removal from solution onto a hydrothermally modified oyster shell material. *PLoS ONE* 8, e60243 (2013).
- 162. Adhikari, R. A., Bal Krishna, K. & Sarukkalige, R. Evaluation of phosphorus adsorption capacity of various filter materials from aqueous solution. *Adsorpt. Sci. Technol.* **34**, 320–330 (2016).
- 163. Martins, M. C., Santos, E. B. H. & Marques, C. R. First study on oyster-shell-based phosphorous removal in saltwater a proxy to effluent bioremediation of marine aquaculture. *Sci. Total Environ.* **574**, 605–615 (2017).
- 164. Cui, M., Jang, M., Kang, K., Kim, D., Snyder, S. A. & Khim, J. A novel sequential process for remediating rare-earth wastewater. *Chemosphere* **144**, 2081–2090 (2016).

- 165. Sengupta, S., Ergas, S. J., Lopez-Luna, E., Sahu, A. K. & Palaniswamy, K. Autotrophic biological denitrification for complete removal of nitrogen from septic system wastewater.
 Water Air Soil Pollut. Focus 6, 111–126 (2006).
- 166. Simard, M.-C., Masson, S., Mercier, G., Benmoussa, H., Blais, J.-F. & Coudert, L. Autotrophic denitrification using elemental sulfur to remove nitrate from saline aquarium waters. *J. Environ. Eng.* **141**, 04015037 (2015).
- 167. Xiong, X. & Ye, Z. Study of nitrification behavior in aerated biofilters using oyster shell carrier. *Aquat. Ecosyst. Health Manag.* **9**, 15–19 (2006).
- 168. Caffrey, J. M., Hollibaugh, J. T. & Mortazavi, B. Living oysters and their shells as sites of nitrification and denitrification. *Mar. Pollut. Bull.* **112**, 86–90 (2016).
- 169. Hsu, T.-C. Experimental assessment of adsorption of Cu²⁺ and Ni²⁺ from aqueous solution by oyster shell powder. *J. Hazard. Mater.* **171**, 995–1000 (2009).
- 170. Wu, Q., Chen, J., Clark, M. & Yu, Y. Adsorption of copper to different biogenic oyster shell structures. *Appl. Surf. Sci.* **311**, 264–272 (2014).
- 171. Yen, H. Y. & Li, J. Y. Process optimization for Ni(II) removal from wastewater by calcined oyster shell powders using Taguchi method. *J. Environ. Manage.* **161**, 344–349 (2015).
- 172. Cui, M., Jang, M., Na, S., Lee, S. & Khim, J. Catalytic assistance of ultrasound for manganese removal by waste oyster shells. *J. Environ. Manage.* **115**, 235–240 (2013).
- 173. Fan, L., Zhang, S., Zhang, X., Zhou, H., Lu, Z. & Wang, S. Removal of arsenic from simulation wastewater using nano-iron/oyster shell composites. *J. Environ. Manage.* **156**, 109–114 (2015).

- 174. Zhou, X., Liu, W., Zhang, J., Wu, C., Ou, X., Tian, C., Lin, Z. & Dang, Z. Biogenic calcium carbonate with hierarchical organic–inorganic composite structure enhancing the removal of Pb(II) from wastewater. *ACS Appl. Mater. Interfaces* **9**, 35785–35793 (2017).
- 175. Liu, Y., Sun, C., Xu, J. & Li, Y. The use of raw and acid-pretreated bivalve mollusk shells to remove metals from aqueous solutions. *J. Hazard. Mater.* **168**, 156–162 (2009).
- 176. Yokogawa, Y., Nagata, F., Kameyama, T. & Suzuki, T. Development of porous materials as carriers immobilizing a microorganism for water purification prepared by using waste materials. *Phosphorus Res. Bull.* **13**, 265–270 (2002).
- 177. Moon, H. S., Nam, K. & Kim, J. Y. Initial alkalinity requirement and effect of alkalinity sources in sulfur-based autotrophic denitrification barrier system. *J. Environ. Eng.* **132**, 971–975 (2006).
- 178. Sahu, A. K., Conneely, T., Nüsslein, K. R. & Ergas, S. J. Biological perchlorate reduction in packed bed reactors using elemental sulfur. *Environ. Sci. Technol.* **43**, 4466–4471 (2009).
- 179. Yam, R., Hsu, C.-C., Chang, T.-J. & Chang, W.-L. A preliminary investigation of wastewater treatment efficiency and economic cost of subsurface flow oyster-shell-bedded constructed wetland systems. *Water* **5**, 893–916 (2013).
- 180. Feng, Y., Li, X., Yu, Y., Qi, J., Jia, X., Wang, J. & Li, X. Production of unburned calcium silicon filter material (UCSFM) from oyster shell and its performance investigation in an A/O integrated biological aerated filter reactor (A/O-BAF). *RSC Adv.* **6**, 85324–85332 (2016).
- 181. Jung, S., Heo, N. S., Kim, E. J., Oh, S. Y., Lee, H. U., Kim, I. T., Hur, J., Lee, G.-W., Lee, Y.-C. & Huh, Y. S. Feasibility test of waste oyster shell powder for water treatment. *Process Saf. Environ. Prot.* **102**, 129–139 (2016).

- 182. Tong, S., Stocks, J. L., Rodriguez-Gonzalez, L. C., Feng, C. & Ergas, S. J. Effect of oyster shell medium and organic substrate on the performance of a particulate pyrite autotrophic denitrification (PPAD) process. *Bioresour. Technol.* **244**, 296–303 (2017).
- 183. Wang, B., Zhang, Q. & Hong, J. Fe⁰/C-bentonite alginate beads and oyster shell fixed-bed column combined process to continuously remove N-acetyl-p-aminophenol in persulfate system. *J. Ind. Eng. Chem.* **67**, 301–311 (2018).
- 184. Njoyim, E., Ghogomu, P., Laminsi, S., Nzali, S., Doubla, A. & Brisset, J.-L. Coupling gliding discharge treatment and catalysis by oyster shell powder for pollution abatement of surface waters. *Ind. Eng. Chem. Res.* **48**, 9773–9780 (2009).
- 185. Chiou, I. J., Chen, C. H. & Li, Y. H. Using oyster-shell foamed bricks to neutralize the acidity of recycled rainwater. *Constr. Build. Mater.* **64**, 480–487 (2014).
- 186. Jung, Y.-J., Koh, H.-W., Shin, W.-T. & Sung, N.-C. A novel approach to an advanced tertiary wastewater treatment: combination of a membrane bioreactor and an oyster-zeolite column. *Desalination* **190**, 243–255 (2006).
- 187. Luo, H., Huang, G., Fu, X., Liu, X., Zheng, D., Peng, J., Zhang, K., Huang, B., Fan, L., Chen, F. & Sun, X. Waste oyster shell as a kind of active filler to treat the combined wastewater at an estuary. *J. Environ. Sci.* **25**, 2047–2055 (2013).
- 188. Nestlerode, J. A., Luckenbach, M. W. & O'Beirn, F. X. Settlement and survival of the oyster *Crassostrea virginica* on created oyster reef habitats in Chesapeake Bay. *Restor. Ecol.* **15**, 273–283 (2007).
- 189. Tongamp, W., Kano, J., Zhang, Q. & Saito, F. Simultaneous treatment of PVC and oystershell wastes by mechanochemical means. *Waste Manag.* **28**, 484–488 (2008).

- 190. Tongamp, W., Kano, J., Suzuta, Y., Saito, F. & Themelis, N. J. Relation between mechanochemical dechlorination rate of polyvinyl chloride and mill power consumption. *J. Mater. Cycles Waste Manag.* 11, 32–37 (2009).
- 191. Yao, Z., Heng, J. Y. Y., Lanceros-Méndez, S., Pegoretti, A., Xia, M., Tang, J. & Wu, W. Surface free energy and mechanical performance of LDPE/CBF composites containing toxic-metal free filler. *Int. J. Adhes. Adhes.* 77, 58–62 (2017).
- 192. Chong, M. H., Chun, B. C., Chung, Y.-C. & Cho, B. G. Fire-retardant plastic material from oyster-shell powder and recycled polyethylene. *J. Appl. Polym. Sci.* **99**, 1583–1589 (2006).
- 193. Shah, A. ur R., Prabhakar, M. N., Saleem, M. & Song, J.-I. Development of biowaste encapsulated polypropylene composites: thermal, optical, dielectric, flame retardant, mechanical, and morphological properties. *Polym. Compos.* **38**, 236–243 (2017).
- 194. Shah, A. ur R., Prabhakar, M. N., Wang, H. & Song, J.-I. The influence of particle size and surface treatment of filler on the properties of oyster shell powder filled polypropylene composites. *Polym. Compos.* **39**, 2420–2430 (2018).
- 195. Li, L., Zeng, Z., Wang, Z., Peng, Z., She, X., Li, S. & Zhong, J. Effect of oyster shell powder loading on the mechanical and thermal properties of natural rubber/oyster shell composites. *Polym. Polym. Compos.* **25**, 17–22 (2017).
- 196. Nciri, N., Shin, T., Lee, H. & Cho, N. Potential of waste oyster shells as a novel biofiller for hot-mix asphalt. *Appl. Sci.* **8**, 415 (2018).
- 197. Chen, X., Zhang, X., Wang, W., Wang, Y. & Jiao, C. Fire-safe agent integrated with oyster shell and melamine polyphosphate for thermoplastic polyurethane. *Polym. Adv. Technol.* **30**, 1576–1588 (2019).

- 198. H. Silva, T., Mesquita-Guimarães, J., Henriques, B., Silva, F. S. & Fredel, M. C. The potential use of oyster shell waste in new value-added by-product. *Resources* **8**, 13 (2019).
- 199. Liu, C.-H., Lee, H.-T., Tsou, C.-H., Wang, C.-C., Gu, J.-H. & Suen, M.-C. Preparation and characterization of biodegradable polyurethane composites containing oyster shell powder. *Polym. Bull.* **77**, 3325–3347 (2020).
- 200. Teixeira, L. B., Fernandes, V. K., Maia, B. G. O., Arcaro, S. & Novaes de Oliveira, A. P. Vitrocrystalline foams produced from glass and oyster shell wastes. *Ceram. Int.* **43**, 6730–6737 (2017).
- 201. Lee, S. W., Kang, G., Lee, K. B. & Park, S. B. New approach for fabrication of folded-structure SiO₂ using oyster shell. *Micron* **40**, 713–718 (2009).
- 202. Gao, F., Geng, C., Xiao, N., Qu, J. & Qiu, J. Hierarchical porous carbon sheets derived from biomass containing an activation agent and in-built template for lithium ion batteries. *Carbon* **139**, 1085–1092 (2018).
- 203. Xiong, X., Cai, L., Jiang, Y. & Han, Q. Eco-efficient, green, and scalable synthesis of 1,2,3-triazoles catalyzed by Cu(I) catalyst on waste oyster shell powders. *ACS Sustain. Chem. Eng.* **2**, 765–771 (2014).
- 204. Kordoghli, S., Paraschiv, M., Tazerout, M., Khiari, B. & Zagrouba, F. Novel catalytic systems for waste tires pyrolysis: optimization of gas fraction. *J. Energy Resour. Technol.* **139**, 032203 (2016).
- 205. Chen, H.-Y., Li, L. G., Lai, Z., Kwan, A. K. H., Chen, P. & Ng, P. L. Effects of crushed oyster shell on strength and durability of marine concrete containing fly ash and blastfurnace slag. *Mater. Sci.* **25**, 97–107 (2019).

- 206. Luhar, S., Cheng, T.-W. & Luhar, I. Incorporation of natural waste from agricultural and aquacultural farming as supplementary materials with green concrete: a review. *Compos. Part B Eng.* **175**, 107076 (2019).
- 207. Mo, K. H., Alengaram, U. J., Jumaat, M. Z., Lee, S. C., Goh, W. I. & Yuen, C. W. Recycling of seashell waste in concrete: a review. *Constr. Build. Mater.* **162**, 751–764 (2018).
- 208. Eziefula, U. G., Ezeh, J. C. & Eziefula, B. I. Properties of seashell aggregate concrete: a review. *Constr. Build. Mater.* **192**, 287–300 (2018).
- 209. Ramakrishna, C., Thenepalli, T., Han, C. & Ahn, J.-W. Synthesis of aragonite-precipitated calcium carbonate from oyster shell waste via a carbonation process and its applications. *Korean J. Chem. Eng.* **34**, 225–230 (2017).
- 210. Zhao, W., Gao, C., Guo, F. & Wu, Y. Synthesis of calcium sulfate hemihydrate whiskers using oyster shells. *Res. Chem. Intermed.* **42**, 2953–2961 (2016).
- Lemos, A. F., Rocha, J. H. G., Quaresma, S. S. F., Kannan, S., Oktar, F. N., Agathopoulos,
 S. & Ferreira, J. M. F. Hydroxyapatite nano-powders produced hydrothermally from nacreous material. *J. Eur. Ceram. Soc.* 26, 3639–3646 (2006).
- 212. Terasaka, S., Kamitakahara, M., Yokoi, T. & Matsubara, H. Ability of hydroxyapatite synthesized from waste oyster shells to remove fluoride ions. *Mater. Trans.* **56**, 1509–1512 (2015).
- 213. Wang, Z., Jiang, S., Zhao, Y. & Zeng, M. Synthesis and characterization of hydroxyapatite nano-rods from oyster shell with exogenous surfactants. *Mater. Sci. Eng. C* **105**, 110102 (2019).

- 214. Lee, K. B., Lee, S. W. & Park, S. B. Growth of single-crystalline sodium titanate and sodium tungstate one-dimensional nanostructures: bio-inspired approach using oyster shell. *J. Cryst. Growth* **311**, 4365–4370 (2009).
- 215. Khan, M. D., Ahn, J. W. & Nam, G. Environmental benign synthesis, characterization and mechanism studies of green calcium hydroxide nano-plates derived from waste oyster shells. *J. Environ. Manage.* **223**, 947–951 (2018).
- 216. You, W., Hong, M., Zhang, H., Wu, Q., Zhuang, Z. & Yu, Y. Functionalized calcium silicate nanofibers with hierarchical structure derived from oyster shells and their application in heavy metal ions removal. *Phys. Chem. Chem. Phys.* **18**, 15564–15573 (2016).
- 217. Ha, S., Lee, J. W., Choi, S.-H., Kim, S.-H., Kim, K. & Kim, Y. Calcination characteristics of oyster shells and their comparison with limestone from the perspective of waste recycling. *J. Mater. Cycles Waste Manag.* **21**, 1075–1084 (2019).
- 218. Tayeh, B. A., Hasaniyah, M. W., Zeyad, A. M. & Yusuf, M. O. Properties of concrete containing recycled seashells as cement partial replacement: a review. *J. Clean. Prod.* 237, 117723 (2019).
- 219. Soisuwan, S., Phommachant, J., Wisaijorn, W. & Praserthdam, P. The characteristics of green calcium oxide derived from aquatic materials. *Procedia Chem.* **9**, 53–61 (2014).
- 220. Bourrat, X., Francke, L., Lopez, E., Rousseau, M., Stempflé, P., Angellier, M. & Albéric,
 P. Nacre biocrystal thermal behaviour. *CrystEngComm* 9, 1205–1208 (2007).
- 221. Wardecki, D., Przeniosło, R. & Brunelli, M. Internal pressure in annealed biogenic aragonite. *CrystEngComm* **10**, 1450–1453 (2008).
- 222. Kwon, H.-B., Lee, C.-W., Jun, B.-S., Yun, J., Weon, S.-Y. & Koopman, B. Recycling waste oyster shells for eutrophication control. *Resour. Conserv. Recycl.* **41**, 75–82 (2004).

- 223. Huang, Y.-F., Lee, Y.-T., Chiueh, P.-T. & Lo, S.-L. Microwave calcination of waste oyster shells for CO₂ capture. *Energy Procedia* **152**, 1242–1247 (2018).
- 224. Fujita, T. Active absorbable algal calcium (AAA Ca): new Japanese technology for osteoporosis and calcium paradox disease. *J. Assoc. Physicians India* **52**, 564–567 (2004).
- 225. Fujita, T., Fukase, M., Nakada, M. & Koishi, M. Intestinal absorption of oyster shell electrolysate. *Bone Miner.* **4**, 321–327 (1988).
- 226. Fujita, T., Kitazawa, R., Fukase, M., Uchida, K., Matsuda, S. & Nakai, T. Effect of calcium supplementation as oyster shell heated *in vacuo* on metabolism and survival of rats. *J. Bone Miner. Metab.* **13**, 93–97 (1995).
- 227. Fujita, T. Osteoporosis: past, present and future. *Osteoporos. Int.* **7**, 6–9 (1997).
- 228. Fujita, T., Fukase, M., Miyamoto, H., Matsumoto, T. & Ohue, T. Increase of bone mineral density by calcium supplement with oyster shell electrolysate. *Bone Miner.* **11**, 85–91 (1990).
- 229. Fujita, T. Oyster shell electrolysate (AACa) with high biological availability. *J. Bone Miner. Metab.* **11**, S41–S45 (1993).
- 230. Fujita, T., Fujii, Y., Goto, B., Miyauchi, A., Takagi, Y., Kobayashi, S., Kamoshita, K., Mikuni, N., Kurihara, Y. & Shikauchi, I. Increase of intestinal calcium absorption and bone mineral density by heated algal ingredient (HAI) in rats. *J. Bone Miner. Metab.* **18**, 165–169 (2000).
- 231. Miyauchi, A., Fujita, T., Ohue, M., Fujii, Y. & Takagi, Y. Reappraisal of Katsuragi Calcium study, a prospective, double-blind, placebo-controlled study of the effect of active absorbable algal calcium (AAACa) on vertebral deformity and fracture. *J. Bone Miner. Metab.* 22, 32–38 (2004).

- 232. Uenishi, K., Fujita, T., Ishida, H., Fujii, Y., Ohue, M., Kaji, H., Hirai, M., Kakumoto, M. & Abrams, S. A. Fractional absorption of active absorbable algal calcium (AAACa) and calcium carbonate measured by a dual stable-isotope method. *Nutrients* 2, 752–761 (2010).
- 233. Fujita, T., Fujii, Y., Goto, B., Miyauchi, A. & Takagi, Y. Peripheral computed tomography (pQCT) detected short-term effect of AAACa (heated oyster shell with heated algal ingredient HAI): A double-blind comparison with CaCO₃ and placebo. *J. Bone Miner. Metab.* **18**, 212–215 (2000).
- 234. Fujita, T., Ohue, M., Fujii, Y., Miyauchi, A. & Takagi, Y. The effect of active absorbable algal calcium (AAA Ca) with collagen and other matrix components on back and joint pain and skin impedance. *J. Bone Miner. Metab.* **20**, 298–302 (2002).
- 235. Fujita, T., Ohgitani, S. & Nomura, M. Fall of blood ionized calcium on watching a provocative TV program and its prevention by active absorbable algal calcium (AAA Ca). *J. Bone Miner. Metab.* **17**, 131–136 (1999).
- 236. Lyu, W., Jia, H., Deng, C., Saito, K., Yamada, S. & Kato, H. Zeolite-containing mixture supplementation ameliorated dextran sodium sulfate-induced colitis in mice by suppressing the inflammatory bowel disease pathway and improving apoptosis in colon mucosa. *Nutrients* **9**, (2017).
- 237. Ahmad, M., Moon, D. H., Wazne, M., Kim, H. J., Lee, Y. H. & Ok, Y. S. Effects of natural and calcined oyster shells on antimony solubility in shooting range soil. *J. Korean Soc. Appl. Biol. Chem.* **56**, 461–464 (2013).
- 238. Moon, D. H., Oh, D.-Y., Wazne, M. & Park, J.-H. Immobilization of As and Pb in contaminated sediments using waste resources. *Environ. Earth Sci.* **69**, 2721–2729 (2013).

- 239. Moon, D. H., Cheong, K. H., Koutsospyros, A., Chang, Y.-Y., Hyun, S., Ok, Y. S. & Park, J.-H. Assessment of waste oyster shells and coal mine drainage sludge for the stabilization of As-, Pb-, and Cu-contaminated soil. *Environ. Sci. Pollut. Res.* **23**, 2362–2370 (2016).
- 240. Alidoust, D., Kawahigashi, M., Yoshizawa, S., Sumida, H. & Watanabe, M. Mechanism of cadmium biosorption from aqueous solutions using calcined oyster shells. *J. Environ. Manage.* **150**, 103–110 (2015).
- 241. Yen, H. Y. Taguchi optimization for Cd(II) removal from aqueous solutions using oyster shell powders. *Desalination Water Treat.* **57**, 20430–20438 (2016).
- 242. Lee, H. H., Kim, S. Y., Owens, V. N., Park, S., Kim, J. & Hong, C. O. How does oyster shell immobilize cadmium? *Arch. Environ. Contam. Toxicol.* **74**, 114–120 (2018).
- 243. Currie, J. A., Harrison, N. R., Wang, L., Jones, M. I. & Brooks, M. S. A preliminary study of processing seafood shells for eutrophication control. *Asia-Pac. J. Chem. Eng.* **2**, 460–467 (2007).
- 244. Nam, G., Choi, Y.-H., Lee, N. & Ahn, J. Effect by alkaline flocculation of algae and phosphorous from water using a calcined waste oyster shell. *Water* **9**, 661 (2017).
- 245. Tsai, H.-C., Lo, S.-L. & Kuo, J. Using pretreated waste oyster and clam shells and microwave hydrothermal treatment to recover boron from concentrated wastewater. *Bioresour. Technol.* **102**, 7802–7806 (2011).
- 246. Thenepalli, T., Ramakrishna, C. & Ahn, J. W. Environmental effect of the coffee waste and anti-microbial property of oyster shell waste treatment. *J. Energy Eng.* **26**, 39–49 (2017).
- 247. Olalekan, S., Olanrewaju, A., Olatunde, A. & Omolola, J. Potential application of oyster shell as adsorbent in vegetable oil refining. *Adv. Res.* **6**, 1–8 (2016).

- 248. Jung, J.-H., Yoo, K.-S., Kim, H.-G., Lee, H.-K. & Shon, B.-H. Reuse of waste oyster shells as a SO₂/NO_x removal absorbent. *J. Ind. Eng. Chem.* **13**, 512–517 (2007).
- 249. Asaoka, S., Yamamoto, T., Kondo, S. & Hayakawa, S. Removal of hydrogen sulfide using crushed oyster shell from pore water to remediate organically enriched coastal marine sediments. *Bioresour. Technol.* **100**, 4127–4132 (2009).
- 250. Wang, T., Xiao, D.-C., Huang, C.-H., Hsieh, Y.-K., Tan, C.-S. & Wang, C.-F. CO₂ uptake performance and life cycle assessment of CaO-based sorbents prepared from waste oyster shells blended with PMMA nanosphere scaffolds. *J. Hazard. Mater.* **270**, 92–101 (2014).
- 251. Ma, K.-W. & Teng, H. CaO powders from oyster shells for efficient CO₂ capture in multiple carbonation cycles. *J. Am. Ceram. Soc.* **93**, 221–227 (2010).
- 252. Ferraz, E., Gamelas, J. A. F., Coroado, J., Monteiro, C. & Rocha, F. Recycling waste seashells to produce calcitic lime: characterization and wet slaking reactivity. *Waste Biomass Valorization* (2018).
- 253. Rujitanapanich, S., Kumpapan, P. & Wanjanoi, P. Synthesis of hydroxyapatite from oyster shell via precipitation. *Energy Procedia* **56**, 112–117 (2014).
- 254. Li, G., Xu, X., Chen, E., Fan, J. & Xiong, G. Properties of cement-based bricks with oyster-shells ash. *J. Clean. Prod.* **91**, 279–287 (2015).
- 255. Binag, N. H. D. Utilization of shell wastes for locally based cement mortar and bricks production: its impact to the community. *KnE Soc. Sci.* **3**, 985–1004 (2018).
- 256. Wu, S.-C., Hsu, H.-C., Hsu, S.-K., Tseng, C.-P. & Ho, W.-F. Preparation and characterization of hydroxyapatite synthesized from oyster shell powders. *Adv. Powder Technol.* **28**, 1154–1158 (2017).

- 257. Wu, S.-C., Hsu, H.-C., Hsu, S.-K., Tseng, C.-P. & Ho, W.-F. Effects of calcination on synthesis of hydroxyapatite derived from oyster shell powders. *J. Aust. Ceram. Soc.* (2019).
- 258. Wu, Y., Wei, J., Guo, S., Yu, K., Zhuang, Z. & Yu, Y. Recycling biowaste shells to produce 0D/2D Mn–Ca nanostructures for efficient trace-level metal extraction: confined growth of nanosheets and good dispersion of quantum dots. *J. Mater. Chem. A* **5**, 20448–20457 (2017).
- 259. Heriyanto, Pahlevani, F. & Sahajwalla, V. Synthesis of calcium silicate from selective thermal transformation of waste glass and waste shell. *J. Clean. Prod.* **172**, 3019–3027 (2018).
- 260. Nakatani, N., Takamori, H., Takeda, K. & Sakugawa, H. Transesterification of soybean oil using combusted oyster shell waste as a catalyst. *Bioresour. Technol.* **100**, 1510–1513 (2009).
- 261. Jairam, S., Kolar, P., Sharma-Shivappa, R., Osborne, J. A. & Davis, J. P. KI-impregnated oyster shell as a solid catalyst for soybean oil transesterification. *Bioresour. Technol.* **104**, 329–335 (2012).
- 262. Jin, H., Kolar, P., Peretti, S., Osborne, J. & Cheng, J. Kinetics and mechanism of NaOH-impregnated calcined oyster shell-catalyzed transesterification of soybean oil. *Energies* **10**, 1920 (2017).
- 263. Jin, H., Kolar, P., Peretti, S., Osborne, J. & Cheng, J. Effect of preparation conditions on structure and activity of sodium-impregnated oyster shell catalysts for transesterification. *Catalysts* **8**, 259–271 (2018).

- 264. Risso, R., Ferraz, P., Meireles, S., Fonseca, I. & Vital, J. Highly active CaO catalysts from waste shells of egg, oyster and clam for biodiesel production. *Appl. Catal. Gen.* **567**, 56–64 (2018).
- 265. Mohammadian, N. & Akhlaghinia, B. Calcined oyster shell nanoparticles (COS NPs): a new, efficient and reusable catalyst for one-pot rapid preparation of 1,8-dioxo-octahydroxanthenes under solvent-free conditions. *Res. Chem. Intermed.* 44, 1085–1103 (2018).
- 266. Hamester, M. R. R., Balzer, P. S. & Becker, D. Characterization of calcium carbonate obtained from oyster and mussel shells and incorporation in polypropylene. *Mater. Res.* 15, 204–208 (2012).
- 267. Bari, M. L., Inatsu, Y., Kawasaki, S., Nazuka, E. & Isshiki, K. Calcinated calcium killing of *Escherichia coli* O157:H7, *Salmonella*, and *Listeria monocytogenes* on the surface of tomatoes. *J. Food Prot.* **65**, 1706–1711 (2002).
- 268. Oikawa, K., Asada, T., Yamamoto, K., Wakabayashi, H., Sasaki, M., Sato, M. & Matsuda, J. Antibacterial activity of calcined shell calcium prepared from wild surf clam. *J. Health Sci.* **46**, 98–103 (2000).
- 269. Tsou, C.-H., Wu, C.-S., Hung, W.-S., De Guzman, M. R., Gao, C., Wang, R.-Y., Chen, J., Wan, N., Peng, Y.-J. & Suen, M.-C. Rendering polypropylene biocomposites antibacterial through modification with oyster shell powder. *Polymer* **160**, 265–271 (2019).
- 270. Marie, B., Joubert, C., Tayale, A., Zanella-Cleon, I., Belliard, C., Piquemal, D., Cochennec-Laureau, N., Marin, F., Gueguen, Y. & Montagnani, C. Different secretory repertoires control the biomineralization processes of prism and nacre deposition of the pearl oyster shell. *Proc. Natl. Acad. Sci.* 109, 20986–20991 (2012).

- 271. Upadhyay, A., Thiyagarajan, V. & Tong, Y. Proteomic characterization of oyster shell organic matrix proteins (OMP). *Bioinformation* **12**, 266–278 (2016).
- 272. Marin, F. Molluscan shell matrix characterization by preparative SDS-PAGE. *Sci. World J.* **3**, 342–347 (2003).
- 273. Marin, F., Luquet, G., Marie, B. & Medakovic, D. Molluscan shell proteins: primary structure, origin, and evolution. *Curr. Top. Dev. Biol.* **80**, 209–276 (2007).
- 274. Bédouet, L., Schuller, M. J., Marin, F., Milet, C., Lopez, E. & Giraud, M. Soluble proteins of the nacre of the giant oyster *Pinctada maxima* and of the abalone *Haliotis tuberculata*: extraction and partial analysis of nacre proteins. *Comp. Biochem. Physiol. B Biochem. Mol. Biol.* **128**, 389–400 (2001).
- 275. Bédouet, L., Rusconi, F., Rousseau, M., Duplat, D., Marie, A., Dubost, L., Le Ny, K., Berland, S., Péduzzi, J. & Lopez, E. Identification of low molecular weight molecules as new components of the nacre organic matrix. *Comp. Biochem. Physiol. B Biochem. Mol. Biol.* 144, 532–543 (2006).
- 276. Rousseau, M., Boulzaguet, H., Biagianti, J., Duplat, D., Milet, C., Lopez, E. & Bédouet,
 L. Low molecular weight molecules of oyster nacre induce mineralization of the MC3T3E1 cells. J. Biomed. Mater. Res. A 85A, 487–497 (2008).
- 277. Zhang, G., Willemin, A. S., Brion, A., Piet, M. H., Moby, V., Bianchi, A., Mainard, D., Galois, L., Gillet, P. & Rousseau, M. A new method for the separation and purification of the osteogenic compounds of nacre ethanol soluble matrix. *J. Struct. Biol.* 196, 127–137 (2016).
- 278. Lamghari, M., Almeida, M. J., Berland, S., Huet, H., Laurent, A., Milet, C. & Lopez, E. Stimulation of bone marrow cells and bone formation by nacre: *in vivo* and *in vitro* studies.

 *Bone 25, 91S-94S (1999).

- 279. Latire, T., Legendre, F., Bouyoucef, M., Marin, F., Carreiras, F., Rigot-Jolivet, M., Lebel, J.-M., Galéra, P. & Serpentini, A. Shell extracts of the edible mussel and oyster induce an enhancement of the catabolic pathway of human skin fibroblasts, *in vitro*. *Cytotechnology* 69, 815–829 (2017).
- 280. Chaturvedi, R., Singha, P. K. & Dey, S. Water soluble bioactives of nacre mediate antioxidant activity and osteoblast differentiation. *PLoS ONE* **8**, e84584 (2013).
- 281. Lee, S.-Y., Kim, H.-J. & Han, J.-S. Anti-inflammatory effect of oyster shell extract in LPS-stimulated raw 264.7 cells. *Prev. Nutr. Food Sci.* **18**, 23–29 (2013).
- 282. Brion, A., Zhang, G., Dossot, M., Moby, V., Dumas, D., Hupont, S., Piet, M. H., Bianchi, A., Mainard, D., Galois, L., Gillet, P. & Rousseau, M. Nacre extract restores the mineralization capacity of subchondral osteoarthritis osteoblasts. *J. Struct. Biol.* 192, 500–509 (2015).
- 283. Willemin, A., Zhang, G., Velot, E., Bianchi, A., Decot, V., Rousseau, M., Gillet, P. & Moby, V. The effect of nacre extract on cord blood-derived endothelial progenitor cells: a natural stimulus to promote angiogenesis? *J. Biomed. Mater. Res. A* **107**, 1406–1413 (2019).
- 284. Fuji, T., Inoue, T. & Hasegawa, Y. Nacre extract prevents scopolamine-induced memory deficits in rodents. *Asian Pac. J. Trop. Med.* **11**, 202 (2018).
- 285. Ma, J. New active organic substance in oyster shell capable of scavenging oxygen free radicals with high efficiency. *Chem. Res. Chin. Univ.* **24**, 171–174 (2008).
- 286. Tseng, Y.-H., Chevallard, C., Dauphin, Y. & Guenoun, P. CaCO₃ nanostructured crystals induced by nacreous organic extracts. *CrystEngComm* **16**, 561–569 (2013).

- 287. Ma, C., Zhang, C., Nie, Y., Xie, L. & Zhang, R. Extraction and purification of matrix protein from the nacre of pearl oyster *Pinctada fucata*. *Tsinghua Sci. Technol.* **10**, 499–503 (2005).
- 288. Suzuki, M., Sakuda, S. & Nagasawa, H. Identification of chitin in the prismatic layer of the shell and a chitin synthase gene from the Japanese pearl oyster, *Pinctada fucata*. *Biosci. Biotechnol. Biochem.* **71**, 1735–1744 (2007).
- 289. Alabaraoye, E., Achilonu, M. & Hester, R. Biopolymer (chitin) from various marine seashell wastes: isolation and characterization. *J. Polym. Environ.* **26**, 2207–2218 (2018).
- 290. Zhao, J., Liao, C., Chen, X. & Song, W. Hierarchically ordered macro–mesoporous anatase TiO₂ prepared by pearl oyster shell and triblock copolymer dual templates for high photocatalytic activity. *RSC Adv.* **8**, 38461–38469 (2018).
- 291. Lee, S. W. & Choi, C. S. High-rate growth of calcium carbonate crystal using soluble protein from diseased oyster shell. *Cryst. Growth Des.* **7**, 1463–1468 (2007).
- 292. Suzuki, M., Nagasawa, H. & Kogure, T. Synthesis and structure of hollow calcite particles. *Cryst. Growth Des.* **6**, 2004–2006 (2006).
- 293. Miyamoto, H., Morimoto, K., Tanaka, A., Sato, K., Matsushiro, A., Miyashita, T. & Tonomura, B. Presence of protein complex is prerequisite for aragonite crystallization in the nacreous layer. *Mar. Biotechnol.* **5**, 37–44 (2003).
- 294. Rousseau, M., Bédouet, L., Lati, E., Gasser, P., Le Ny, K. & Lopez, E. Restoration of stratum corneum with nacre lipids. *Comp. Biochem. Physiol. B Biochem. Mol. Biol.* **145**, 1–9 (2006).
- 295. Yu, W.-C., He, C., Wu, C.-L., Wang, J., Li, Z., Guo, T., Li, Y.-C. & Wang, X.-T. Extraction and identification of melanin in shell and mantle of Pacific oyster *Crassostrea gigas*. *Oceanol. Limnol. Sin.* **46**, 909–914 (2015).

- 296. Comfort, A. Distribution of shell porphyrins in Mollusca. *Nature* **162**, 851–852 (1948).
- 297. Miyoshi, T., Matsuda, Y. & Komatsu, H. Fluorescence from pearls and shells of black lip oyster, *Pinctada margaritifera*, and its contribution to the distinction of mother oysters used in pearl culture. *Jpn. J. Appl. Phys.* **26**, 1069–1072 (1987).
- 298. Iwahashi, Y. & Akamatsu, S. Porphyrin pigment in black-lip pearls and its application to pearl identification. *Fish. Sci.* **60**, 69–71 (1994).
- 299. Feng, D., Li, Q., Yu, H., Zhao, X. & Kong, L. Comparative transcriptome analysis of the Pacific oyster *Crassostrea gigas* characterized by shell colors: identification of genetic bases potentially involved in pigmentation. *PLoS ONE* **10**, e0145257 (2015).
- 300. de Alvarenga, R. A. F., Galindro, B. M., Helpa, C. de F. & Soares, S. R. The recycling of oyster shells: an environmental analysis using Life Cycle Assessment. *J. Environ. Manage.* **106**, 102–109 (2012).
- 301. Escande, V., Velati, A., Garel, C., Renard, B.-L., Petit, E. & Grison, C. Phytoextracted mining wastes for ecocatalysis: Eco-Mn®, an efficient and eco-friendly plant-based catalyst for reductive amination of ketones. *Green Chem.* 17, 2188–2199 (2015).
- 302. Su, Y.-Y., Huang, H.-H., Yu, T.-H., Tseng, C.-C., Tsai, H.-J. & Hsu, W.-K. Optical property of nature source: UV–visible emissions from calcined oyster shells. *Opt. Mater.* **101**, 109736 (2020).
- 303. Lee, M., Tsai, W.-S. & Chen, S.-T. Reusing shell waste as a soil conditioner alternative?

 A comparative study of eggshell and oyster shell using a life cycle assessment approach. *J. Clean. Prod.* **265**, 121845 (2020).
- 304. Williams, S. T., Lockyer, A. E., Dyal, P., Nakano, T., Churchill, C. K. C. & Speiser, D. I. Colorful seashells: identification of haem pathway genes associated with the synthesis of porphyrin shell color in marine snails. *Ecol. Evol.* **7**, 10379–10397 (2017).

- 305. Grant, H. E. & Williams, S. T. Phylogenetic distribution of shell colour in Bivalvia (Mollusca). *Biol. J. Linn. Soc.* **125**, 377–391 (2018).
- 306. Snow, M. R., Pring, A., Self, P., Losic, D. & Shapter, J. The origin of the color of pearls in iridescence from nano-composite structures of the nacre. *Am. Mineral.* **89**, 1353–1358 (2004).
- 307. Comfort, A. Molluscan shells as a practical source of uroporphyrin I. *Science* **112**, 279–280 (1950).
- 308. Comfort, A. The pigmentation of molluscan shells. *Biol. Rev.* **26**, 285–301 (1951).
- 309. Affenzeller, S., Wolkenstein, K., Frauendorf, H. & Jackson, D. J. Eumelanin and pheomelanin pigmentation in mollusc shells may be less common than expected: insights from mass spectrometry. *Front. Zool.* **16**, 47 (2019).
- 310. Feng, D., Li, Q., Yu, H., Kong, L. & Du, S. Transcriptional profiling of long non-coding RNAs in mantle of *Crassostrea gigas* and their association with shell pigmentation. *Sci. Rep.* **8**, 1436 (2018).
- 311. Verdes, A., Cho, W., Hossain, M., Brennan, P. L. R., Hanley, D., Grim, T., Hauber, M. E. & Holford, M. Nature's palette: characterization of shared pigments in colorful avian and mollusk shells. *PLoS One* 10, e0143545 (2015).
- 312. Lim, C. K. High-Performance Liquid Chromatography and Mass Spectrometry of Porphyrins, Chlorophylls and Bilins. vol. 2 (World Scientific, 2009).
- 313. Barillé, L., Bris, A. L., Méléder, V., Launeau, P., Robin, M., Louvrou, I. & Ribeiro, L. Photosynthetic epibionts and endobionts of Pacific oyster shells from oyster reefs in rocky versus mudflat shores. *PLoS One* **12**, e0185187 (2017).
- 314. Nagai, K., Yano, M., Morimoto, K. & Miyamoto, H. Tyrosinase localization in mollusc shells. *Comp. Biochem. Physiol. B Biochem. Mol. Biol.* **146**, 207–214 (2007).

- 315. Lemer, S., Saulnier, D., Gueguen, Y. & Planes, S. Identification of genes associated with shell color in the black-lipped pearl oyster, *Pinctada margaritifera*. *BMC Genomics* **16**, 568 (2015).
- 316. Checa, A. G., Macías-Sánchez, E., Harper, E. M. & Cartwright, J. H. E. Organic membranes determine the pattern of the columnar prismatic layer of mollusc shells. *Proc. R. Soc. B Biol. Sci.* **283**, 20160032 (2016).
- 317. Guo, B., Cai, X., Xu, S., Fateminia, S. M. A., Liu, J., Liang, J., Feng, G., Wu, W. & Liu, B. Decoration of porphyrin with tetraphenylethene: converting a fluorophore with aggregation-caused quenching to aggregation-induced emission enhancement. *J. Mater. Chem. B* **4**, 4690–4695 (2016).
- 318. Zhang, J., Zheng, X., Hu, X. & Xie, Z. GSH-triggered size increase of porphyrin-containing nanosystems for enhanced retention and photodynamic activity. *J. Mater. Chem. B* **5**, 4470–4477 (2017).
- 319. Williams, S. T., Ito, S., Wakamatsu, K., Goral, T., Edwards, N. P., Wogelius, R. A., Henkel, T., Oliveira, L. F. C. de, Maia, L. F., Strekopytov, S., Jeffries, T., Speiser, D. I. & Marsden, J. T. Identification of shell colour pigments in marine snails *Clanculus pharaonius* and *C. margaritarius* (Trochoidea; Gastropoda). *PLoS One* 11, e0156664 (2016).
- 320. Arma, L. H., Saitoh, A., Ishibashi, Y., Asahi, T., Sueoka, Y., Sakakibara, M. & Takebe, H. Red fluorescence lamellae in calcitic prismatic layer of *Pinctada vulgaris* shell (Mollusc, bivalvia). *Opt. Mater. Express* **4**, 1813–1823 (2014).
- 321. Needham, A. E. *Zoophysiology and Ecology, Volume 3: The Significance of Zoochromes*. vol. 3 (Springer-Verlag Berlin, 1974).

- 322. Polo, C. F., Frisardi, A. L., Resnik, E. R., Schoua, A. E. & Batlle, A. M. Factors influencing fluorescence spectra of free porphyrins. *Clin. Chem.* **34**, 757–760 (1988).
- 323. Shindi, A. A. F., Zhou, P.-C., Zou, Z.-X. & Li, Y.-Q. A novel, selective, and rapid fluorimetric method for the simultaneous analysis of coproporphyrin and uroporphyrin in urine. *Anal. Chim. Acta* **664**, 89–94 (2010).
- 324. Ohno, O., Kaizu, Y. & Kobayashi, H. J-aggregate formation of a water-soluble porphyrin in acidic aqueous media. *J. Chem. Phys.* **99**, 4128–4139 (1993).
- 325. Giovannetti, R. The use of spectrophotometry UV-vis for the study of porphyrins. in *Macro To Nano Spectroscopy* 87–108 (2012).
- 326. Bielec, J., Pilas, B., Sarna, T. & Truscott, T. G. Photochemical studies of porphyrin—melanin interactions. *J. Chem. Soc. Faraday Trans. 2 Mol. Chem. Phys.* **82**, 1469–1474 (1986).
- 327. Demarque, D. P., Crotti, A. E. M., Vessecchi, R., Lopes, J. L. C. & Lopes, N. P. Fragmentation reactions using electrospray ionization mass spectrometry: an important tool for the structural elucidation and characterization of synthetic and natural products. *Nat. Prod. Rep.* **33**, 432–455 (2016).
- 328. Macours, P. & Cotton, F. Improvement in HPLC separation of porphyrin isomers and application to biochemical diagnosis of porphyrias. *Clin. Chem. Lab. Med.* **44**, 1433–1440 (2006).
- 329. Danton, M. & Lim, C. K. High-performance liquid chromatography/electrospray ionization tandem mass spectrometry of hydroxylated uroporphyrin and urochlorin derivatives formed by photochemical oxidation of uroporphyrinogen I. *Biomed. Chromatogr.* **21**, 534–545 (2007).

- 330. Fateen, E., Abd-Elfattah, A., Gouda, A., Ragab, L. & Nazim, W. Porphyrins profile by high performance liquid chromatography/electrospray ionization tandem mass spectrometry for the diagnosis of porphyria. *Egypt. J. Med. Hum. Genet.* **12**, 49–58 (2011).
- 331. Benton, C. M., Lim, C. K., Moniz, C. & Jones, D. J. Ultra high-performance liquid chromatography of porphyrins in clinical materials: column and mobile phase selection and optimisation: UHPLC of porphyrins in clinical materials. *Biomed. Chromatogr.* **26**, 714–719 (2012).
- 332. Nicholas, R. E. H. & Rimington, C. Isolation of unequivocal uroporphyrin III. A further study of turacin. *Biochem. J.* **50**, 194–201 (1951).
- 333. Danton, M. & Lim, C. K. Porphomethene inhibitor of uroporphyrinogen decarboxylase: analysis by high-performance liquid chromatography/electrospray ionization tandem mass spectrometry. *Biomed. Chromatogr.* **21**, 661–663 (2007).
- 334. Kajiwara, M., Tokiwa, S., Takatori, K. & Kojima, I. Properties of zinc uroporphyrin III produced from isopropanol by *Arthrobacter hyalinus*. *J. Ferment. Bioeng.* **79**, 174–176 (1995).
- 335. Rachma, D., Sandiningtyas, V. & Suendo, V. Isolation of chlorophyll a from spinach and its modification using Fe²⁺ in photostability study. in *Proceeding of the Third International Conference on Mathematics and Natural Sciences* vol. 2010 859–873 (2010).
- 336. Müller, T., Vergeiner, S. & Kräutler, B. Structure elucidation of chlorophyll catabolites (phyllobilins) by ESI-mass spectrometry—pseudo-molecular ions and fragmentation analysis of a nonfluorescent chlorophyll catabolite (NCC). *Int. J. Mass Spectrom.* **365**–**366**, 48–55 (2014).

- 337. Budd, A., McDougall, C., Green, K. & Degnan, B. M. Control of shell pigmentation by secretory tubules in the abalone mantle. *Front. Zool.* **11**, 62 (2014).
- 338. Zhang, G. *et al.* The oyster genome reveals stress adaptation and complexity of shell formation. *Nature* **490**, 49–54 (2012).
- 339. Sommerdijk, N. A. J. M. & With, G. de. Biomimetic CaCO₃ mineralization using designer molecules and interfaces. *Chem. Rev.* **108**, 4499–4550 (2008).
- 340. Lahiri, J., Xu, G., Dabbs, D. M., Yao, N., Aksay, I. A. & Groves, J. T. Porphyrin amphiphiles as templates for the nucleation of calcium carbonate. *J. Am. Chem. Soc.* **119**, 5449–5450 (1997).
- 341. Hayatsu, H., Negishi, T., Arimoto, S. & Hayatsu, T. Porphyrins as potential inhibitors against exposure to carcinogens and mutagens. *Mutat. Res. Mol. Mech. Mutagen.* **290**, 79–85 (1993).
- 342. Martins, C., Rodrigo, A. P., Cabrita, L., Henriques, P., Parola, A. J. & Costa, P. M. The complexity of porphyrin-like pigments in a marine annelid sheds new light on haem metabolism in aquatic invertebrates. *Sci. Rep.* **9**, 12930 (2019).
- 343. Cuthill, I. C. *et al.* The biology of color. *Science* **357**, eaan0221 (2017).
- 344. Battersby, A. R. Tetrapyrroles: the pigments of life. Nat. Prod. Rep. 17, 507–526 (2000).
- 345. Linzen, B. The tryptophan → ommochrome pathway in insects. in *Advances in Insect Physiology* vol. 10 117–246 (Elsevier, 1974).
- 346. Bandaranayake, W. M. The nature and role of pigments of marine invertebrates. *Nat. Prod. Rep.* **23**, 223 (2006).
- 347. Figon, F. & Casas, J. Ommochromes in invertebrates: biochemistry and cell biology. *Biol. Rev.* **94**, 156–183 (2019).

- 348. Panettieri, S., Gjinaj, E., John, G. & Lohman, D. J. Different ommochrome pigment mixtures enable sexually dimorphic Batesian mimicry in disjunct populations of the common palmfly butterfly, Elymnias hypermnestra. *PLoS ONE* **13**, e0202465 (2018).
- 349. Figon, F., Munsch, T., Croix, C., Viaud-Massuard, M.-C., Lanoue, A. & Casas, J. Uncyclized xanthommatin is a key ommochrome intermediate in invertebrate coloration. *Insect Biochem. Mol. Biol.* **124**, 103403 (2020).
- 350. Reiter, S., Hülsdunk, P., Woo, T., Lauterbach, M. A., Eberle, J. S., Akay, L. A., Longo, A., Meier-Credo, J., Kretschmer, F., Langer, J. D., Kaschube, M. & Laurent, G. Elucidating the control and development of skin patterning in cuttlefish. *Nature* **562**, 361–366 (2018).
- 351. Chan-Higuera, J. E., Santacruz-Ortega, H. del C., Carbonell-Barrachina, Á. A., Burgos-Hernández, A., Robles-Sánchez, R. M., Cruz-Ramírez, S. G. & Ezquerra-Brauer, J. M. Xanthommatin is behind the antioxidant activity of the skin of *Dosidicus gigas*. *Molecules* 24, 3420 (2019).
- 352. Williams, T. L., DiBona, C. W., Dinneen, S. R., Jones Labadie, S. F., Chu, F. & Deravi, L. F. Contributions of phenoxazone-based pigments to the structure and function of nanostructured granules in squid chromatophores. *Langmuir* 32, 3754–3759 (2016).
- 353. Bolognese, A. & Liberatore, R. Photochemistry of ommochrome pigments. *J. Heterocycl. Chem.* **25**, 1243–1246 (1988).
- 354. Nijhout, H. F. Ommochrome pigmentation of the *linea* and *rosa* seasonal forme *Precis* coenia (Lepidoptera: Nymphalidae). *Achives Insect Biochem. Physiol.* **36**, 215–222 (1997).
- 355. Daniels, E. V. & Reed, R. D. Xanthurenic acid is a pigment in *Junonia coenia* butterfly wings. *Biochem. Syst. Ecol.* **44**, 161–163 (2012).

- 356. Linzen, B. Ommidine ein neuer typus von ommochromen aus orthopteren. Z. Für Naturforschung B 21, 1038–1047 (1966).
- 357. Butenandt, A., Biekert, E. & Linzen, B. Über ommochrome, XIV. Zur verbreitung der ommine im tierreich. *Hoppe-Seyler's Z. Für Physiol. Chem.* **313**, 251–258 (1958).
- 358. Holl, A. Coloration and chromes. in *Ecophysiology of Spiders* (ed. Nentwig, W.) 16–25 (Springer Berlin Heidelberg, 1987).
- 359. Butenandt, A., Biekert, E., Koga, N. & Traub, P. Über ommochrome, XXI. Konstitution und synthese des ommatins D. *Hoppe-Seyler's Z. Für Physiol. Chem.* **321**, 258–275 (1960).
- 360. Hsiung, B.-K., Blackledge, T. A. & Shawkey, M. D. Spiders do have melanin after all. *J. Exp. Biol.* **218**, 3632–3635 (2015).
- 361. Ostrovsky, M. A., Zak, P. P. & Dontsov, A. E. Vertebrate eye melanosomes and invertebrate eye ommochromes as screening cell organelles. *Biol. Bull.* **45**, 570–579 (2018).
- 362. Huijser, A., Pezzella, A. & Sundström, V. Functionality of epidermal melanin pigments: current knowledge on UV-dissipative mechanisms and research perspectives. *Phys. Chem. Chem. Phys.* **13**, 9119 (2011).
- 363. Cai, Z., Wu, J., Chen, L., Guo, W., Li, J., Wang, J. & Zhang, Q. Purification and characterisation of aquamarine blue pigment from the shells of abalone (*Haliotis discus hannai* Ino). *Food Chem.* **128**, 129–133 (2011).
- 364. Barnard, W. & de Waal, D. Raman investigation of pigmentary molecules in the molluscan biogenic matrix. *J. Raman Spectrosc.* **37**, 342–352 (2006).
- 365. Comfort, A. Acid-soluble pigments of molluscan shells. 3. The indigoid character of the blue pigment of *Haliotis cracherodii* Leach. *Biochem. J.* **45**, 204–208 (1949).

- 366. Comfort, A. Identity of the shell pigment of *Haliotis cracherodii* Leach. *Nature* **163**, 647–647 (1949).
- 367. Comfort, A. Acid-soluble pigments of shells. 1. The distribution of porphyrin fluorescence in molluscan shells. *Biochem. J.* **44**, 111–117 (1949).
- 368. Comfort, A. Acid-soluble pigments of molluscan shells. 2. Pigments other than porphyrins. *Biochem. J.* **45**, 199–204 (1949).
- 369. Nicholas, R. E. H. & Comfort, A. Acid-soluble pigments of molluscan shells. 4. Identification of shell porphyrins with particular reference to conchoporphyrin. *Biochem. J.* 45, 208–210 (1949).
- 370. Jones, P. & Silver, J. Red and blue-green bile pigments in the shell of *Astraea tuber* (Mollusca: Archaeogastropoda). *Comp. Biochem. Physiol. Part B Comp. Biochem.* **63**, 185–188 (1979).
- 371. Patnaik, P. Handbook of inorganic chemicals. (McGraw-Hill, 2003).
- 372. Ayotte, P., Hébert, M. & Marchand, P. Why is hydrofluoric acid a weak acid? *J. Chem. Phys.* **123**, 184501 (2005).
- 373. Autier, P., Doré, J. F. & Césarini, J.-P. Should subjects who used psoralen suntan activators be screened for melanoma? *Ann. Oncol.* **8**, 435–437 (1997).

Identification de composés valorisables présents dans la coquille de l'huître comestible *Crassostrea gigas**

Ces travaux de thèse ont été réalisés dans le cadre d'une convention industrielle de formation par la recherche (Cifre) entre l'entreprise ostréicole Tarbouriech-Médithau, basée à Marseillan sur le bord de l'Etang de Thau, et deux instituts du Pôle Chimie Balard de l'Université de Montpellier : l'Institut des Biomolécules Max Mousseron et l'Institut Charles Gerhart Montpellier. L'objectif principal visait l'identification de composés valorisables issus de coquilles de l'huître *Crassostrea gigas* Tarbouriech-Médithau, aux caractéristiques morphologiques et organoleptiques singulières. Cette étude s'est positionnée dans un cadre plus général de valorisation de la coquille de l'huitre comestible comme matériau biosourcé, faisant ressortir les avantages et les défis afférents à leur recyclage ainsi que la nécessité de participer à l'approfondissement de certains aspects fondamentaux non encore décrits.

Ainsi, la couleur rose-pourpre des coquilles de l'huître *Crassostrea gigas* a fait l'objet d'une étude visant à extraire et identifier les biomolécules contribuant à cette coloration. Les travaux d'extraction ont nécessité le développement de méthodes originales et fiables, applicables à l'extraction de pigments solubles en milieu acide aqueux. L'analyse structurale de ces composés par chromatographie liquide en phase inverse combinée à la spectrométrie de masse haute résolution, par spectroscopie de fluorescence et par résonnance magnétique nucléaire, a permis de nouvellement identifier des familles de biomolécules hétérocycliques tels que les porphyrines. L'extraction et l'identification de ces composés ouvrent la voie à des applications qui pourraient permettre d'envisager construire des procédés de recyclage innovant des coquilles d'huîtres *Crassostrea gigas*.

Mots clefs: Crassostrea gigas, pigments, extraction, identification, spectrométrie de masse

Identification of valuable compounds from the shell of the edible oyster Crassostrea gigas

This thesis program was carried out in a partnership between the oyster farming company Tarbouriech-Médithau, located on the edge of the Thau lagoon (Marseillan), and two institutes of The Balard Chemistry Centre of The University of Montpellier: The Institute of Biomolecules Max Mousseron and The Institute Charles Gerhart Montpellier. The main objective was the identification of valuable compounds from the shells of the oyster *Crassostrea gigas* Tarbouriech-Médithau with singular morphological and organoleptic properties. This study was positioned within the more general framework of the recycling of the shell of this edible oyster as a source of natural materials, highlighting the advantages and challenges related to its recycling as well as the need to participate to the investigation of particular fundamental aspects not described to date.

Thus, the pink-purple colour of the shell of the oyster *Crassostrea gigas* was investigated in order to extract and identify the biomolecules contributing to this colour. The extraction required the development of original and reliable methods, applicable to the extraction of acid-soluble pigments. The structural investigation of these compounds conducted by reverse phase liquid chromatography combined with high-resolution mass spectrometry, by fluorescence spectroscopy and by nuclear magnetic resonance, made possible the newly identification of heterocyclic biomolecules such as porphyrins. The extraction and the identification of these compounds open the way to applications and allow to consider the development of innovative recycling processes of shells of the oyster *Crassostrea gigas*.

Key words: Crassostrea gigas, pigments, extraction, identification, mass spectrometry